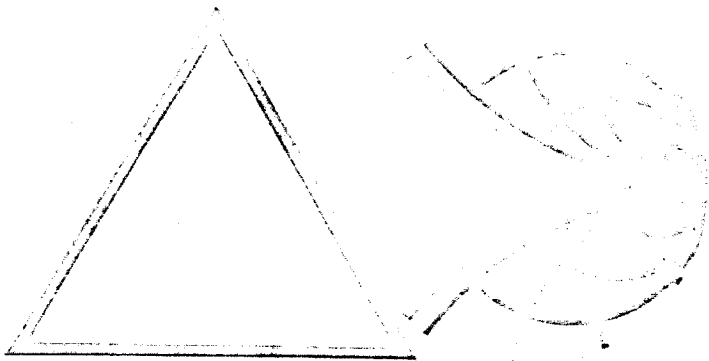TR-66
3 September 1965

A HIGH-GAIN OMNI-
DIRECTIONAL SATELLITE
ANTENNA TECHNIQUE

Contract No. NAS 5-3947

Prepared by:

G. G. Chadwick, Chief Engineer

J. E. Hill, Technical Consultant

P. Kerr, Engineer

Approved by:

G. G. Chadwick, Chief Engineer

Prepared for:

NASA
Goddard Space Flight Center
Greenbelt, Maryland

Radiation Systems incorporated 440 Swann Avenue, Alexandria, Virginia

TABLE OF CONTENTS

LIST OF ILLUSTRATIONS

List of Illustrations (Cont'd) –

List of Illustrations (Cont'd) –   <u>Page</u>

FOREWORD

The final report contained herein describes an engineering model of a novel antenna technique which is particularly well suited for use in space borne vehicles. The antenna system consists of a 12-element planar multiple-beam array and a 4 x 16-element multiple-beam circular array. Solid state switching is used in both arrays to reduce the outputs to a single terminal.

The planar array is of the multiple-beam variety and has twelve beam output positions; one for each element. These beams totally cover an included cone angle of approximately 90 degrees. This coverage sector is centered symmetrically about the axis normal to the array. The planar array is unique in that the individual spiral radiator elements are arranged to form three-element building blocks rather than the four-element building blocks used in more conventional multiple-beam systems. Solid state switches, capable of handling 20 watts of average power, are utilized to reduce the twelve beam outputs to a common input/output terminal.

The cylindrical array portion of the system consists of four tiers of sixteen spiral cavity radiators uniformly disposed about the periphery of the cylinder. These antenna outputs are processed by a unique translation matrix. The outputs of the translation or mode forming network are, in turn, processed by a multiple-beam matrix. This arrangement allows the simultaneous generation of sixteen multiple-beams, with the beam dispositions
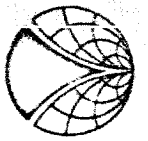
being uniform in azimuth. Four banks of these sixteen beams are formed; one for each of four elevation stations. The total elevation coverage is approximately 90 degrees. Solid state switches are provided for selection of the desired elevation bank and also to reduce the sixteen beams from any elevation bank to a single output terminal.

The final report discusses the theory of operation and the data obtained for the above described system. The report also contains a description of the solid state switch driver and a description of a beam interposition technique utilized to avoid gain loss at the beam crossover points. A detailed block diagram of the system and the necessary schematics are also included as part of the basic report.

1.0 INTRODUCTION

The technical content of this final report has been prepared under the sponsorship of the National Aeronautics and Space Administration, Greenbelt, Maryland, through the medium of a contract numbered NAS 5-3927. The objective of the program was to design, fabricate, and deliver to the Goddard Space Flight Center, a completely integrated antenna system with automatic beam control.

The developed antenna system consists of a twelve-element planar multiple-beam array and a 4 x 16-element multiple-beam circular array. Solid state switching networks are used in both arrays to reduce the multiple-beam ports to a single r-f terminal.

The planar array is of the multiple-beam class and generates twelve simultaneous beams; one for each element. These beams totally cover a 90 degree conical sector of space. This coverage sector is centered about the axis normal to the array surface. The planar array is unique in that the individual spiral radiator elements are arranged to form three-element building blocks rather than the four-element building blocks used in more conventional multiple-beam systems. Solid state switches, capable of handling 20 watts of average power, are utilized to reduce the twelve beam outputs to a common input/output terminal.

The cylindrical array consists of four tiers of sixteen spiral cavity radiators each. The radiators in each tier are uniformly disposed about the

periphery of the cylinder. These antenna outputs are processed by a mode forming matrix. The terminals of the mode forming network are processed, through sixteen SP4T solid state switches, by a multiple-beam network. The sixteen outputs of this network represent sixteen simultaneous beams which lie in one of four elevation stations and which are uniformly disposed in azimuth. The SP4T switches allow selection of the desired elevation sector. The total elevation coverage is approximately 90 degrees. Solid state switches are provided to reduce the sixteen beam terminals from any elevation bank to a single r-f terminal.

The antenna system is designed to operate at frequencies of 1700 and 2270 mc. It provides circularly polarized, high gain coverage over all space, with the exception of a 90 degree cone of silence. This 90 degree cone of silence would not occur if two opposed planar arrays were utilized in place of the present single planar array. However, the addition of a second planar array does not add to knowledge of the system's performance or capability and hence it was deleted.

The solid state switching components are capable of handling 20 watts of average r-f power at a frequency of 1700 mc. The peak power rating on these components is 1.2 kw. The insertion loss of the individual SPDT solid state switches is 0.4 db with a minimum isolation requirement of 20 db. The requirements of the SP16T and SP12T switches, needed for the cylindrical and circular arrays, respectively, are identical except for an increase in the insertion loss to a total value of 1.6 db.
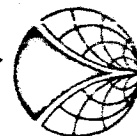
The program was divided into three phases. The first phase provided for a study of the proposed antenna system. Its objective was to define the performance of the components and networks which, when integrated, would form the system. The study was also to be utilized to predict the system's performance and to define the impact of component tolerances on the system performance. A component design effort was conducted concurrently with this study effort. The objective, in this instance, was to design, test, and evaluate all of the critical strip transmission line components needed for the networks and to generate the necessary negatives for forming the major networks.

Phase II of the program required that the necessary networks be developed for the planar and cylindrical arrays. The beam switching networks were also designed, developed, and evaluated during this phase. This phase was additionally used to fabricate the antenna elements.

Phase III of the program was devoted to system integration and testing. It was during this last phase that all final data were obtained and evaluated.

The technical content of this final report is divided into three major subsections. Section 2.0, entitled "General Discussion", defines the system block diagram and the general characteristics of the system. Section 3.0, entitled "Antenna System Design", describes the theory and design of the components and major subcomponents which, en toto, form the entire assembly.

Section 3.0 also contains a description of the mechanical packaging of the antenna system and the necessary schematics. Section 4.0, entitled "System Performance", contains the test data obtained with the assembly. This section is also used to analyze the data in light of the predicted performance and to define the possible sources of deviation between the predicted and obtained values. Section 5.0, entitled "Recommendations and Conclusions", summarizes the system performance and outlines those areas where system improvements may be realized in future models.

2.0 GENERAL DISCUSSION

The objective of this section of the report is to describe the general characteristics of the developed antenna system. Attention will also be directed to the definition of the antenna system block diagram.

A photograph of the developed antenna system is shown as Figure 1. The 12-element planar array and the 4 x 16-element cylindrical array are easily recognizable in the photograph. The spacial distribution of the simultaneous multiple-beams achieved with each of these two arrays is illustrated in the sketch of Figure 2 along with the coordinate system which will be used as a reference throughout this report. Examination of Figure 2(b) will indicate that a total of twelve beams are generated by the planar array. The beams from this array cover an approximate 90 degree conical sector of space, centered symmetrically about the zenith axis ($\theta = 0$). The cylindrical array generates a total of 64 beams. These 64 beams are divided into four separate elevation tiers of 16 beams each. The four elevation beams, at any given azimuth station, cover an elevation sector of approximately 90 degrees. This elevation sector is more or less centered about the horizon reference plane ($\theta = 90^{\circ}$). The 16 beams in each elevation tier provide coverage over a 360 degree azimuth sector. Note that the lower 90 degree conical sector is missing. An additional 12-element planar array, opposed in its orientation to the existing 12-element array, would be required to fill the cone of silence in the downward ($\theta = 180^{\circ}$) direction.
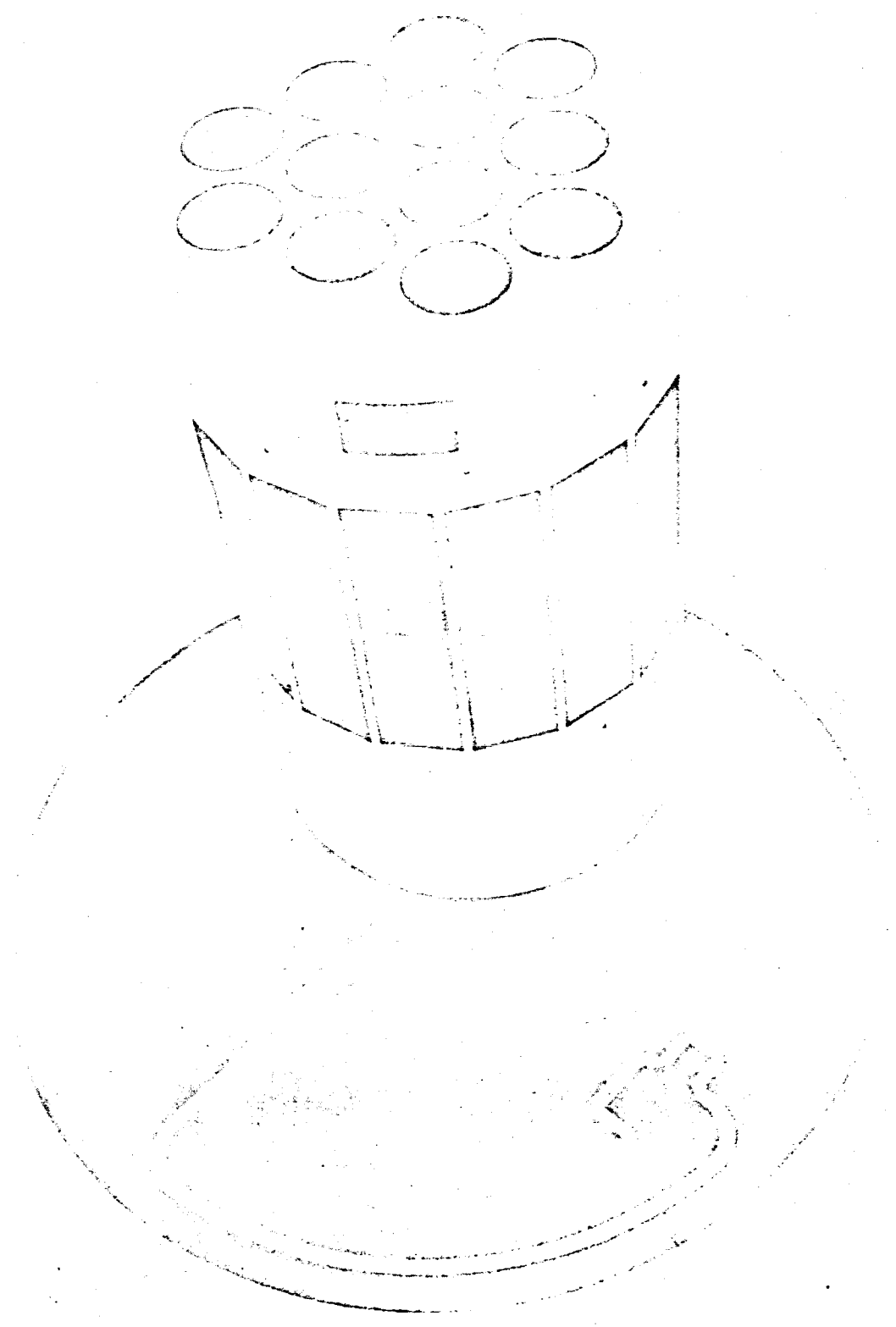
Figure 1. The planar-cylindrical multiple-beam antenna system.

PLANAR ARRAY
(12 ELEMENTS)

θ

$E\theta$

$E\phi$

CIRCULAR ARRAY
(16 ELEMENTS)

$\phi = 0°$

ϕ

$\phi = 90°$

a)

$\theta = 0°$

SECTOR OF PLANAR
ARRAY COVERAGE
(12 BEAMS)

CYLINDRICAL ARRAY SECTOR
64 BEAMS TOTAL

CYLINDRICAL
ARRAY SECTOR

$\theta = 90°$

16 IN
EACH TIER

$\theta = 180°$
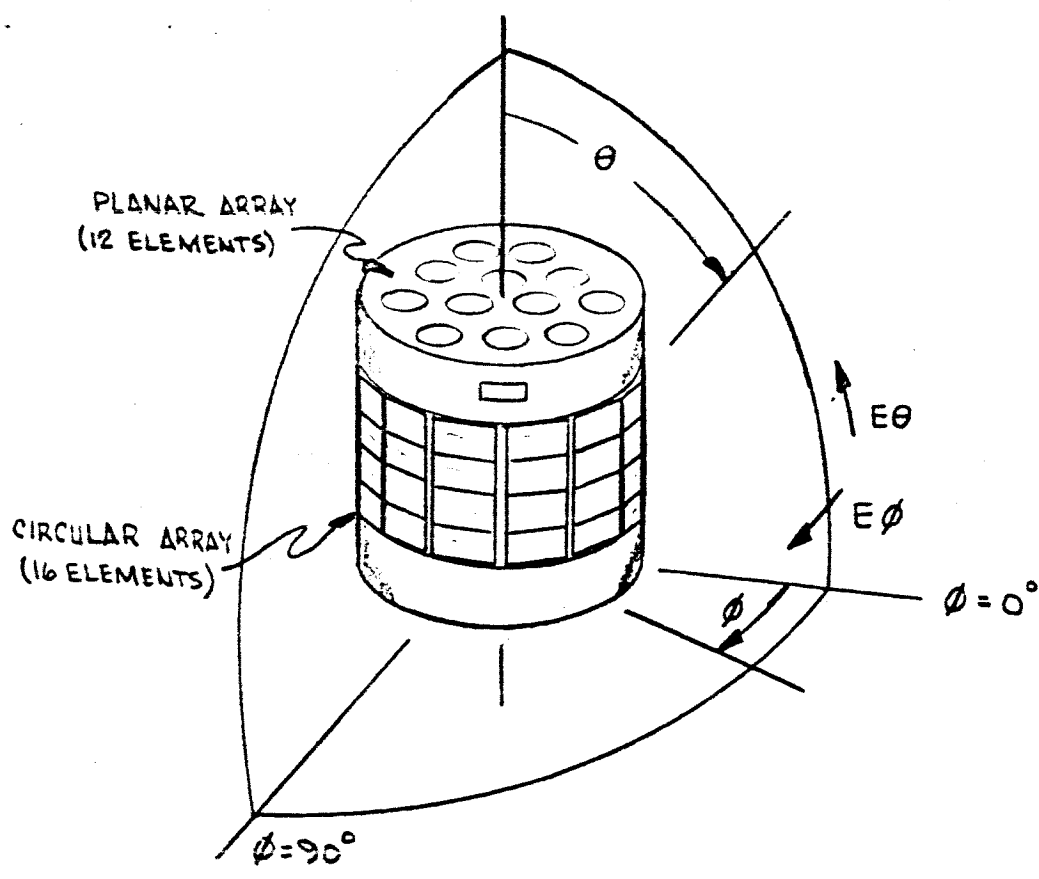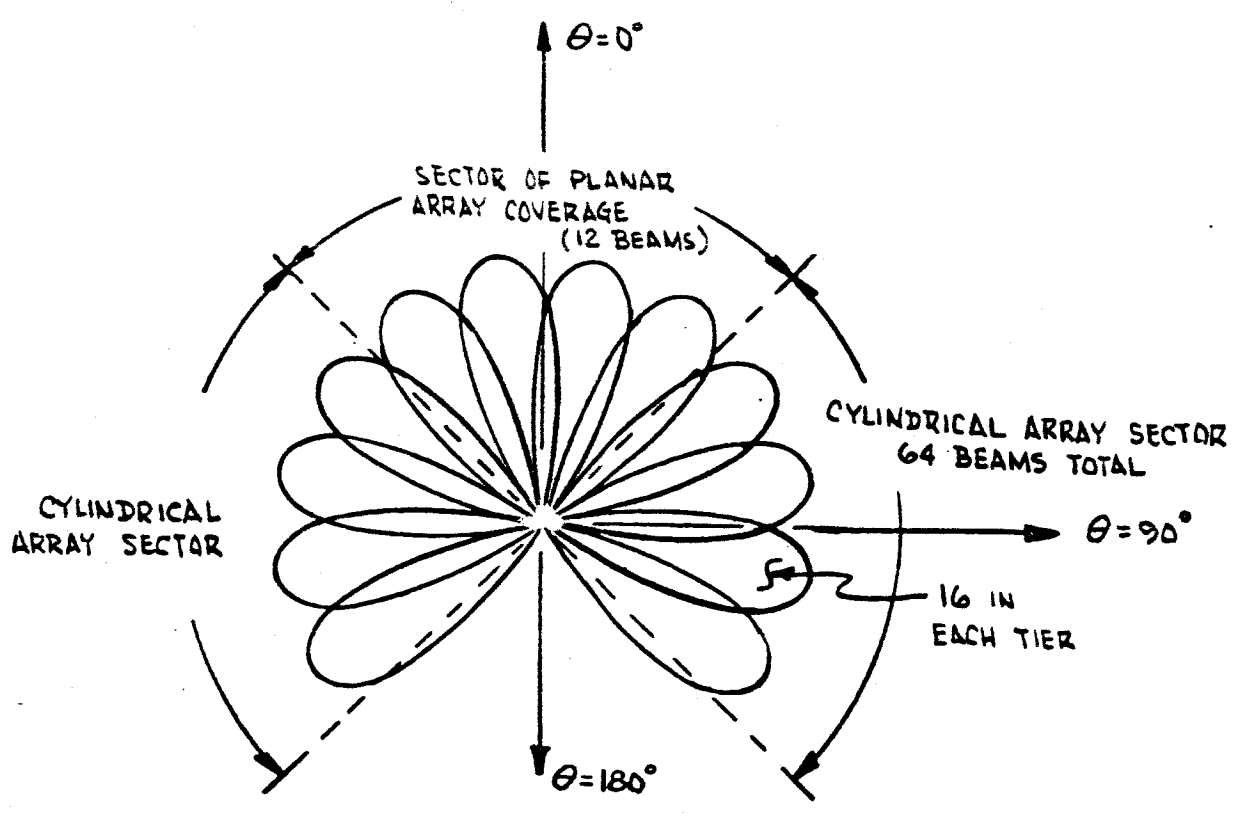
b)

Figure 2(a). Coordinate system and array geometry.
(b). Disposition of multiple beams.

The beams generated by the planar array have a nominal beamwidth of approximately 24 degrees and are approximately circular in cross-section. The simultaneous multiple beams generated by the cylindrical array have a nominal azimuth beamwidth of 20 degrees with a nominal elevation beamwidth of approximately 24 degrees.

A block diagram of the complete multiple-beam antenna system is shown in the sketch of Figure 3. This functional block diagram is divided into two parts, with the only common linkage being the switch control network. This network drives the solid state switches.

The twelve-element array consists of twelve spiral cavity antennas, geometrically arranged in the manner shown in Figure 1. These spiral elements form an array of the multiple-beam class. This array utilizes a three-element building block rather than the four-element building block of conventional multiple-beam networks. The advantage of this technique is that it allows better beam "packing" in space (i.e., the beam crossover levels, common to any three elements, are higher than the beam crossover levels common to any four elements in a conventional multiple-beam array). The technique has the further advantage of allowing the array geometry to approach a circular configuration, thereby achieving sidelobes which are lower than the rectangularly configured or square configured multiple-beam uniformly excited arrays.

The planar array antenna terminals are connected to a twelve-port multiple-beam matrix. This matrix excites all elements in phase for any given
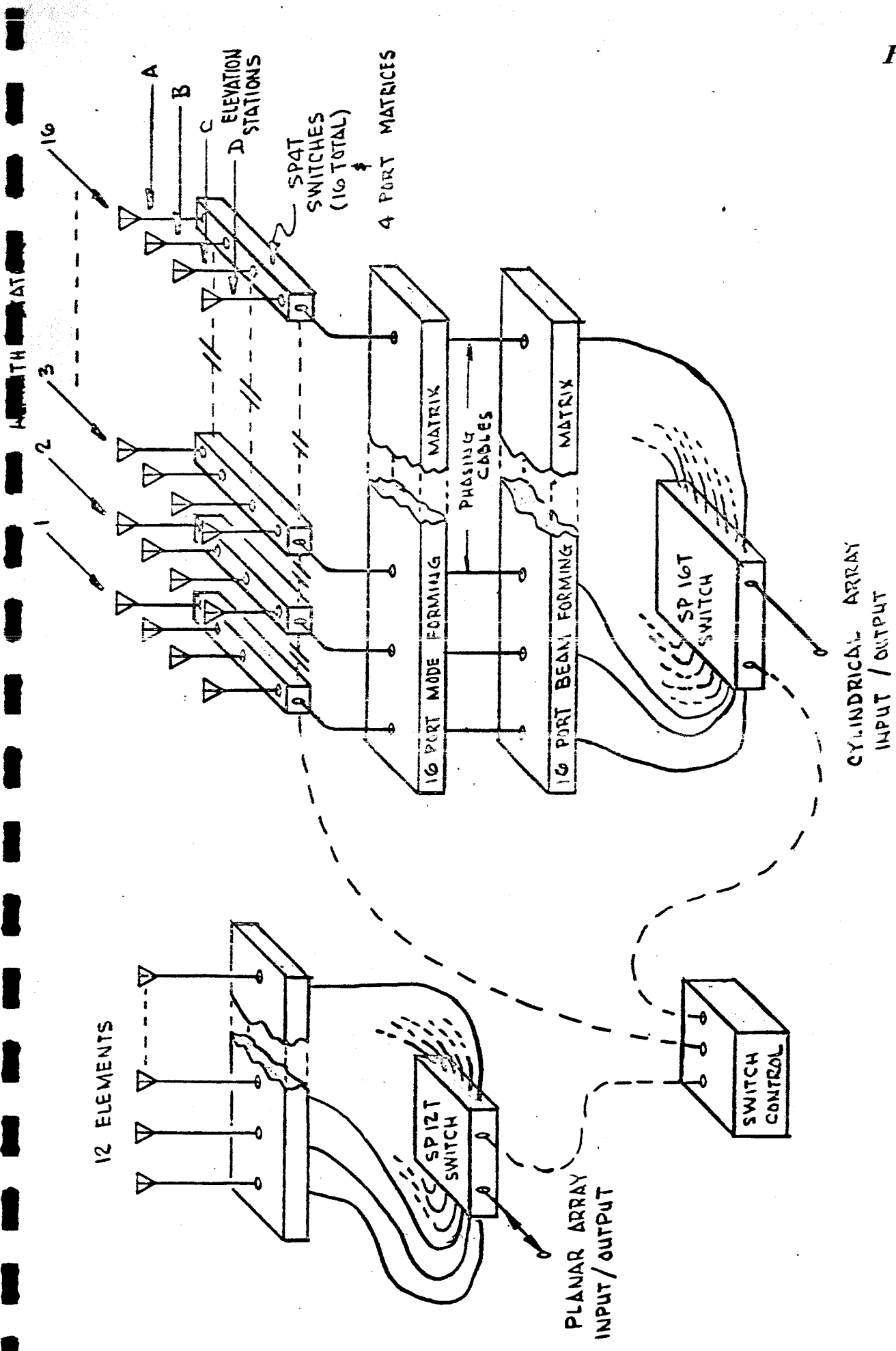
Figure 3. Antenna system block diagram.

input port, however, the phase distribution is controlled from port to port

to achieve simultaneous beams which are more or less uniformly distributed

over a 90 degree conical sector in space. The outputs of the twelve-port

matrix are routed into a SP12T solid state switching network. This switch-

ing network is capable of handling 20 watts of average power and 1.2 kw

of peak power. The output of the switching network constitutes the output

of the planar array system. The solid state switches are controlled, at

nanosecond rates, by a remote switch control network.

The cylindrical array consists of 64 spiral cavity elements having

square radiating surfaces. The orientation of these elements on the surface

of the cylinder is best described by reference to the photograph of Figure 1.

The arrangement consists of sixteen vertical rows of four elements each.

Each of these vertical rows of four elements is connected to an individual

four-port multiple-beam matrix. These individual multiple-beam matrices

excite the four elements in a given vertical bank to generate four beams,

displaced in elevation, and lying at a common azimuth station. These beams

are arranged to cover a 90 degree elevation sector which is more or less

symmetric about the horizon reference. The outputs of the four simultaneously

generated beams in each elevation bank are reduced to a single terminal by a

SP4T solid state switching network. This switching network is a low power

device and is controlled by the switch control unit.

The outputs of the SP4T switch networks are connected to a sixteen-

port mode forming matrix. This matrix develops an equivalence between the outputs of the cylindrical array and those obtainable from a linear array. Each input port excites all elements with equal amplitude but the phase excitation varies from port to port. The result is a series of pseudo omnidirectional modes each having different phase progressions. The mathematical form of these modes, in their pure sense, is identical to the mathematical form of a single element of a 16-element array. The only significant distinction is the difference between the arguments. In the linear array the argument is a function of the wavelength, spacing, and the azimuth angle. In the cylindrical array the argument is a function of only the azimuth angle. It is this identity of form which allows the inputs of the mode forming matrix to be treated in the same manner as the inputs of a linear array. Since the argument for the cylindrical array is not a function of wavelength, it follows that its beamwidths should be constant with frequency and that the crossovers between these beam should likewise remain at a near constant value.

The outputs of the mode forming matrix are processed by a sixteen-port multiple-beam matrix. It is this matrix which combines the translated mode outputs to form sixteen simultaneous beams disposed evenly over 360 degrees of azimuth angle. These beams may be formed at any of four elevation stations, with the elevation selection being made by the tandem operated SP4T switches discussed above. The outputs of the sixteen-port matrix are

reduced to one terminal by means of a SP16T solid state switch. This switch is driven, at nanosecond rates, by the same switch control network which drives the planar array. The SP16T switch is also capable of handling 20 watts of average power with a peak power capacity in excess of 1.2 kw.

In addition to the design of the above described system, an individual four-element array was developed and tested. This array resembles, in its physical appearance, the vertical banks used in the cylindrical array. It also is connected to a four-port multiple-beam network and a SP4T switch. However, there is one distinct difference: A "one-shot" digital phase shifter is utilized. The phase shifters are so arranged that, when excited, they cause the multiple-beam positions to be reoriented. The reoriented beam positions have maxima where the original beam crossovers existed. The purpose of investigating this technique is to demonstrate that it is possible to interposition the beam maxima to avoid the gain loss normally encountered at the crossover positions.

The next section of the report will detail the design of the array and the four-element network with beam interpositioning.

3.0   ANTENNA SYSTEM DESIGN

3.1 General

This section of the report will describe the detailed design of the antenna system. Attention will first be directed to the cylindrical array, its theory of operation, and the detailed design considerations which were implemented to achieve the final antenna model. The planar array will be discussed in Section 3.3 The theory of operation for the planar array will be discussed along with the detailed design considerations. Section 3.4 will describe the switch control network which is utilized to activate the solid state switches that guide the beams in space. Section 3.5 will discuss the packaging of the antenna. Section 3.6 will describe the design of the four-element array which has the capability of interpositioning beams. System performance characteristics will not be contained in this section of the report. They will be described, in detail, in Section 4.0.

3.2 Cylindrical Array

The block diagram of the cylindrical array was discussed in Section 2.0 and described in Figure 3. The intent of this section of the report is to describe the theory of operation of the array, its detailed design, and the design of the components which were required to implement the cylindrical array. Data will be presented for all of the individual components. However, no data will be described relating to the performance of the overall

antenna system. The system performance characteristics are contained

in Section 4.0.

3.2.1 Theory of Operation

The circular array was originally developed under an Air Force

contract for the Air Force Cambridge Research Laboratory of Bedford,

Massachusetts. This effort defined the theoretical considerations nec-

essary for the implementation of a cylindrical array which could provide

high gain coverage over 360 degrees of azimuth angle. Several exper-

imental models were developed to demonstrate the practicality of the

system approach. A great deal of technical literature, describing the

cylindrical array concept, was generated under the above referenced

program effort. It is not the intent of this report to totally document the

complete theory of operation of the circular array. The interested reader

is referred to references 1 through 3 of the bibliographies for more com-

plete detail. However, it is felt that an abridged description of the

theory of operation is in order. This abridged theory of operation is

contained in the following paragraphs. It will be followed in Section

3.2.2 by the detailed design description of the specific array developed

for the present program.

The geometry of the cylindrical array has always been appeal-

ing to system designers because of its ability to provide 360 degrees of

coverage. A technique will be discussed which allows a cylindrical array
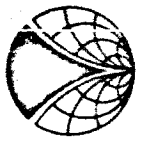
to provide high resolution coverage over 360 degrees of azimuth angle. When used as a scanning array, a beam may be swept through 360 degrees by using any of the numerous techniques available for scanning a linear array. When used to provide multiple beams, an array of N elements is excited by N isolated inputs. Each input corresponds to a beam in a selected direction; all of the N beams being disposed uniformly over 360 degrees of azimuth angle. In both the instance of the scanning array and the multiple-beam array, the resolution achieved is comparable to that available from a planar aperture of the same height and with a length equal to that of the cylinder diameter.

In a conventional linear array, each element is controlled in amplitude and phase to achieve a given result. In the cylindrical array, the outputs of each element of an array, having N elements, are processed by a network having N inputs. Each input excites all of the N array elements with equal amplitudes, but with differing phase excitations. These phase excitations are progressive. The increments of phase progression increase from one processing port to the next. The resulting far-field patterns for each of these modes are nearly omnidirectional for the instance where the phase progression between the elements is not large. As the interelement phase progression increases with increasing mode number, the omnidirectivity of the mode deteriorates. When the highest order mode is used, the phase progression between elements is 180 degrees.

This type of phase excitation generates an N-lobed amplitude pattern[*] which, because of its special nature, is only useful for multiple-beam applications. The far-field phase pattern of the remaining modes is not uniform with azimuth angle but will vary from zero to $\pm (N-2) \emptyset /2$ degrees (where $\emptyset$ is the azimuth angle), depending on which input port is excited. The mathematical form of the pseudo omnidirectional patterns, generated by these remaining $(N-1)$ input ports, differs from the mathematical form of the individual elements of a linear array only in the definition of the argument. Since the patterns generated by the inputs of the circular array processing network are of the same form as those used for a linear array, it follows that they may, in turn, be processed by any of the myriad techniques used to process a linear array.

It is important to distinguish between the individual terms used in both cases. In the linear array, the elemental terms represent the contribution of a single radiator in the array. In the cylindrical array, the equivalent elemental terms each represent the equiamplitude progressive phase excitation of all N elements. The distinction between the cylindrical array terms, or modes, is simply the incremental phase difference between each of the N elements.

Figure 4 is a sketch depicting N radiating elements arranged to form a ring in the horizon plane. The spacial orientation of the array, and the physical array parameters denoted in this figure, will be used throughout

-18-
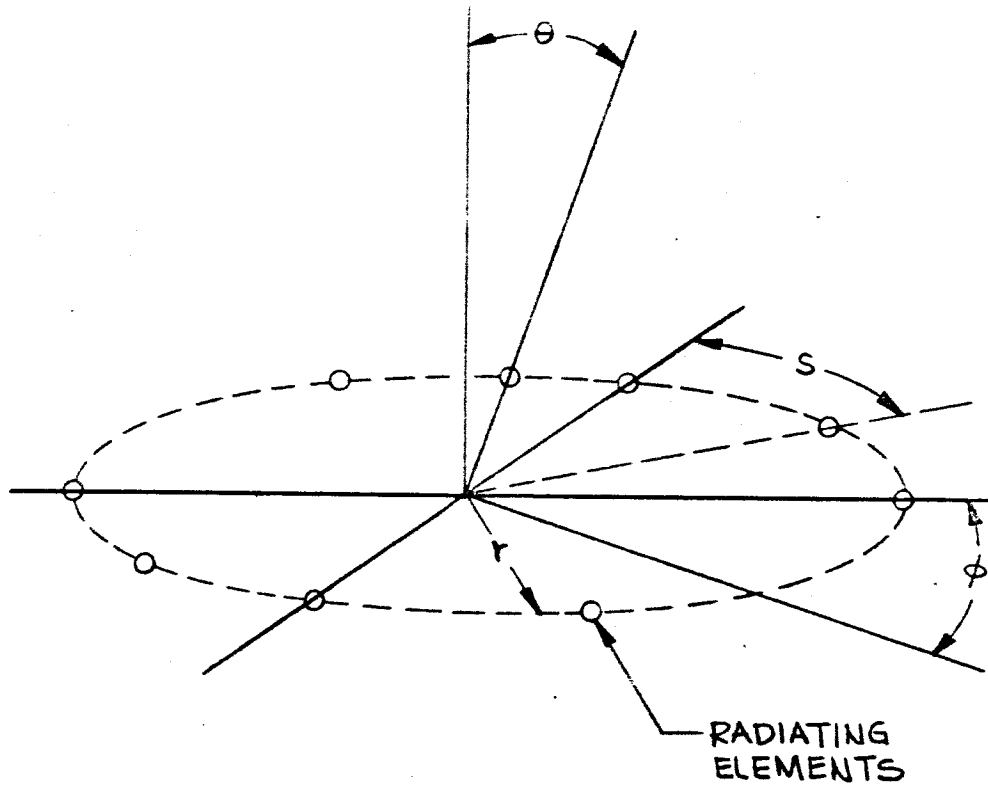
Figure 4. Basic geometry and coordinate system of the cylindrical array.

the remainder of the discussion. The radiation patterns realizable from this type of array may be represented in complex Fourier form as

$$E(\emptyset) = A_0(\emptyset) + A_1(\emptyset)\, e^{j\emptyset} + A_2(\emptyset)\, e^{j2\emptyset} \text{---} A_N(\emptyset)\, e^{jN\emptyset}, \qquad (1)$$

or more simply in the summation form,

$$E(\emptyset) = \sum_{n=0}^{n=N-1} A_n\, e^{jn\emptyset}. \qquad (2)$$

In earlier applications, most investigators were only interested in exciting the A_0 term to achieve an equiphase, equiamplitude distribution of radiated energy in the $\emptyset$ plane. The imperfections in these patterns, both in phase and amplitude were generally minimized. These imperfections, represented by the remainder of the Fourier terms, generally increased with frequency, thereby limiting the range of frequencies over which a given maximum level of imperfection could be achieved. Later efforts were concerned with the generation of single-lobed patterns. These patterns were indirectly realized by the judicious control of the coefficients A_n. It should be noted, however, that the design procedure was not generally synthesized directly from the Fourier series of equation (1). Early beam-forming methods modified the element phases with line length devices to form a plane wave front and then the element excitation was varied to achieve a given beam shape. Nonetheless, it can be shown that equivalent results could have been achieved by controlling the amplitude coefficients of equation (1).

The idea of synthesizing any beam from a circular array that could be synthesized from a linear array first germinated when the similarity of their basic format was recognized. The general expression for a linear array of N elements may be written directly as

$$E'(\emptyset) = \sum_{n=0}^{n=N-1} A_n e^{jnu} \qquad (3)$$

where: $E'(\emptyset)$ = the array factor of an array of N linear elements,
N = the number of elements,
A_n = the nth amplitude excitation coefficient,
u = k S cos $\emptyset$,
k = $2\pi/\lambda$,
S = element spacing.

If the comparison between (1) and (3) is limited to one plane, it becomes apparent that the only significant distinction between the two equations is the form of the argument. In the instance of the ring array, the argument is simply $\emptyset$, the azimuth angle. However, in the case of the linear array, the argument is u(=k S cos$\emptyset$). Except for limits then, it follows that the same degree of freedom exists in both cases for synthesizing patterns. The basic problem heretofore with the cylindrical array has been the absence of a technique which would allow separable excitation of the individual terms of equation (1). In the linear array this separable excitation is a simple matter since each term represents the contribution of a single element. In the circular array, the complex spacial arrangement does not allow the individual elements to represent the individual terms of equation (1). However, if a method were generated

for separately and independently exciting each of the terms of (1), it would follow that the problem of synthesizing beams from a cylindrical array would be no more difficult than synthesizing beams from a linear array.

It will be shown later that the individual terms, or expressions of equation (1), may be separably excited. However, in the general case, no term can be excited without some content of the remaining terms existing. To examine the degree of imperfection in any given mode, it is necessary to theoretically analyze the phase and amplitude characteristics of a given mode.

The Fourier synthesis of patterns from circular arrays has been the object of considerable study during the course of the last few years. A synthesis technique utilized by Taylor[4] traced the steps from the required pattern to the element coefficients, and an intermediate expression for the pattern involving a complex Fourier series was formulated. Although Taylor did not directly state that there was a limit on the allowable phase progression, he did indicate that the array size very sharply limits the highest order term that can be realized in the Fourier series. The result is that the progressive phase excitation radiates the desired terms predominantly with higher order terms entering as unwanted perturbations. The magnitude of these perturbations can be evaluated by the method of TaShing[5] for in-phase arrays. When this expression is modified to take into account the progressive phase of the excitation, the

following equation is obtained for the pth term:

$$E_p(\theta, \emptyset) = N \left\{ \sum_{n=0}^{\infty} A_n (p-n) \frac{d^n}{dz^n} \left[J^p(Z) \right] e^{jp\emptyset} \right\} \quad (4)$$

$$+ N \sum_{x=-\infty}^{\infty}{}' \left\{ \sum_{n=0}^{\infty} A_{nj} (p-n-N_x) \frac{d^n}{dz^n} \left[J(p-N_x) \right] e^{j(p-N_x)\emptyset} \right\}$$

where: $E_p(\emptyset, \theta)$ is the relative pattern of the pth mode,

J_p is a bessel function of order p,

Z $= (2\pi r/\lambda) \sin \theta$,

N $=$ number of elements,

n is an integer.

The prime on the summation indicates that the term $x = 0$ is excluded. The element pattern, which has been integrated into the above expression, is expressed as a Fourier series of the form,

$$E_e(\emptyset, \theta) = \sum_{n=-\infty}^{n=+\infty} A_n(\theta) e^{jn\emptyset} \quad (5)$$

where the amplitude coefficient A_n is a function of elevation angle.

The first bracketed expression of equation (4) is the desired far-field characteristic. The second part of the equation represents the un-wanted residuals which cause undesired amplitude and phase distortion of the desired mode. The first section has an amplitude which is independent of azimuth angle, and has a phase characteristic which increases linearly

with increasing azimuth angles. A significant factor is the relative phase of the expression as a function of p, the mode number. The j term is raised to the (p-n) power, so that for any two given modes, a fixed-phase differential will occur. Thus, in order to correlate the modes properly, a fixed-phase correction will have to be inserted in each port. The magnitude of this fixed-phase difference will be a function of the element patterns and spacings. If the element patterns remain reasonably constant with frequency, the fixed-phase shift will, in turn, vary little with frequency; thereby allowing for the possibility of broadband operation.

It is interesting to note that the maximum value of p is N/2 which corresponds to a 180 degree phase shift from element to element. For this value of p, it is impossible to excite an $e^{j(N/2)\phi}$ term without also exciting a complimentary residual of $e^{-j(N/2)\phi}$. The sum of these two terms is equal to $\cos(N\phi/2)$ (ignoring higher order residuals), indicating that the far-field pattern has nulls and maxima equal in number to the value of N. Another factor of interest is that the pattern mode with the next highest residual content is $E'\left[(\,(N/2)-1)\right]\phi$ which has an associated perturbation of order $-(N/2 + 1)$. It is here that the cutoff effect can be seen in terms of the Bessel function of argument z. With an increase in the order of p, $J_p(z)$ increases and, since Bessel functions decay rapidly for values of the argument less than the order, z must have

a larger value to avoid cutoff. It is also easy to see why the $E_o(\emptyset)$

pattern (in-phase array) has the optimum omnidirectivity because its

first residual term has the highest order $----\pm N$.

The mode characteristics, as represented by equation (4),

have been tabulated on an IBM 7090 computer for arrays of 8, 16, 32,

and 48 elements. These mode characteristics were tabulated for theo-

retical element patterns of the form

$$E(\emptyset) = \cos^r (\emptyset),$$ (6)

where r was made to range from 0 to 16. Computed data have also been

tabulated for experimentally measured element patterns in the instance of

both the 8 and 16 element arrays. In all of the above instances, an ele-

ment spacing range from 0.25 to 0.75λ has been investigated. These

tabulations are much too extensive for this report but may be found in

references 1 through 3. The computed data of Figure 5 is exemplary of

the curves obtained from the expression of equation (4). The curves rep-

resent the tabulated data for the instance where r = 16 and where N, the

number of elements, is also equal to 16. The graph of Figure 5(a) repre-

sents the minimum-to-maximum voltage ratio (ρ) in the azimuth plane as

a function of mode number. The curve of Figure 5(b) represents the phase

deviation from the desired phase progression as a function of mode number.

The mode number is of the form 0m or m0, where m represents the number

of 2π phase progressions about the array periphery. In the former instance,
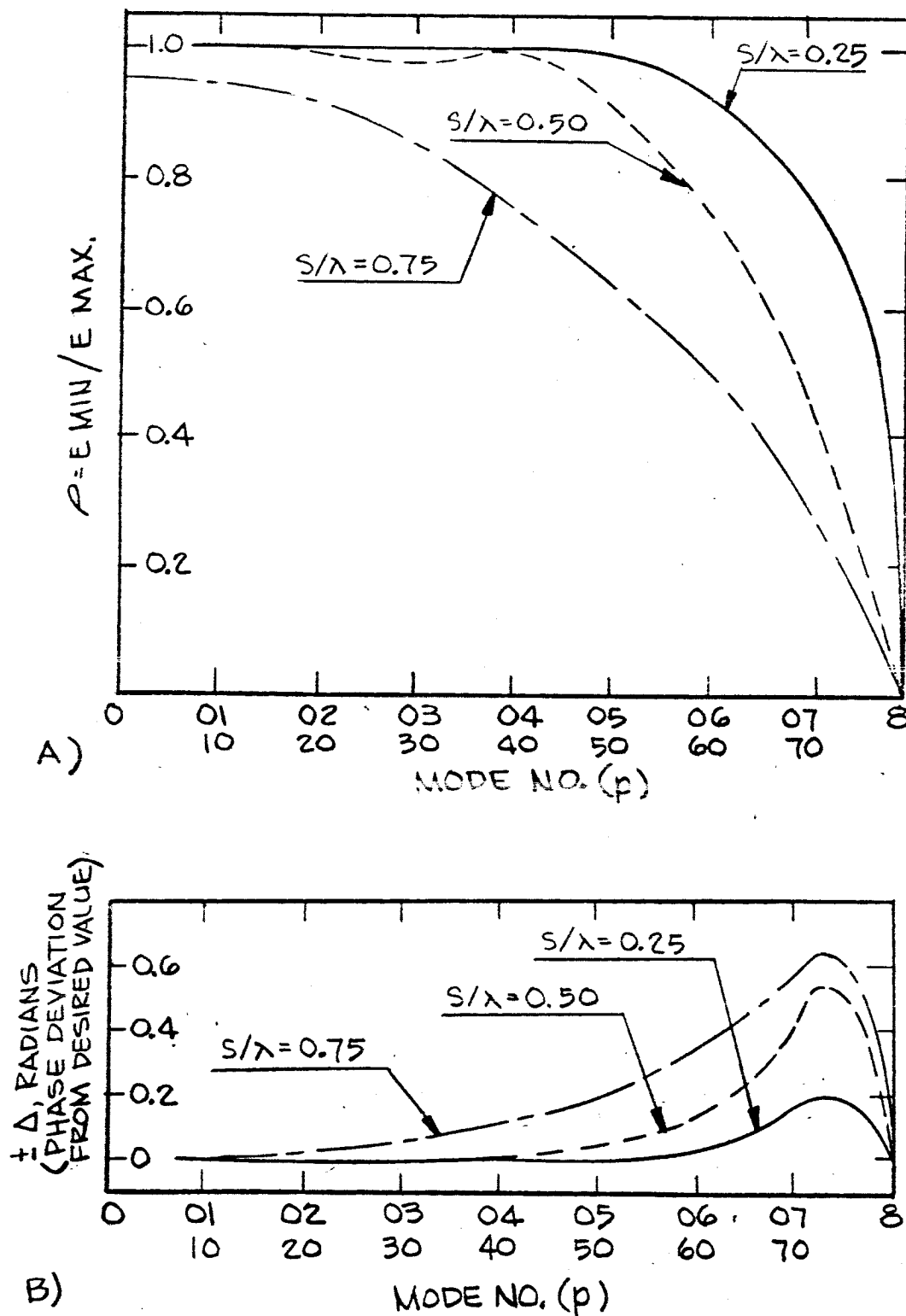
Figure 5. Mode purity in terms of amplitude a) and phase deviation b) for an element pattern of the form $\cos^{16}\phi$.

the notation indicates that the progression is clockwise, as viewed from the top of the array; in the latter instance, the notation indicates that the phase progression is counter-clockwise. It should be noted that, while the curves of Figure 5 are shown as continuum, in actual fact they are only valid for integral values of p. Generally, all of the data computed from equation (4) has the same format as that of Figure 2, differing only in detail. In all instances, the amplitude and phase deviations increase with increasing mode number, increasing element spacing, and increasing element beamwidth.

A typical set of voltage amplitude patterns is plotted in Figure 6 for the conditions assumed in Figure 5, and for the case where the spacing is equal to 0.5λ. The plot is shown over the range from $\emptyset = 0$ to $\emptyset = 1.6$ radians. The full range of $\emptyset$ is not included, since the functions are periodic over increments of $\pi/8$ radians.

The definition of the individual mode patterns represents an intermediate step for the computation of the eventual far-field patterns which will be formed by judiciously combining the modes. While the data of Figures 5 and 6, and the expression from which the data were evolved is rigorous, it does not allow for simple programming even by computer processing standards. Since the rigorous expression represents an unwarranted amount of programming, it is desirable to seek an expression which would approximate the computed mode patterns, but which would be more amenable to
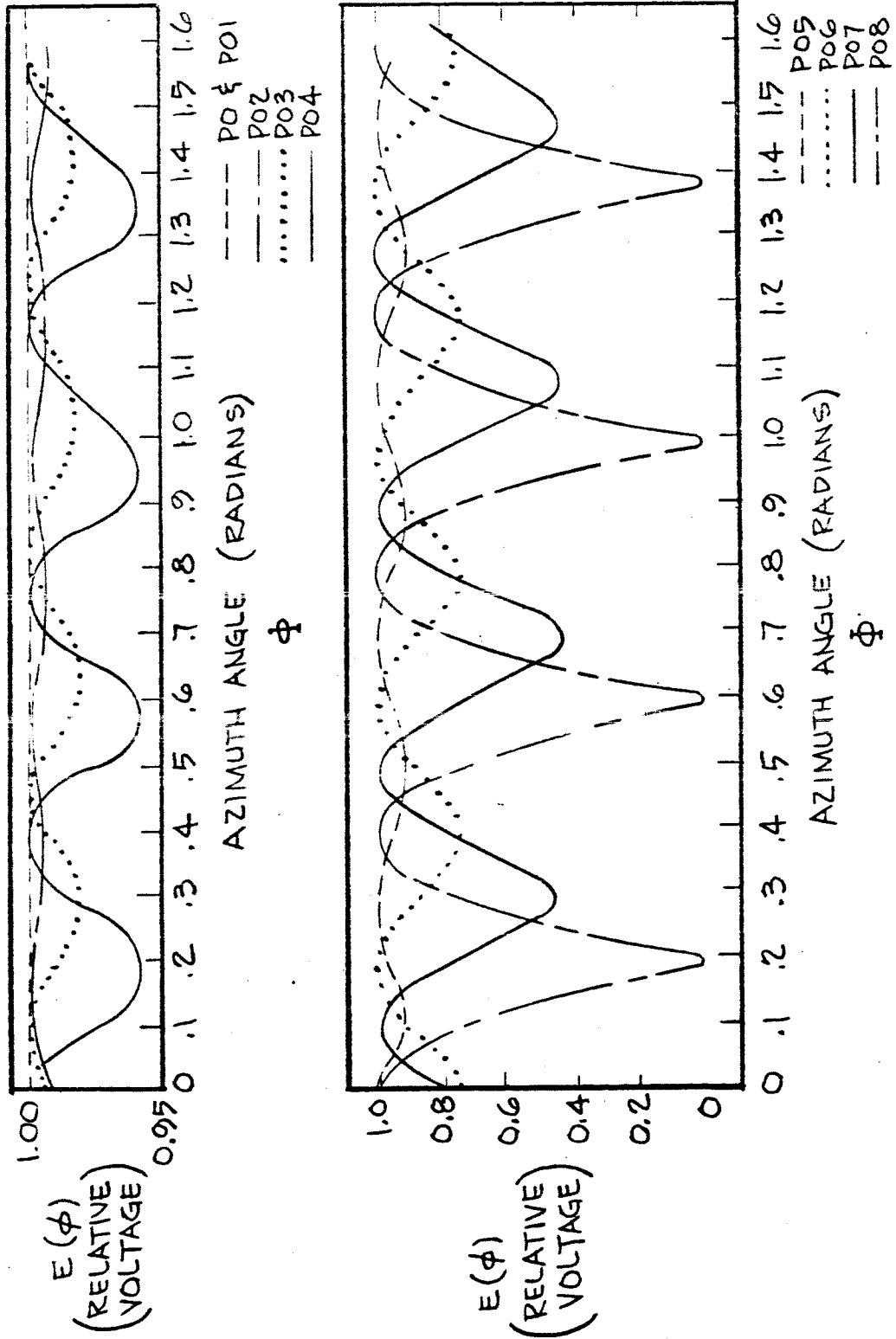
Figure 6. Voltage patterns vs. azimuth angle for conditions of Figure 5.

simple programming. The general expression for this approximation could then be summed for eventual synthesis by further processing networks. This expression may be written as:

$$E(\emptyset, p) = \left\{ e^{j\delta p} \left[e^{j\emptyset p} + k_p e^j \left[\emptyset p(1 - N/|p|) + p y_p/|p| \right] \right] \right\} \left[1 + k_p \right]^{-1} \quad (7)$$

where: δ_p is the base reference phase for each mode,

       y_p is the phase parameter which defines the position of the first amplitude minimum relative to element number 1 $(n = 1)$,

       k_p is the amplitude of the perturbing higher order mode.

The value of k_p may be defined or derived from the simple relationship:

$$k_p = (1 - \rho)/(1 + \rho), \quad (8)$$

where ρ is the ordinate of Figure 5. The position of the first pattern minima for each mode, relative to element number 1, may be taken directly from the earlier described computed data. The use of this latter parameter now insures that the amplitude deviations are not only correct, but are also properly oriented. In reference 3, a number of test cases, utilizing an expression similar to equation (7),were analyzed. In all instances the deviations between the patterns predicted by the computer, using the approximate expression, agreed within 1.5 percent of the data obtained using the rigorous expression of equation (4).

The approximating expression of equation (7) may now be utilized to examine the mode outputs and compare them with the output of a single element in a conventional linear array. If the value of ρ in expression (8) approaches 0, then the equation simplifies to:

$$E(\emptyset, p)_{k_p \gg 0} = e^{j\delta_p} \left[e^{j\emptyset_p} \right] . \tag{9}$$

This expression is reasonably valid for the lower order mode numbers and for close element spacings. The striking resemblance between the mode pattern of equation (9) and the element contributions in a linear array may be observed by comparison with equation (3). A comparison of equation (3) and equation (9) will indicate that the only significant difference between the two, outside of the element factor, is the argument. In the instance of the circular array, the argument contains only the parameter $\emptyset$. In the instance of the linear array, the argument involves the element spacing and $\sin \emptyset$. Hence, while the circular array expression is not a function of frequency, the linear array term is.

In actual fact, of course, the cylindrical array term is not frequency insensitive. The fundamental, although it does not contain a frequency component, has a perturbing higher-order mode which increases in magnitude with increasing frequency. The question now arises as to the effect of the perturbing term, particularly for the higher-order modes. The number of elements, or equivalent elements, for the circular array could be viewed as being equal to twice the number of the mode terminals. Half of the outputs would consist of the fundamental terms, and the remaining half would consist of the higher-order terms. However, these higher-order terms are inseparable from the fundamental terms, and whatever excitation applies

to the fundamental of a given mode will also apply to the higher-order term. Fortunately, these higher-order terms for most of the modes are highly attenuated and rather random in phase and amplitude. Experience with the synthesis of modes containing perturbing terms has proved that the higher-order terms tend to average, having only a secondary effect on the characteristics of the synthesized beam. The general effect is to slightly distort the main beam with a general improvement in the expected sidelobe level. For example, in reference 3, a synthesis program was established which combined the mode terminals with a Tchebysheff distribution for -25 db sidelobe levels. The performance of the array was theoretically examined over a 50 percent bandwidth. It was found that the sidelobes were less than -26 db, but that the beam tended to have shoulders which caused a variation in the beamwidth.

Some method of exciting all the terms of equation (1) separately and simultaneously is fundamental to the concept of the cylindrical array. The feeding network must excite all of the array elements with equal amplitude for all N input ports. However, the phase progression must vary from one input to another. An N port multiple-beam matrix has this capability. The manner in which this matrix functions has been described in the literature[6, 7, 8, 9] and hence will not be repeated here.

Figure 7 contains the generalized block diagrams for a scanning cylindrical array and for a multiple-beam cylindrical array. In both instances,
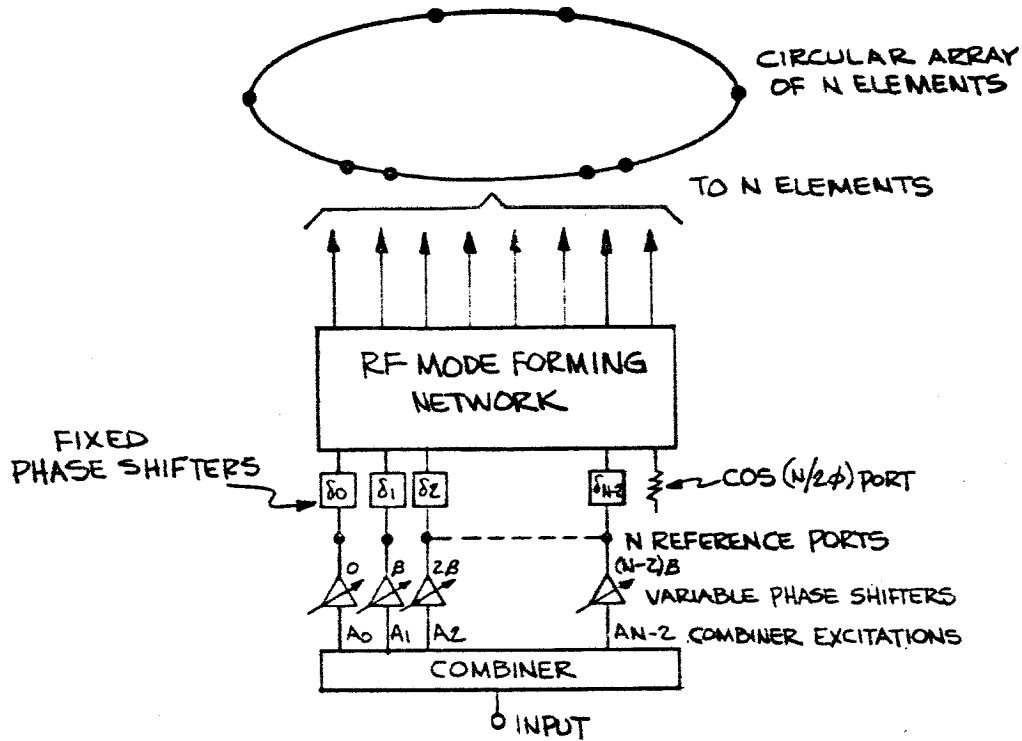
Figure 7(a).   Generalized block diagram of an antenna system with a scanning azimuth beam.
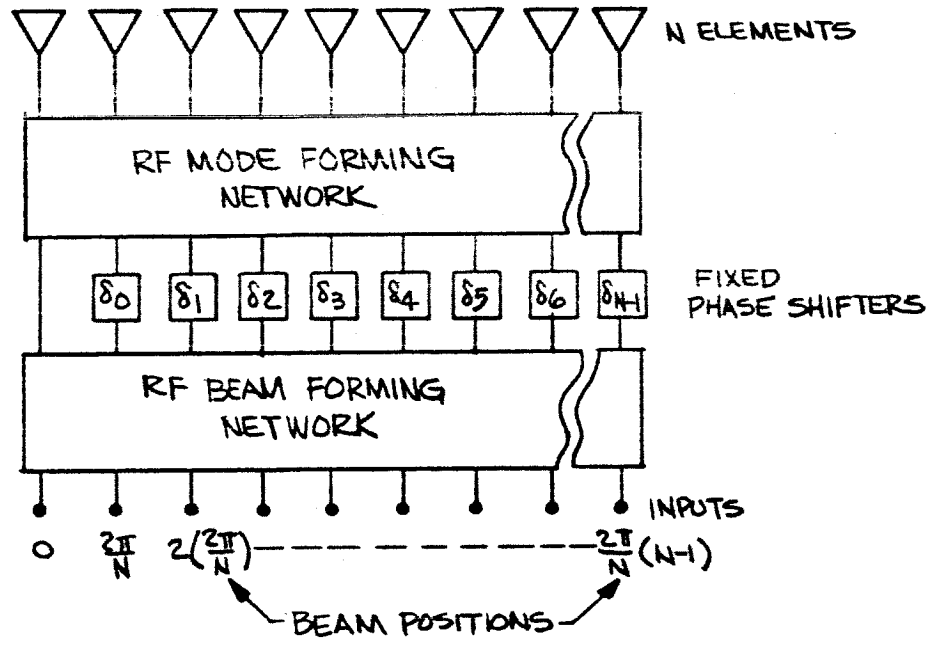
Figure 7(b).   Generalized block diagram of an N element multiple-beam circular array.

the radiating structure is a ring of N elements of arbitrary elevation configuration. The outputs of these N element arrays are processed by an N input - N output matrix. It is these outputs which have the format that is closely related to the format of the expression for a single element in a linear array. The mathematical expression for each of these outputs is given rigorously by equation (4) or by the approximate expression of equation (8). The base phasors are necessary to adjust all outputs to the same phase reference. This base phase correction may be derived from the rigorous expression of equation (4).

When the cylindrical array technique is utilized to form a scanning beam, a conventional matched power divider may be utilized, with in-line phase shifters providing the needed scan parameter. The amplitude coefficients for each of the mode inputs may be controlled to synthesize any desired pattern, by simply controlling the power distribution at the output of the combiner. Note that in the instance of the scanning array, the last term, which generates the N-lobed mode pattern, is not used.

The block diagram of the multiple-beam cylindrical array is similar to that of the scanning array, except that the combiner and the scan control phase shifters have been replaced by a multiple-beam matrix of the same format as the mode-forming matrix. In this latter instance, the last mode can be utilized if the beams are made to lie in the directions of the elements. The outputs of the multiple-beam matrix are equal in number to the number of elements in the array.

The multiple-beam technique generates sidelobes which are theoretically 13 db below the main beam amplitudes. Amplitude tapering techniques presently used in linear arrays for modifying the multiple-beam uniform distribution, can be applied directly to the cylindrical array[1].

The analysis of the cylindrical array is somewhat unusual in that it does not utilize the conventional approach of computing the far-field pattern from the specific element excitations and the geometry of the array configuration. The described technique utilizes the concept of omnidirectional modes which have the same mathematical format as the contributions of single elements in a conventional linear array. It is then presumed that since the mathematical formats are identical, the types of processing used in each instance would also be identical. This mathematical correlation, although not conventional, is particularly convenient in the instance of the cylindrical array. For example, the derivation of the far-field patterns, and the definition of the excitation coefficients from which these patterns are derived, would be mathematically complex and quite tedious, particularly where multiple-beam systems are being considered.

The cylindrical array technique results in element excitations which, if treated in a conventional manner, would yield the same far-field results. Figure 8 aptly illustrates that this is indeed the case. In the instance shown, the excitations are derived for two types of element patterns: one which is omni-directional and the other which is a cardioid. In both instances, the far-field

BEAM DIRECTION

3-4j
(25)

-3   -3
(9)   (9)

-1 (1)   (1) -1

-3 (9)   (9) -3

(25)
3+4j

RADIUS = .73λ
ELEMENT
SPACING = .56λ

ARRAY PATTERN =

$$\frac{SIN\,9\,\phi}{SIN\,\phi}$$

a) ELEMENT PATTERN = 1

BEAM DIRECTION

-.3-5.8j
(34)

4.3-.1j   4.3-.1j
(19.5)   (19.5)

2.7+.3j   2.7+.3j
(7.1)   (7.1)

-1.0-.4j   -1.0-.4j
(1.1)   (1.1)

.7j
(.5)
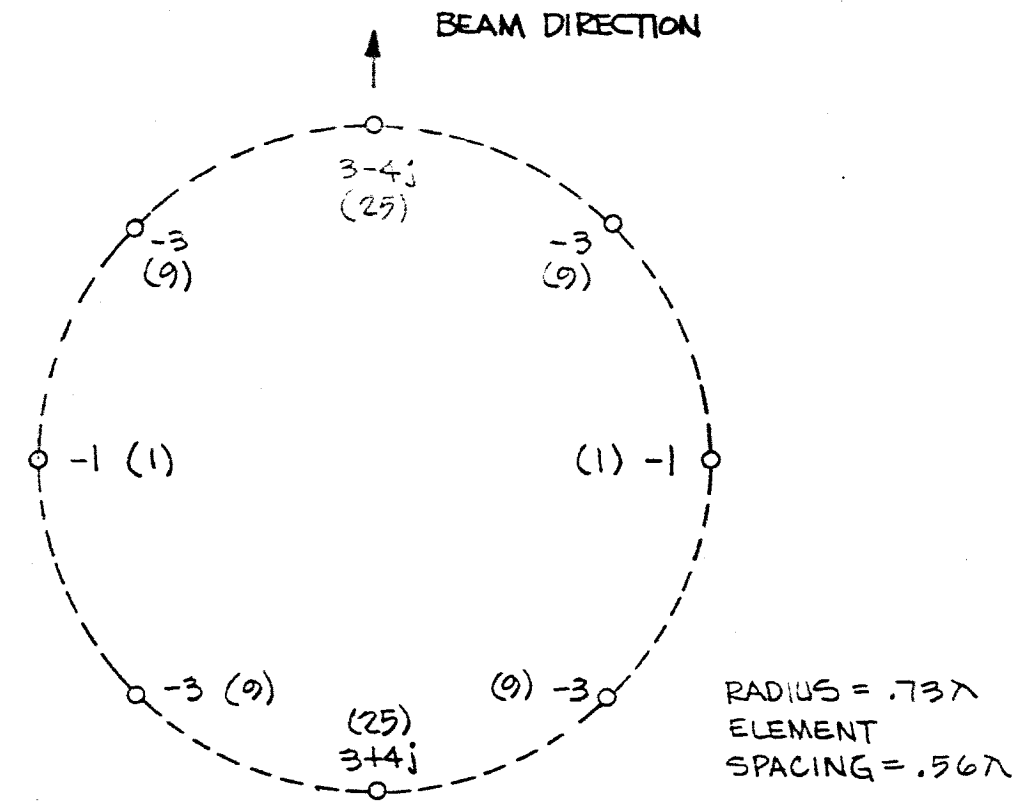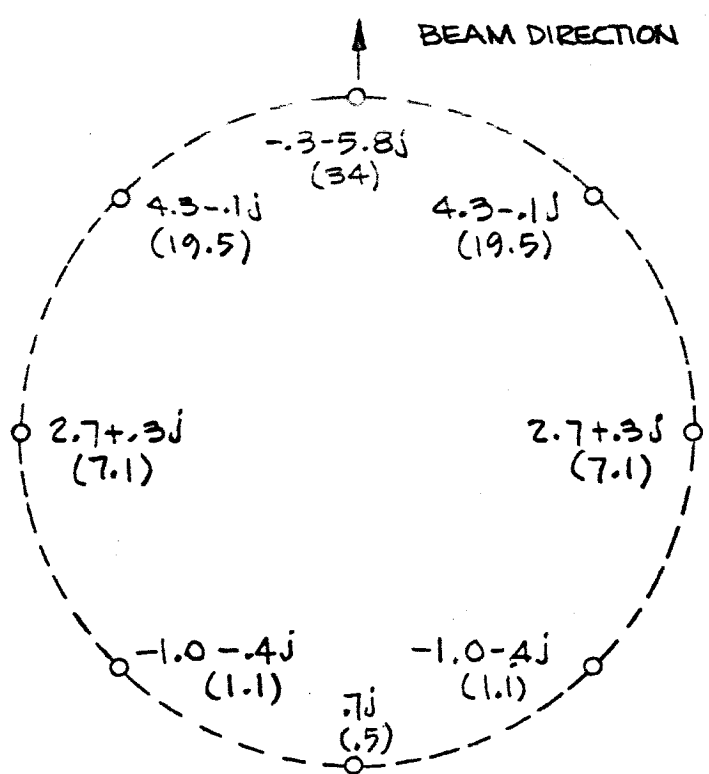
b) ELEMENT PATTERN = 1 + cos φ

Figure 8. Element amplitudes and (powers) for two types of element pattern.
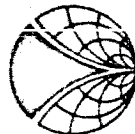
pattern could be computed in the normal manner to achieve the same far-field results as is achieved with the above analysis. The character of the excitation coefficients is markedly affected by the element pattern. In the case of an omnidirectional element pattern, the power appearing at the element terminals is equally strong in the direction of the beam pointing and in the reverse direction. For the case where a cardioid pattern is assumed, the energy appears at the element terminal in the direction of the beam pointing, with very little appearing in the reverse direction.

The next section of the report will treat the detailed design of the specific 4 x 16-element multiple-beam system which was developed for the program.

3.2.2 Detailed Design

The preceding paragraphs have described the general design criteria and the theory of operation for the cylindrical array concept. The purpose of this section is to apply these concepts to the specific design of the 4 x 16-element array.

The first phase in the program was to measure the element patterns of the spiral cavity radiator at frequencies of 1700 and 2270 mc, for both horizontal and vertical polarizations. The results obtained will be discussed later in Section 3.2.3.1. The observed experimental patterns were then reduced to elemental Fourier form. The approximating Fourier expressions

for the experimental patterns are listed below.

Case I: Frequency 2.27 kmc, polarization $E_{\emptyset}$ (or horizontal)

$$E(\emptyset') = 0.356 + 0.463 \cos \emptyset' + 0.137 \cos 2\emptyset' \quad (10)$$
$$+ 0.042 \cos 3\emptyset'$$

Case II: Frequency 2.27 kmc, polarization E_θ (or vertical)

$$E(\emptyset') = 0.320 + 0.459 \cos \emptyset' + 0.191 \cos 2\emptyset' \quad (11)$$
$$+ 0.034 \cos 3\emptyset'$$

Case III: Frequency 1.7 kmc, polarization $E_{\emptyset}$

$$E(\emptyset') = 0.399 + 0.428 \cos \emptyset' + 0.129 \cos 2\emptyset' \quad (12)$$
$$+ 0.058 \cos 3\emptyset' - 0.013 \cos 4\emptyset'$$

Case IV: Frequency 1.7 kmc, polarization E_θ

$$E(\emptyset') = 0.321 + 0.486 \cos \emptyset' + 0.164 \cos 2\emptyset \quad (13)$$
$$+ 0.012 \cos 3\emptyset' + 0.029 \cos 4\emptyset' - 0.029 \cos 5\emptyset'$$

where $E(\emptyset')$ = element voltage pattern relative to element axis.

The correlation between the above synthesized expressions and the observed experimental data were excellent. Examination of the above expressions will indicate that for some functions it was necessary to utilize more terms than for others. The number of terms required was simply determined by increasing the number of terms until the desired degree of correlation was obtained. The above functions were next utilized in the
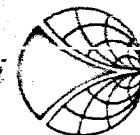
formula of equation (4) to compute the mode pattern characteristics. Cases I and II above were examined for element pattern spacings of 0.6 and 0.7λ. Cases III and IV were examined for element spacings of 0.4 and 0.5λ. These element spacings were reasonably consistent with the spacing allowed by the geometry of the spiral cavity element and by the specified range of frequencies. The solution to equation (4) for each of the four cases cited and for the element spacings investigated, were obtained by using an IBM 7094 computer. The mode omnidirectivities, for each of the investigated cases, are plotted in Figures 9 through 12. Examination of the computed data will indicate that the mode omnidirectivity decreases more rapidly as the spacing is increased and as the beam resolution decreases. Computed data which were recorded, in addition to the maximum to minimum amplitude deviations for each mode, were the base phase for each mode and the position of the maxima for each mode.

The computed mode data were next reduced to the format of equation (7) in order that the far-field patterns of the total system could be computed. The beam patterns were computed, using the summation format

$$E(\emptyset) = \sum_{p=-(N/2)}^{p=(\frac{N-2}{2})} e^{j\delta_p} A_p (1 + k_p)^{-1} \left[e^{j\emptyset_p} + k_p e^{j} \left[\emptyset_p(1 - N/|p|) + p y_p/|p| \right] \right] \quad (14)$$

where: p   is mode number = -8, -7, -6, . . . 0, 1, 2, . . . 7,

   N   = the number of modes = 16,
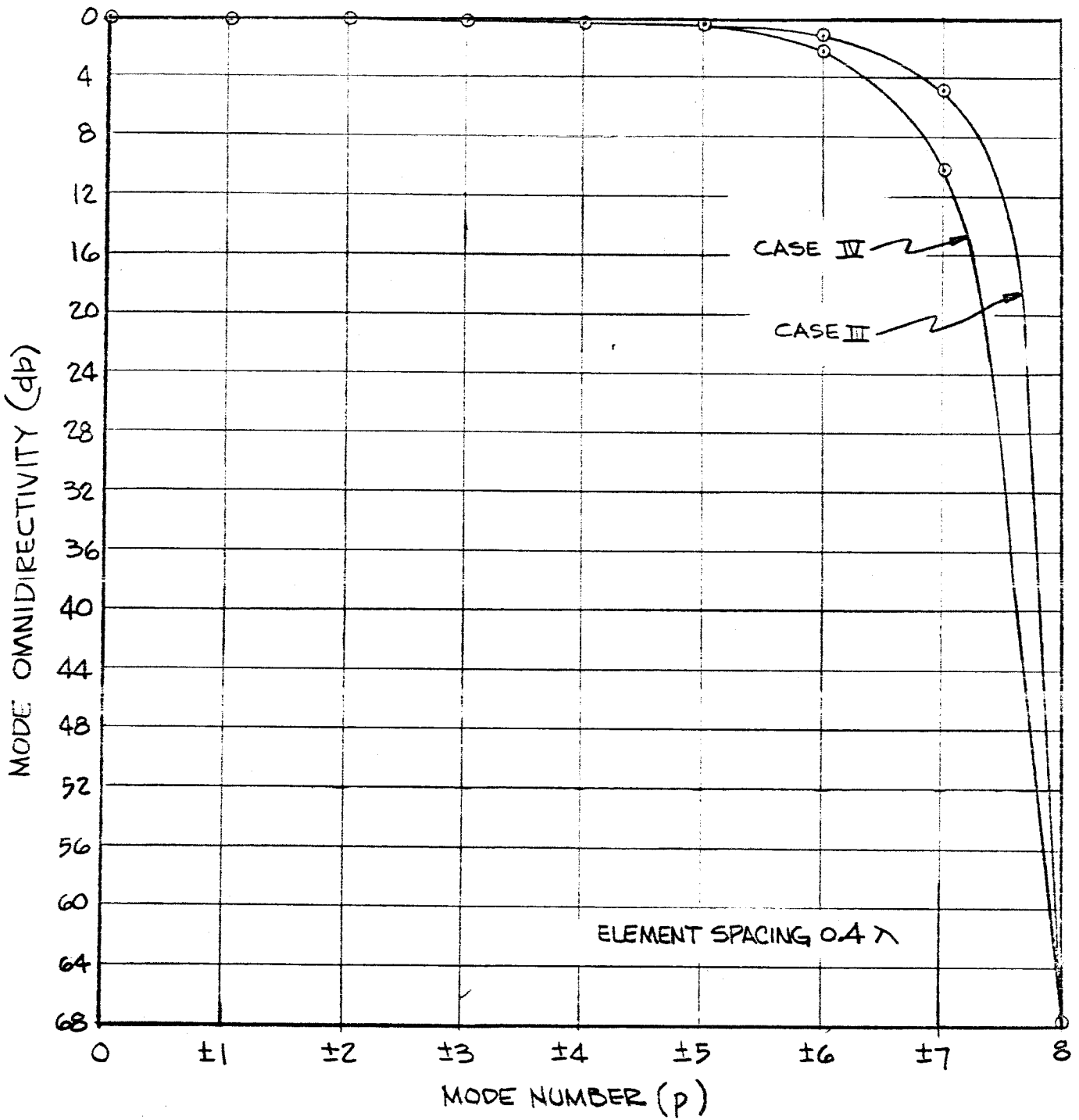
Figure 9.   Computed mode omnidirectivity for cases III and IV.
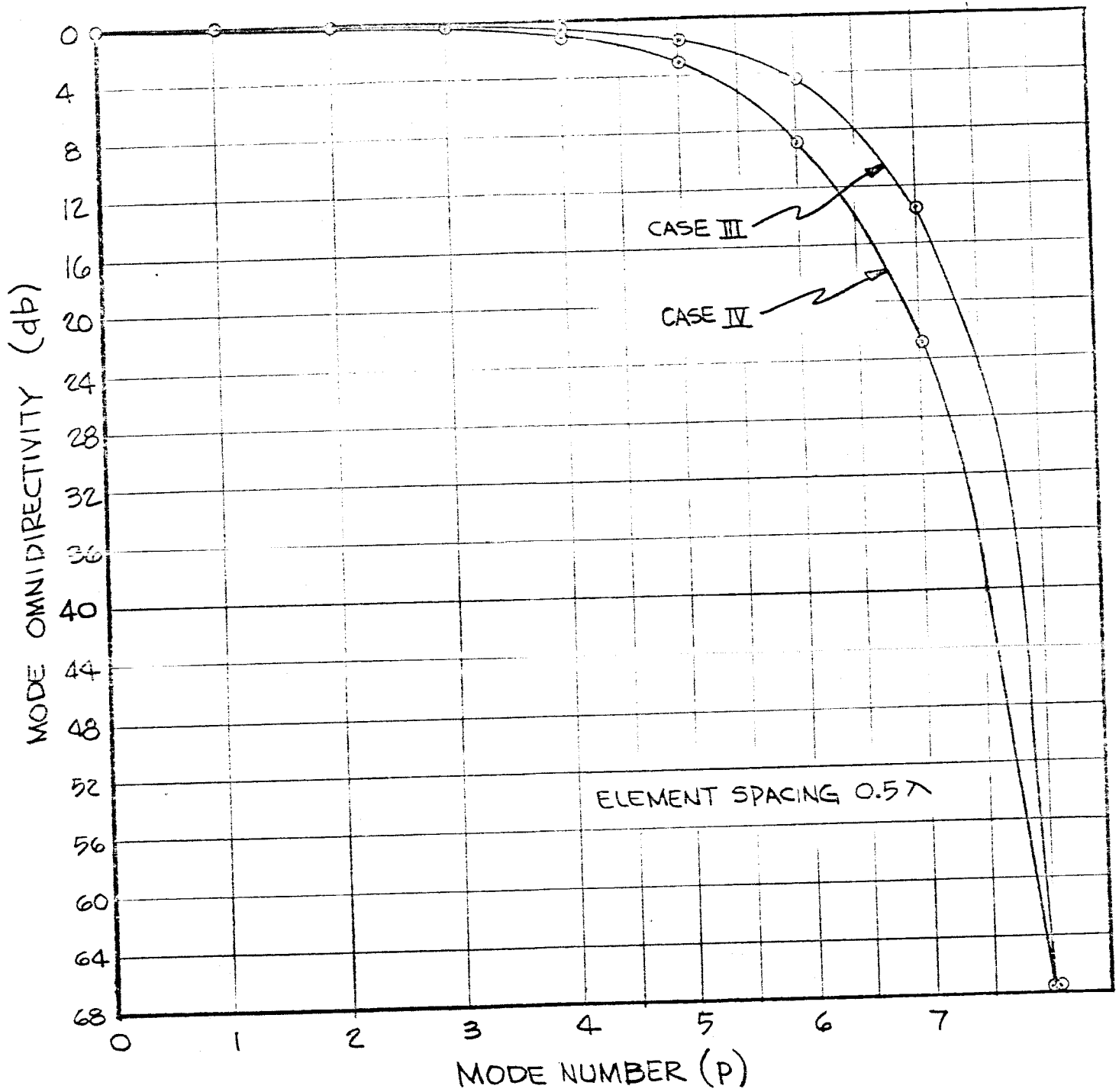
Figure 10. Computed mode omnidirectivity for cases III and IV.
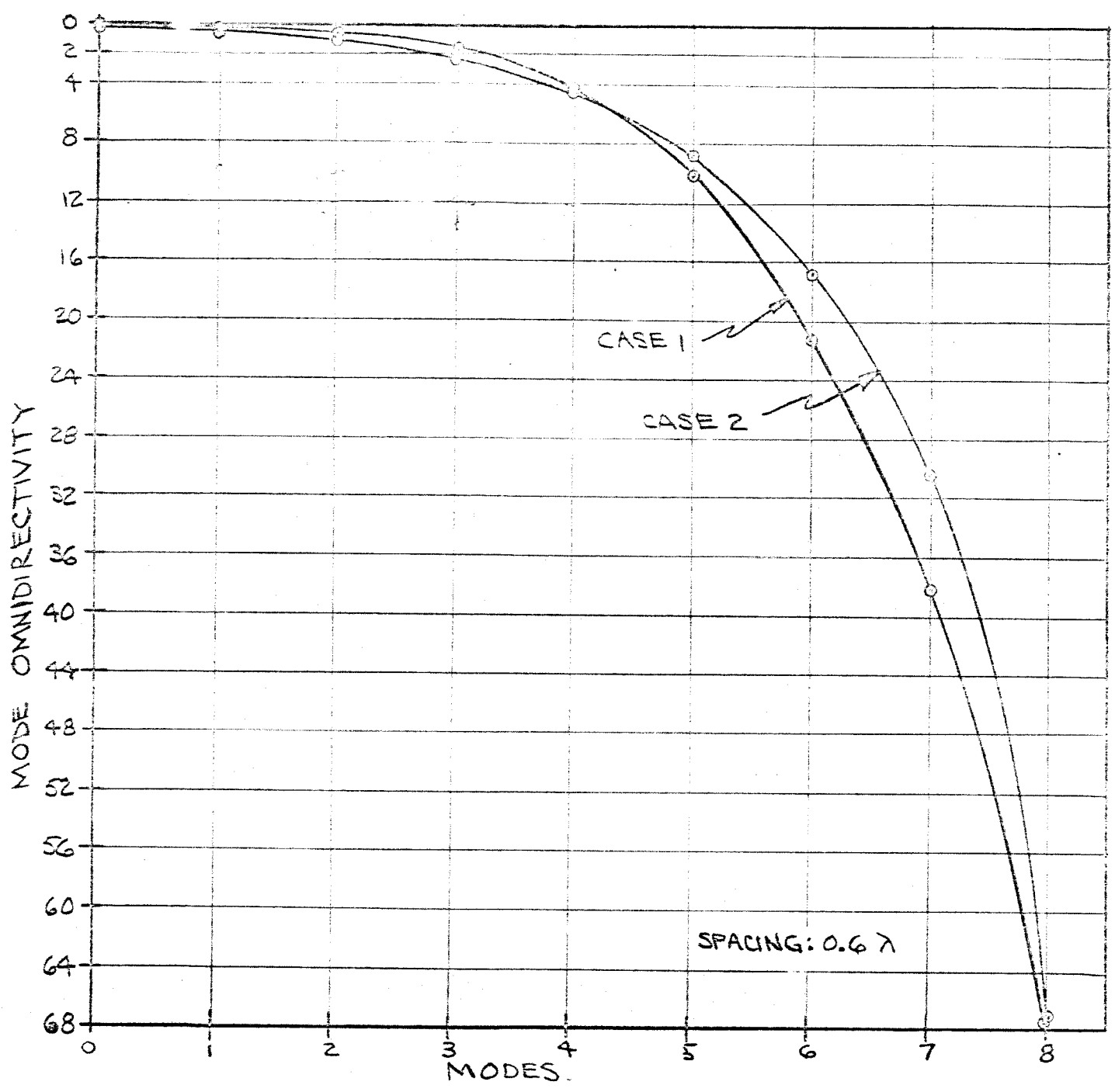
Figure 11. Computed mode omnidirectivity for cases I and II.
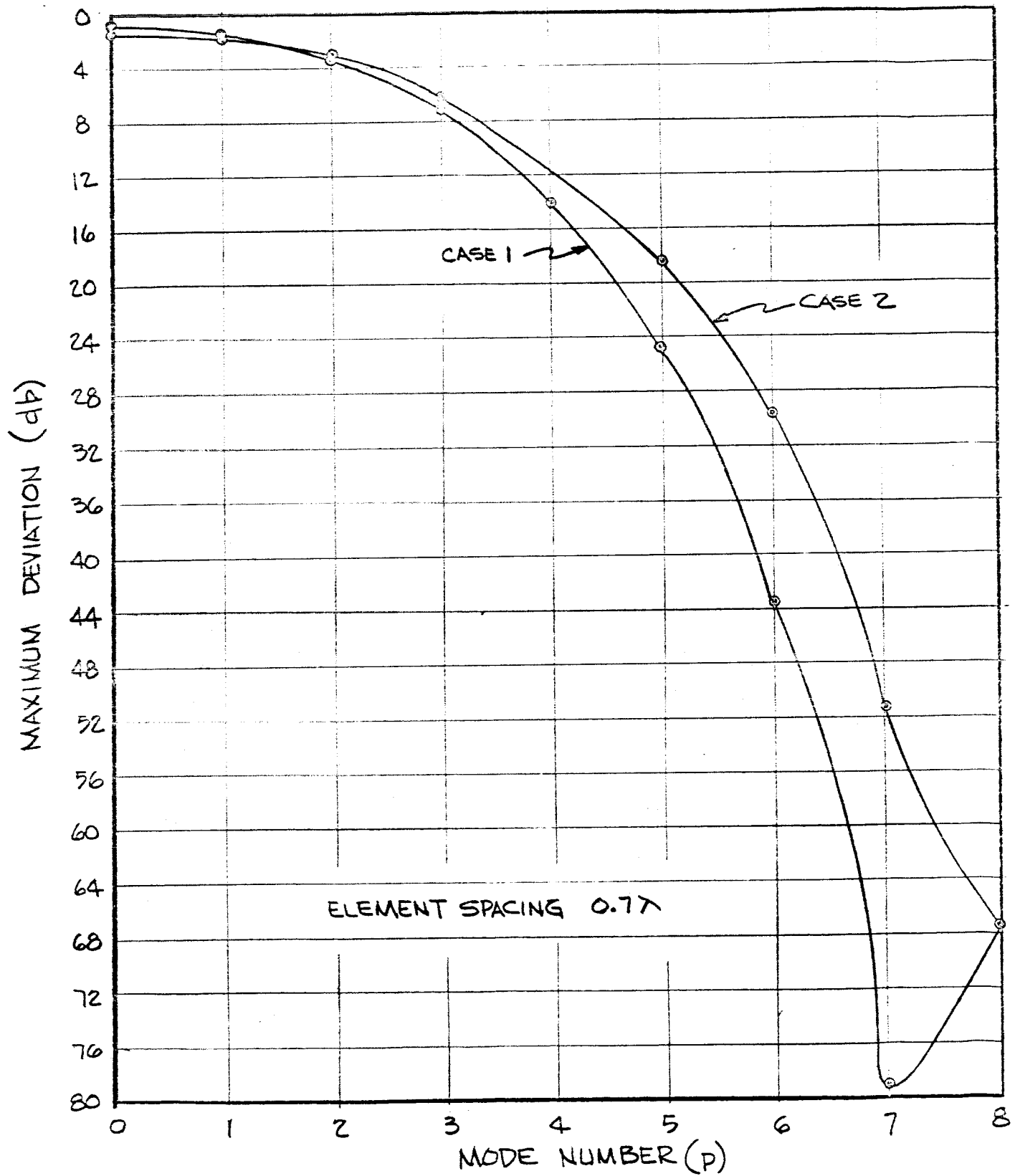
Figure 12.   Computed mode omnidirectivity for cases I and II.

δ_p is the base reference phase for each mode,

k_p is the amplitude of the perturbing higher order mode,

A_p is the directivity of the pth mode,

p is the relative phase parameter,

$\emptyset' = (\emptyset - \beta)$,

β is the variable inter-port phasor,

$\emptyset$ is the space angle, varies from $0°$ to $360°$.

The above expression was utilized to compute the far-field patterns for cases I through IV. Here again, the element spacings of 0.4 and 0.5λ correspond to cases I and II with cases III and IV related to the element spacings of 0.6 and 0.7λ, respectively. The base phasors were assumed compensated by the best possible r-f cable length. The best cable length, for each mode, was a constant factor for cases I and III. The best cable length was selected, for the above cited instances, to compensate the base phase, for each mode (which is a function of polarizations and the element spacings since they are interrelated by virtue of the frequency spread and the fact that the horizontal and vertically polarized patterns were obtained at a given antenna terminal. The same concept for base phase correction was used for cases II and IV, with element spacings of 0.5 wavelengths and 0.7 wavelengths, respectively. The realized-computed patterns for cases I and II, with a spacing of 0.7λ, are plotted in Figures 13 and 14. The corresponding pattern for cases III and IV, at a spacing of
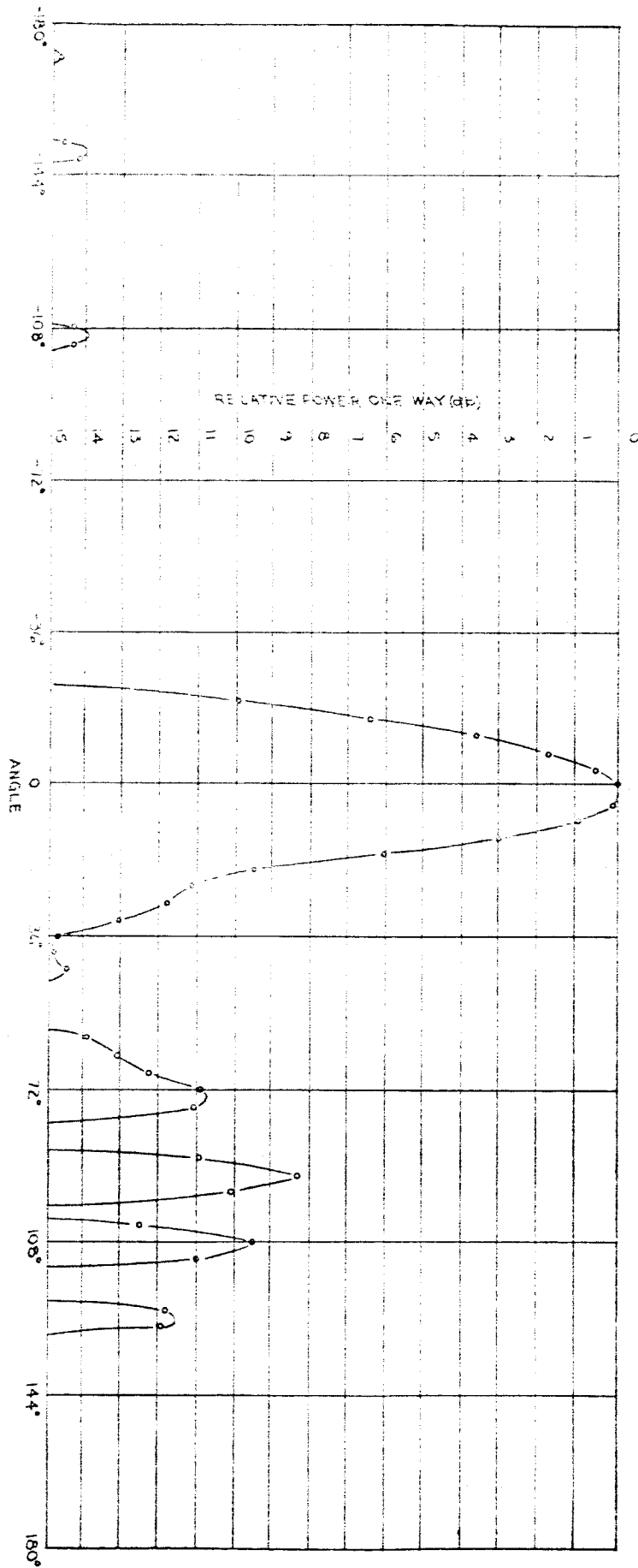
COMPUTED BEAM PATTERN FOR
CASE I WITH 0.7 λ SPACING
(β=0° BEAM POSITION)

P44

RELATIVE POWER ONE WAY (db)

ANGLE
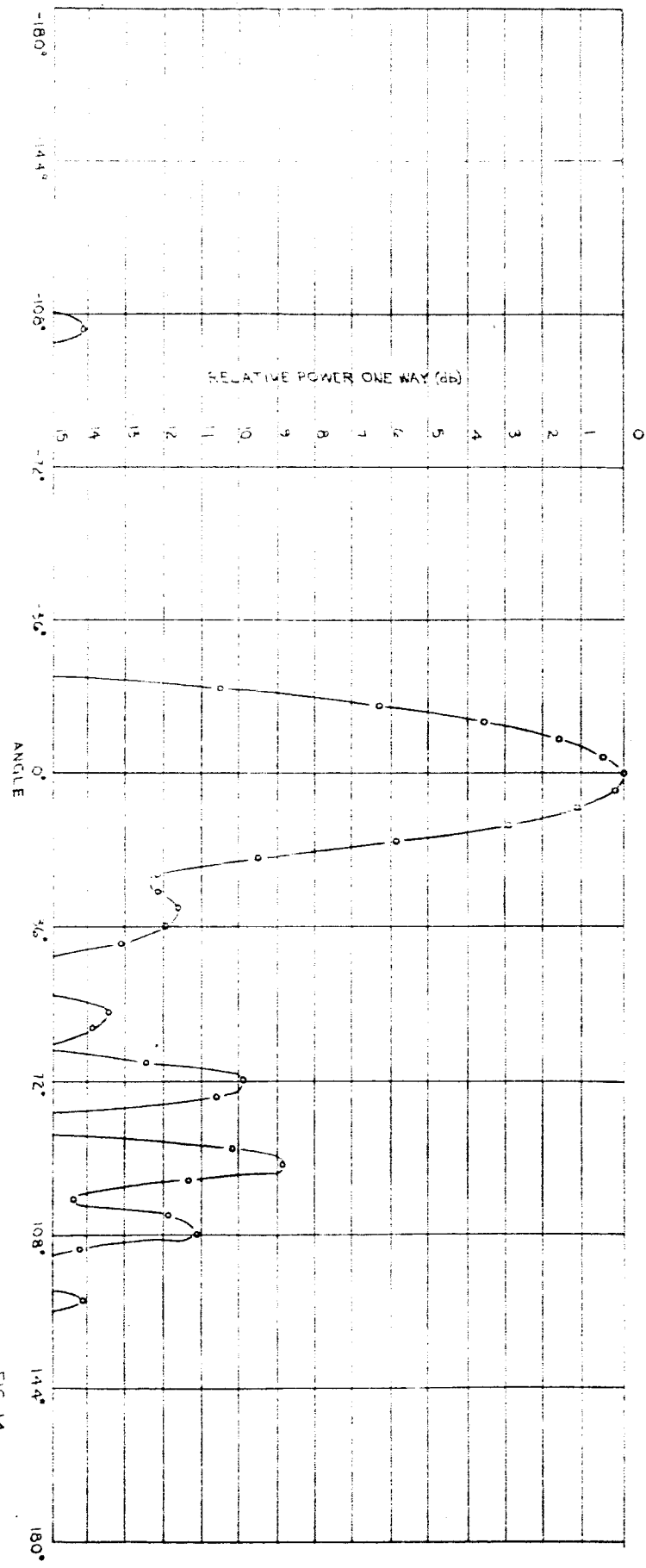
FIG. 14
COMPUTED BEAM PATTERN FOR CASE III
WITH 0.1 λ SPACING (β=0° BEAM POSITION)
P45

0.5λ, are plotted in Figures 15 and 16. The computed pattern of Figure 13 represents the case of horizontal polarization at an approximate frequency of 2270 mc. The beamwidth is approximately 20 degrees. The maximum observed sidelobe level is -8.5 db, in one instance. A second sidelobe magnitude of -9.6 db is also evident. All other sidelobes are below 10 db. Figure 14 represents the case for the vertically polarized pattern at an approximate frequency of 2270 mc. The beamwidth is again approximately 20 degrees, with a maximum observed sidelobe level of -8.9 db. With the exception of a secondary maximum sidelobe level of -9.8 db all other sidelobes are below 10 db. Figure 15 represents the case for the horizontally polarized pattern, at an approximate frequency of 1700 mc. The beamwidth is again approximately 20 degrees. In this instance, the maximum sidelobe level is 10.3, relative to the main lobe maximum. All other sidelobe levels are below 11 db. Figure 16 represents the instance where the pattern is vertically polarized and the frequency is 1700 mc. The maximum observed sidelobe for this case is 12.2 db. The beamwidth is again approximately 20 degrees.

All of the computed data shown in Figures 13 through 16 are for the variable inter-port phasor (β) equal to zero. Computed patterns were also obtained for four other typical beam positions. In each instance, it was noted that the maximum sidelobe level varied by approximately $\pm$1/2 db about the above cited values as the beam position varied in space.

RELATIVE POWER ONE WAY (DB)

ANGLE
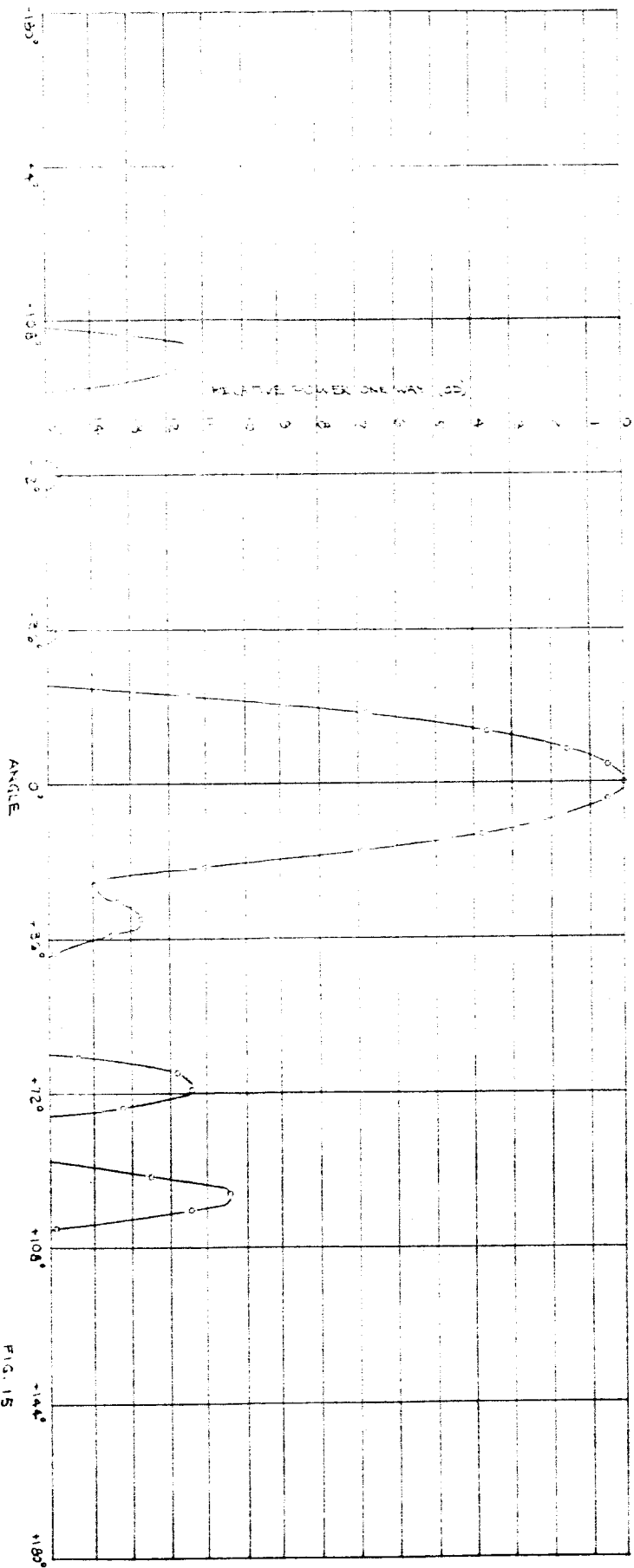
FIG. 15
COMPUTED BEAM PATTERN FOR CASE III
WITH 0.5λ SPACING (3.0° BEAM POSITION)

P. 47

RELATIVE POWER ONE WAY (DB)

ANGLE
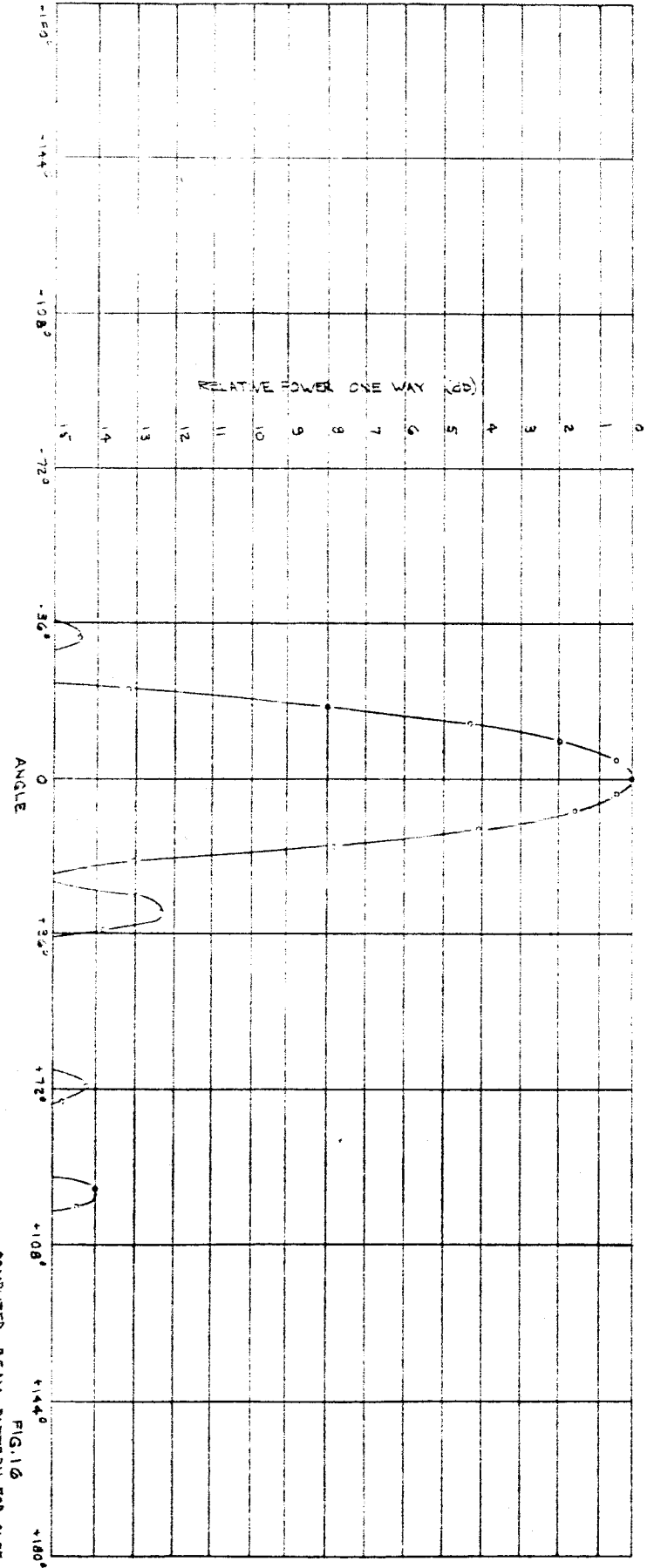
FIG. 16
COMPUTED BEAM PATTERN FOR CASE II
WITH 0.5 λ SPACING (8·0° BEAM POSITION)

P. 48
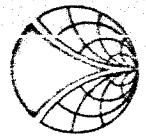
The computed pattern data indicate that the sidelobes are greater than the theoretical value of approximately -13 db for the instance where all modes are perfectly omnidirectional, and where the phase compensation between modes is perfect. It is believed that the increased sidelobe levels are more attributable to imperfect phase compensation than to the deviation from omnidirectivity. Fixed phase shift corrections, combined with cable length corrections, would tend to improve the sidelobe levels, however this degree of complexity was not within the scope of the present program. The sidelobes could be improved at the expense of a slightly reduced aperture efficiency by introducing a slightly tapered distribution. Examination of the patterns indicate that the half-power beamwidth is frequency independent, which is as predicted for the circular array.

Computed pattern data were also obtained for element spacings of 0. 4 and 0. 6λ. This data proved to be impractical since the required element size would not allow the close spacing of 0. 4λ, at the lowest operating frequency. The computed patterns, for these spacings, indicated that the sidelobe levels were somewhat improved.

It was originally planned that the impact of component imperfections on pattern performance be analyzed mathematically through the medium of a 7090 computer. The computer program for this analysis was completed and implemented. It was found, however, that the results derived from the computer indicated that the necessary mathematical formulae had been mis-programmed.

During this same interim of time, the component effort was very nearly completed. The component data indicated that the results were close to the theoretical limits for the components being used. Since it was felt that little could be done to improve the component performances, and further, since an engineering schedule had to be met, it was decided to curtail any further analysis relating to the effect of component errors on system performance. The alternate approach of deriving the best possible component performance was taken in lieu of this analysis.

The design of the vertical banks of four elements was generally dictated by the element size and spacing selected for the azimuth plane cylindrical array patterns. Since the design of such a vertical array is mundane, it will not be detailed in this report. However, a comparison of the obtained data and the predicted data (based on conventional array analysis) will be made in Section 4.0.

3.2.3 Network Components

The objective of this part of the report is to describe the design and performance characteristics of the major components which form the cylindrical array portion of the antenna system. The major components which will be discussed are listed below:

a) Spiral antenna elements

b) Sixteen-port mode and beam forming matrices

c) Four-port beam forming matrices

d) Mode correction network

e) Four-port switching network for the vertical array banks

f) Sixteen-port switching network.

The above components will be discussed, in chronological order, in the following subsections of the report.

3.2.3.1 Antenna Element

A total of sixty-four spiral cavity antenna elements were utilized to implement the cylindrical portion of the developed antenna system. These spiral cavity elements were based on a design described in the literature by Bawer and Wolfe[10]. The cavity surface was square in cross-section with the side dimension of the square being equal to 3.5 inches. The spiral surface was housed in a square cavity having a depth of 1.05 inches. The performance characteristics of a typical spiral cavity element are listed below:

Frequency:	1.7 KMC	2.3 KMC
3 db BW –		
E_ϕ:	87°	74°
E_θ:	82°	78°
10 db BW –		
E_ϕ:	195°	142°
E_θ:	164°	148°
Axial Ratio:	1.3 db	1.9 db
VSWR:	1.24	1.19

The above data were obtained with TNC connectors which were modified to

adapt to the balun which excites the spiral surface. This TNC connector was subsequently removed and replaced by a female center pin and a specially developed outer coaxial housing. This latter arrangement allowed the four spirals in each vertical bank to be made an integral part of the exciting four-port multiple-beam elevation matrix.

3.2.3.2 Sixteen-Port Beam and Mode Forming Matrices

Reference to Figure 3 will indicate that a sixteen-port mode forming matrix and a sixteen-port beam forming matrix are required to implement the cylindrical array. The mode forming matrix establishes the pseudo omnidirectional modes which are, in turn, processed by the beam forming matrix to form the sixteen azimuth plane beams. The interconnecting elements between these two modules are the mode phase correction cables which will be discussed in a later section. The block diagram of the mode forming and beam forming matrix are identical. This block diagram is detailed in the sketch of Figure 17.

The relationships between the terminology of Figure 17 and both the omnidirectional modes and multiple-beam positions are defined in the table below.

		16 Port Matrix Notation	
Port No.	Mode	Beam Direction (ϕ)	Inter-Element Phase Progression
0		0°	0°
10		$22\ 1/2^\circ$	$22\ 1/2^\circ$
20	Same as port no.	45°	45°
30		$67\ 1/2^\circ$	$67\ 1/2^\circ$
40		90°	90°
50		$112\ 1/2^\circ$	$112\ 1/2^\circ$
60		135°	135°
70		$157\ 1/2^\circ$	$157\ 1/2^\circ$
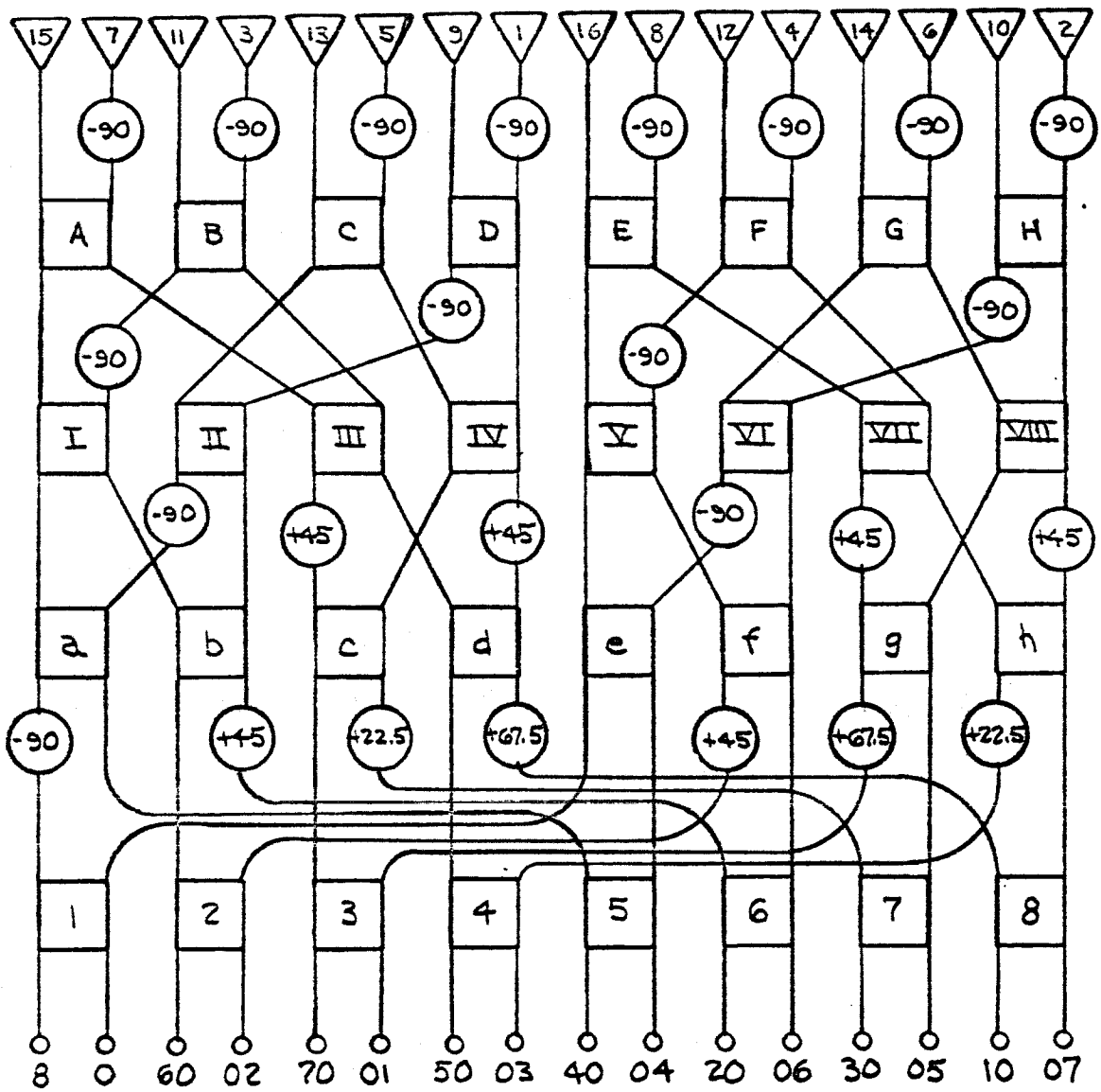
(MODE NO P)
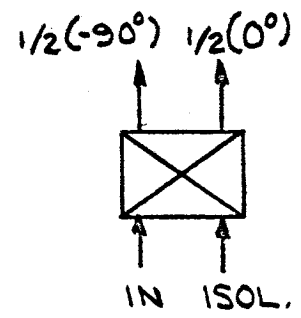
Figure 17. Schematic diagram of the sixteen-port matrix.

Port No.	Mode	Beam Direction (ϕ)	Inter-Element Phase Progression
8		$180°$	$180°$
07		$202\ 1/2°$	$202\ 1/2°$
06		$225°$	$225°$
05	Same as port no.	$247\ 1/2°$	$247\ 1/2°$
04		$270°$	$270°$
03		$292\ 1/2°$	$292\ 1/2°$
02		$315°$	$315°$
01		$337\ 1/2°$	$337\ 1/2°$

The first column of the above table defines the port number designation and corresponds to the terminology of Figure 17. These same port numbers are also used to indicate the multiple-beam positions. The port numbers are selected to identify the omnidirectional mode generated by the mode-forming matrix when it is attached to the sixteen-element array. Thus, the terminology of column 2 is identical to that of column 1. This terminology is in accordance with the convention described on page 25 of this report. The third column identifies the direction of a beam generated for the matrix which is used to generate the multiple beams. The fourth column identifies the inter-element phase progression.

The interconnections between the outputs of the vertical elevation banks and the mode matrix, along with the interconnections between the mode matrix and the multiple-beam matrix, are defined in the table below.

Matrix Terminal Connections

Element No.	1	2	-------------	16
	↕	↕	-------------	↕
Mode Network Antenna Terminals	1	2	-------------	16
	↕	↕		↕
Mode Network Input Terminals	0	10 ---70	8 07 ---	01
	↕	↕ ↕	↕ ↕	↕
Beam Network Output Terminals	0	9 ---15	16 1 ---	7

-54-
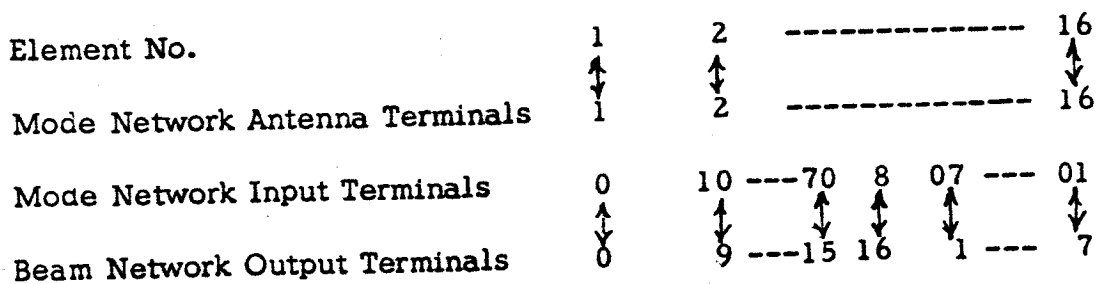
The terminology, defined in the above table, is in accordance with the terminology used in Figure 17. This same terminology was used to identify the terminals of the developed antenna system.

The sixteen-port matrix consists of 3 db couplers and fixed phase shifters. All of these components are designed in three-layer strip transmission line medium. The individual layers are 1/16-inch thick and the base dielectric medium is a copper-clad polyolefin (a radiated polyethylene material). The following paragraphs will now detail the performance of the couplers and the fixed phase shifters used in the matrix. Subsequent paragraphs will detail the performance recorded for the sixteen-port matrix component.

3.2.3.2.1 Three db Coupler Design

The strip transmission line 3 db tandem couplers are formed by utilizing two 8.3 db couplers in tandem[1]. This arrangement allows the spacing between the coupling sections to be 1/16-inch, a thickness consistent with commercially available thicknesses of the polyolefin base material. The characteristics of the developed coupler are listed below.

Frequency	1.7 kmc	2.3 kmc	1.7 – 2.3 kmc
Maximum Imbalance	±0.10 db	±0.10 db	±0.25 db
Maximum VSWR	1.10	1.05	1.14
Minimum Isolation	-22.5 db	-30.8 db	-22.5 db

The above data were taken with modified TNC type connectors at the input and output terminals. In the actual matrix, these terminals were removed and all interconnections between components were made with printed circuit transmission line
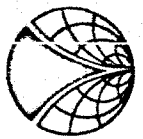
lengths.

3.2.3.2.2 Fixed Phase Shifters

Fixed phase shift values of 22.5, 45, 67.5, and 90 degrees are required to implement the sixteen-port matrix. These fixed phase shifts are relative to a fixed length of strip transmission line. Two types of differential fixed phase shifters are utilized: coplanar and biplanar. The distinction between these two types of phase shifters is best illustrated by reference to Figure 18. The coplanar phase shifter is photoetched on one side of the 1/16-inch center layer of polyolefin. The differential fixed phase shift, relative to the reference line length, is controlled by the coupling between the two short circuited lines. This coupling is, in turn, controlled by the gap width, g, and the line width, w. This type of phase shifter was used for the 22.5 and 45 degree phase shifters. It could not be utilized for the 67.5 or 90 degree phase shifters because the tighter coupling required gap widths which were impractically small. For these higher values of fixed phase shift, the biplanar type, shown in the lower half of Figure 18, were used. In this instance, the coupled sections are printed on the top and bottom surfaces of the 1/16-inch center layer of polyolefin. The coupling is controlled by the width, w, and the thickness of the polyolefin board. It is also controlled by the length of the coupling region.

The input impedance, for both phase shifter types, is 50 ohms. Both of these phase shift types are designed in accordance with the initial theory

CENTRAL LAYER OF POLYOLEFIN

COPLANAR
$Z_0 = 50\ \Omega$

$\frac{1''}{16}$ POLYOLEFIN CENTER LAYER

SHORT CIRCUIT

TOP VIEW   SIDE VIEW
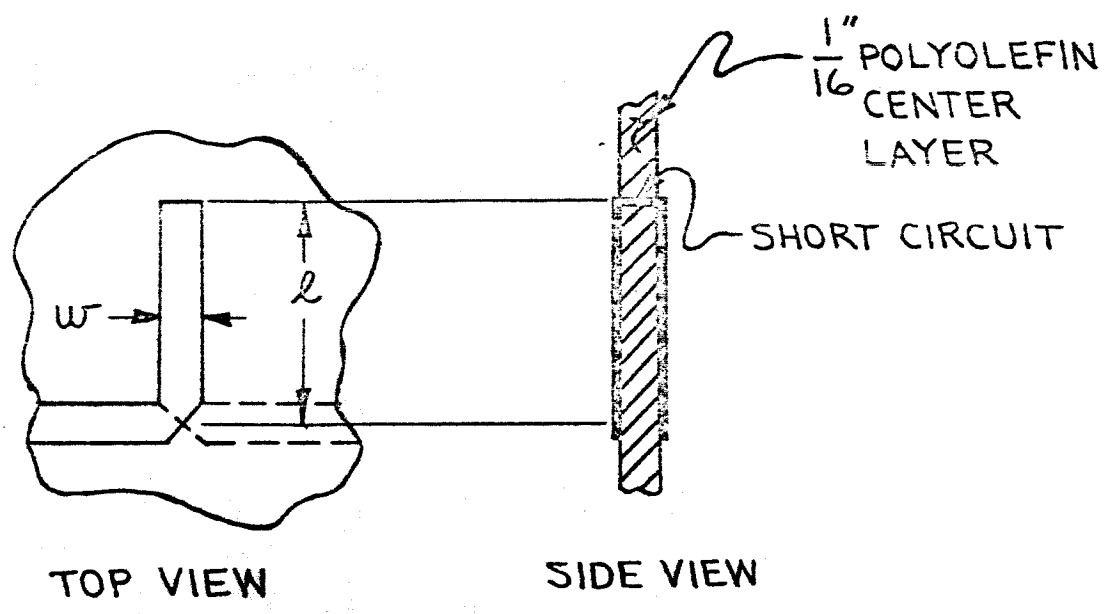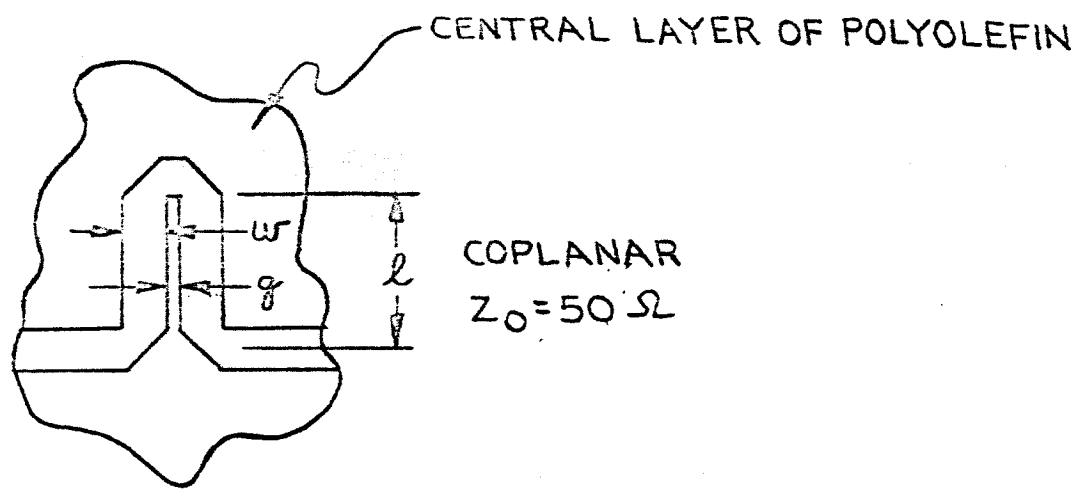
BIPLANAR
$Z_0 = 50\ \Omega$

Figure 18.   Biplanar and coplanar phase shift sections.

described in the literature by Schiffman[11]. The performance characteristics

of the developed phase shifters are listed in the following table:

+22 1/2° Fixed Phase Shifter[1] (Coplanar Type)

	1.7 kmc	2.27 kmc	1.7 — 2.3 kmc
Frequency			
Measured phase shift	+22.2°	+22.5°	
Greatest phase deviation	—	—	+21.3° — 22.8°
Maximum VSWR	1.13	1.21	1.22

+45° Fixed Phase Shifter (Coplanar Type)

	1.7 kmc	2.27 kmc	1.7 — 2.3 kmc
Frequency			
Measured phase shift	+44.8°	+45.2°	
Greatest phase deviation	—	—	+44.8° — +45.8°
Maximum VSWR	1.19	1.13	1.19

+67 1/2° Fixed Phase Shifter (Biplanar Type)

	1.7 kmc	2.27 kmc	1.7 — 2.3 kmc
Frequency			
Measured phase shift	+68.2°	+66.7°	
Greatest phase deviation	—	—	+66.7 — 70°
Maximum VSWR	1.09	1.15	1.18

+90° Fixed Phase Shifter (Biplanar Type)

	1.7 kmc	2.27 kmc	1.7 — 2.3 kmc
Frequency			
Measured phase shift	+91.2°	+88.8°	
Greatest phase deviation	—	—	+88.8° — +93°
Maximum VSWR	1.11	1.17	1.18

Note 1) - Phase is that of coupled section relative to that of straight line
reference section.

All of the above data were obtained with TNC type input and output connections.

3.2.3.2.3 Performance of the Sixteen-Port Matrix

The sixteen-port matrix is formed in three layers of 1/16-inch thick polyolefin. All of the printing is contained in photo-registry on the center 1/16-inch thick layer. The above defined components are integrated on this central layer in such a manner that no component-to-component coaxial connections are required. The entire package is contained within an 18-inch cylinder, having a total depth of 5/16-inch, including a top and a bottom 1/16-inch thick aluminum support sheet. The performance of the sixteen-port matrix is summarized below.

Frequency	1.7 kmc	2.27 kmc
Greatest measured amplitude imbalance	± 0.8 db	± 1.0 db
Average amplitude imbalance	± 0.3 db	± 0.5 db
Greatest measured phase deviation	$\pm 2.2^{\circ}$	$\pm 2.9^{\circ}$
Average phase deviation	$\pm 1.1^{\circ}$	$\pm 1.4^{\circ}$
Poorest measured isolation	19.0 db	15.0 db
Average isolation	24 db	22 db
Worst measured VSWR	1.29	1.38
Average VSWR	1.19	1.18
Average insertion loss	0.8 db	1.2 db

All of the above data were taken using the final TNC input and output connections. Two sixteen-port matrices were formed from the same master negative: one for the mode forming network and one for the beam forming network. The

terminology used on the ports of the final matrices is that defined in the early paragraphs under Section 3.2.3.2. The performance of the matrices was considered acceptable for implementation in the cylindrical array portion of the developed antenna system.

3.2.3.3 Four-Port Matrices

A total of sixteen four-port matrices are required to implement the cylindrical array. Each of these matrices is used to combine the four vertically arrayed elements which occur at each of sixteen different azimuth stations. The function of the matrix is to generate four simultaneous beams displaced in elevation and at a constant azimuth station.

The block diagram of the four-port matrix is shown in Figure 19. It consists of four couplers and a series of fixed phase shifters. Solid-state two-step phase shifters are also utilized in each of the output ports. This network, when excited at any of its inputs, provides an equi-amplitude distribution at the output ports. The output port phase distribution for each of the input ports, is defined in the table on the following page.

ANTENNA PORTS

$$\frac{E_{IN}}{\sqrt{2}} \angle 0° \qquad \frac{E_{IN}}{\sqrt{2}} \angle 90°$$

3db
HYBRID
COUPLER

E_{IN} ISOLATED

⬭ FIXED PHASE SHIFTERS

▢ LINE LENGTHS

◇ 2-STEP PHASE SHIFTERS
ALL 0° BACK BIAS.
VALUES SHOWN
FORWARD BIAS.

INPUTS FROM 4-WAY SWITCH
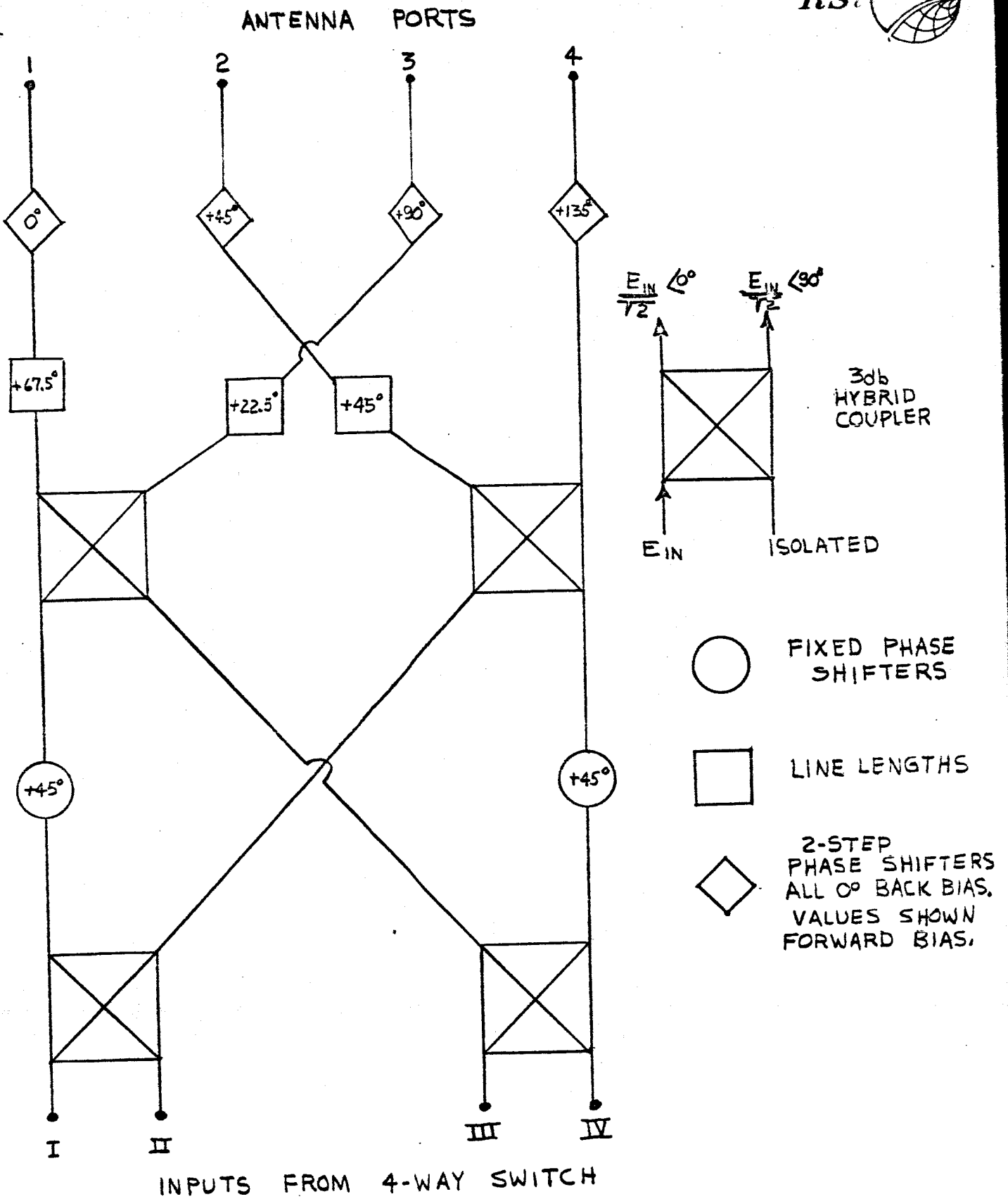
Figure 19. Four-port matrix with solid-state two-step phase shifters
(interpositioning)

Beam Port	Interport Phase	Beam Position ($\theta - 90°$)		
		1.7 kmc	2.27 kmc	Nominal
	Case I			
I	$-22.5°$	$-7.1°$	$-5.3°$	$-6°$
II	$+157.5°$	$+60°$	$+50°$	$+40°$
III	$-112.5°$	$-38°$	$-27.5°$	$-28°$
IV	$+67.5°$	$+21.8°$	$+16°$	$+16°$
	Case II			
I	$+22.5°$	$+7.1°$	$+5.3°$	$+6°$
II	$-157.5°$	$-60°$	$-50°$	$-40°$
III	$+112.5°$	$+38°$	$+27.5°$	$+28°$
IV	$-67.5°$	$-21.8°$	$-16°$	$-16°$

Case I is for the instance where the solid-state phase shifters are in their back bias condition. The phase shift in each of the output phase shift blocks is $0°$. For Case II the solid-state phase shifters are in their forward bias condition. The phase shifts in each of the output blocks, for this instance, are as shown in the sketch of Figure 19. The above table, in addition to defining the output phases, also defines the beam position for both Cases I and II and for frequencies of 1.7 and 2.27 kmc. These beam positions are relative to the horizon station ($\theta = 90°$) rather than to the zenith reference.
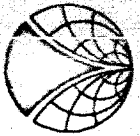
They were derived using conventional array theory, the above listed inter-port phase progressions, and an antenna element spacing of 3.5 inches. The nominal beam positions, as listed on the remote control beam position network, are also defined in the above table. It is interesting to note that the nominal beam position is closer to the horizon than the average beam position for both frequencies. This occurs because of the element pattern shape which tends to move the beam maxima closer to the horizon position.

The object of using two separate sets of four beam positions is to avoid the normal beam crossover gain loss. The above listed beam positions are so arranged that the beam maxima for Case I lie at the beam crossover points for Case II, and vice versa. The four-port matrices were originally designed for both Cases I and II. However, for economic reasons, it became impractical to include the diodes for achieving the Case II excitations. Consequently the sixteen four-port matrices have metal blanks inserted in place of the diodes such that only the Case I excitations can be achieved. A separate fully implemented vertical array was fabricated, however, and will be discussed later in the report.

The required sixteen four-port matrices are fabricated in three-layer strip transmission line. These networks use the components described in Section 3.2.3.2. The networks are 3.0 inches wide by 14.1 inches long. The depth of the networks is 5/16-inch, including a top and a bottom 1/16-inch thick aluminum sheet. The average performance achieved with these

four-port networks is listed below.

Frequency	1.7 kmc	2.27 kmc
Greatest measured amplitude imbalance	± 0.3 db	± 0.4 db
Average amplitude imbalance	± 0.3 db	± 0.3 db
Greatest measured phase deviation	± 6.5°	± 10.5°
Average phase deviation	± 4.9°	± 8.6°
Poorest measured isolation	22.3 db	23.0 db
Average isolation	23.8 db	25.5 db
Worst measured VSWR	1.35	1.52
Average VSWR	1.23	1.42
Average insertion loss	0.3 db	0.60 db

The above data were obtained with TNC input and output connectors. When these units were implemented in the array, the input and output connectors were removed so that an integrated package could be formed. This package consisted of the antenna elements, the four-port matrix, and the SP4T solid-state switch.

Specially designed coaxial connectors were utilized to allow this integration to be realized.

3.2.3.4 R-F Cabling

Two sets of 16 r-f cables were required for the implementation of the cylindrical array. One set was used to connect the outputs of the mode

forming matrix to each of the sixteen vertical banks. A second set of cables was required to interconnect the mode-forming and beam-forming matrices. The cables from the mode-forming network to the vertical bank input were formed of RG-141/U teflon impregnated coaxial cable. TNC connectors were utilized at each end of the cable. The average loss of these cables at 1.7 gc was 0.3 db. The average loss at 2.27 gc was 0.4 db. Cables from mode network port numbers 1, 3, 5, 7, 9, 11, 13 and 15 had interconnecting lengths of 17.00 inches. Cables connected to the remaining ports had interconnecting lengths of 13.95 inches. The cable lengths were measured from connector-end-to-connector-end. The reason for the disparity in lengths is that one of the sets of cables includes a 3/4 wavelength additional length to compensate for the phase shift sections contained in each of the alternate output terminals of the matrix. This allowed the sixteen-port matrices to be packaged within the 18-inch diameter, a feat which would not have been possible without using two different sets of cabling.

The cables connecting the mode-forming and beam-forming matrices were first determined theoretically and then modified experimentally to achieve the best overall system performance. These cable lengths also had an average insertion loss of 0.3 db at 1.7 gc with an average insertion loss of 0.4 db at 2.27 gc. The lengths of the cables, using the same connector-end-to-connector-end measurement, are listed in the table on the following page.

Beam Matrix Port Number	Mode Matrix Port Number	Cable Length
1	07	14. 0"
2	06	12 1/8"
3	05	16 1/8"
4	04	15 3/8"
5	03	15 1/2"
6	02	14 12/32"
7	01	15 3/16"
8	0	14 13/16"
9	10	13 1/4"
10	20	12 3/8"
11	30	12 1/2"
12	40	13. 0"
13	50	13 5/16"
14	60	12 3/8"
15	70	13 15/16"
16	8	13 1/2"

The terminology used in the above table is identical to the terminology used in Section 3. 2. 3. 2.

3. 2. 3. 5 Solid-State SP4T Switches

A solid-state SP4T switch is required to reduce the four beam outputs of each of the sixteen multiple-beam vertical arrays to a single terminal. The block diagram of this switch is defined in the sketch of Figure 20. It consists of three DPDT solid-state transfer switches arranged to form a conventional switching "tree". One of these switches has additional alphabetical port terminology to assist in describing the theory of the DPDT transfer switch operation. When the solid-state switches are back biased, input, a, is connected to port, c, (or I) and port, d, (or II) is connected to port, b. In the forward bias case port, a,

VERTICAL ARRAY
PORT NUMBERS

DPDT SOLID STATE
TRANSFER SWITCH

INPUT/OUTPUT

TO 16 PORT MODE
FORMING MATRIX

a) SP4T SWITCH

3db COUPLER
DC BIAS
DC BLOCK
3 db COUPLER
1N270 DIODES
MYLAR SHIM
INPUT
DC GROUND
DC BIAS INPUT
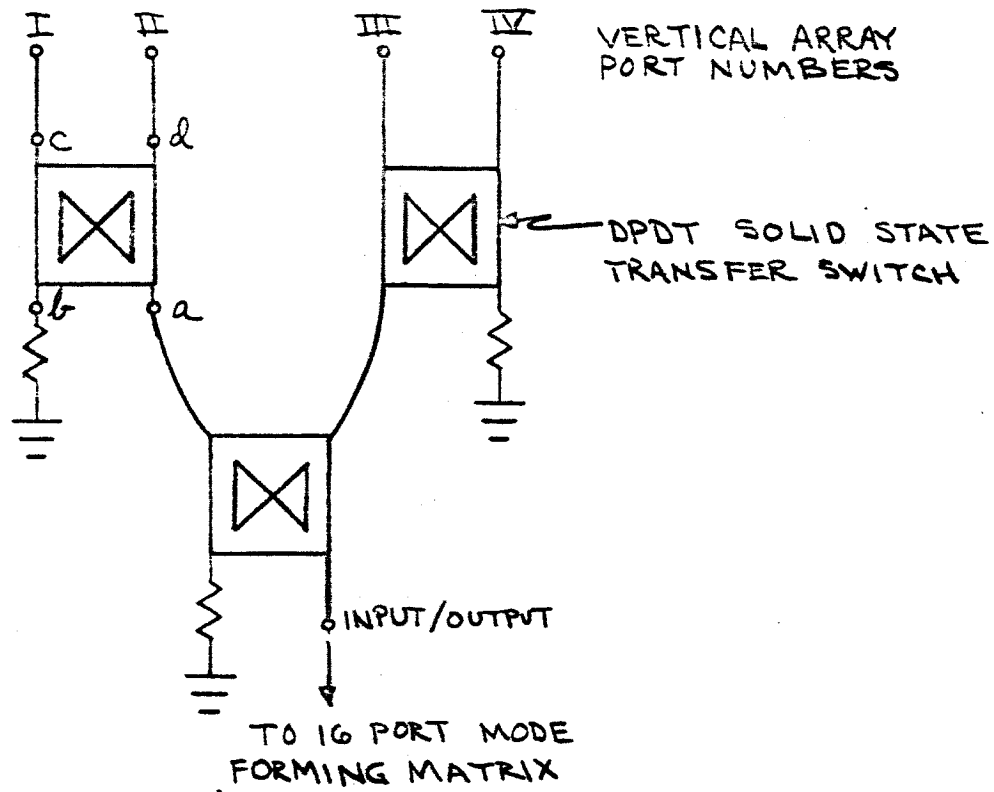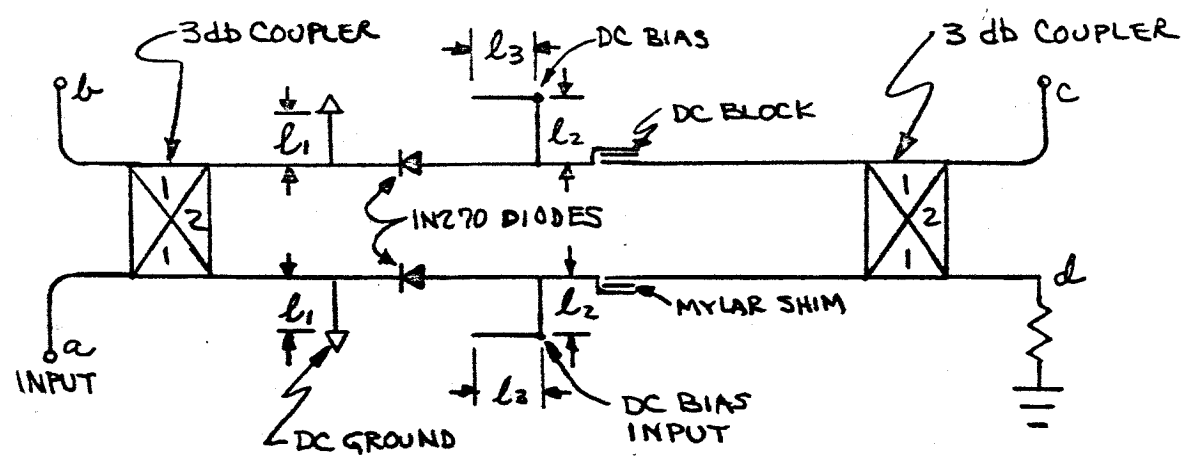
b) SPDT TRANSFER SWITCH

Figure 20.   The SP4T switch and the SPDT transfer switch.
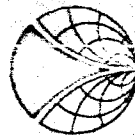
connects to port, d, and port, c, connected to port, b. Thus the unused port is always terminated in a matched load. This is important in a multiple-beam array! If the unused ports are not terminated, reflections from the antenna terminals will appear at, and be reflected by, these open circuited ports. The resultant energy then reradiates and forms a collimated beam just as though the unused beam port were excited by an. amount of r-f energy equal to the magnitude of the reflected energy. The resultant spurious beam thus appears in the far-field pattern as undesired sidelobe content.

The developed SPDT solid-state transfer switch is sketched in the lower half of Figure 20. It consists of two couplers interconnected by two transmission lines, each containing a diode in series. In the reverse bias case the diodes are open circuited and the r-f energy is reflected back through the input hybrid and appears at port, b. In the forward bias case the diodes are conductive and the energy from input, a, passes through the second coupler to port, c. Port d is terminated by a 50 ohm "tab" [1] load.

The DC ground is a short circuited stub of length ℓ_1. This length is approximately one-quarter-wavelength long at 2.0 kmc. Thus, it effectively appears as an open circuit to the main line containing the series connected diode. The DC bias input is located a distance, ℓ_2, from the main line. It is short circuited at r-f frequencies by an open circuited stub of

length, ℓ_3. This length is also approximately $\lambda/4$ at 2 kmc. The length, ℓ_2, was selected to minimize r-f discontinuities but it too was also approximately $\lambda/4$ long at 2 kmc. The DC block consists of two overlapping sections in the main line. The two halves of the line are separated by a 3 mil mylar shim. The overlap area is sufficiently large to have a high capacitance with a resultant low r-f series impedance.

The switch is formed in three layers of 1/16-inch thick each polyolefin with the central layer containing the r-f circuitry. The 3 db couplers are identical to those described in Section 3.2.3.2. The solid-state devices are 1N270 diodes. The performance of this individual switch is described below.

Frequency:	1.7 kmc	2.27 kmc
VSWR (forward bias)	1.29	1.34
VSWR (reverse bias)	1.08	1.05
Isolation (forward bias)	11.5 db	22.1 db
Isolation (reverse bias)	22.2 db	21.3 db
Loss (forward bias)	0.5 db	0.8 db
Loss (reverse bias)	0.4 db	0.7 db

Current drain: 100 miles at 6.3 volts in forward bias (50 miles/diode)

Back bias: −30 V DC

The above described SPDT switches were integrated into a single 14.1 x 3.0 x 5/16-inch three-layer strip transmission line package. The output port positions were made to exactly coincide with the input ports of the four-port matrix. Specially designed coaxial connectors were fabricated

to allow direct connection of the switch to the four-port matrix without the need for commercial coaxial adaptors. The average measured performance of this SP4T switch is described below.

Frequency	1.7 kmc	2.27 kmc
Maximum VSWR	1.31	1.80
Average VSWR	1.17	1.67
Minimum Isolation	12.8 db	14.5 db
Average Isolation	24.1 db	23.2 db
Maximum Insertion Loss	1.0 db	1.6 db
Average Insertion Loss	0.85 db	1.4 db

The above data were obtained with temporary TNC input and output co nectors which were removed prior to integration.

3.2.3.6 Sixteen-Port Switching Network

A solid-state single-pole sixteen-throw switch is required to reduce the 16 azimuth station beam outputs of the beam-forming matrix to a single terminal. The block diagram of this switch is defined in the sketch of Figure 21. It consist of 15 DPDT solid-state transfer switches arranged to form a conventional switching "tree". The terminology and functioning of these switches are identical to that which was described for the SP4T switch of Figure 21. The SP16T switch also has the feature that all unused ports are terminated.
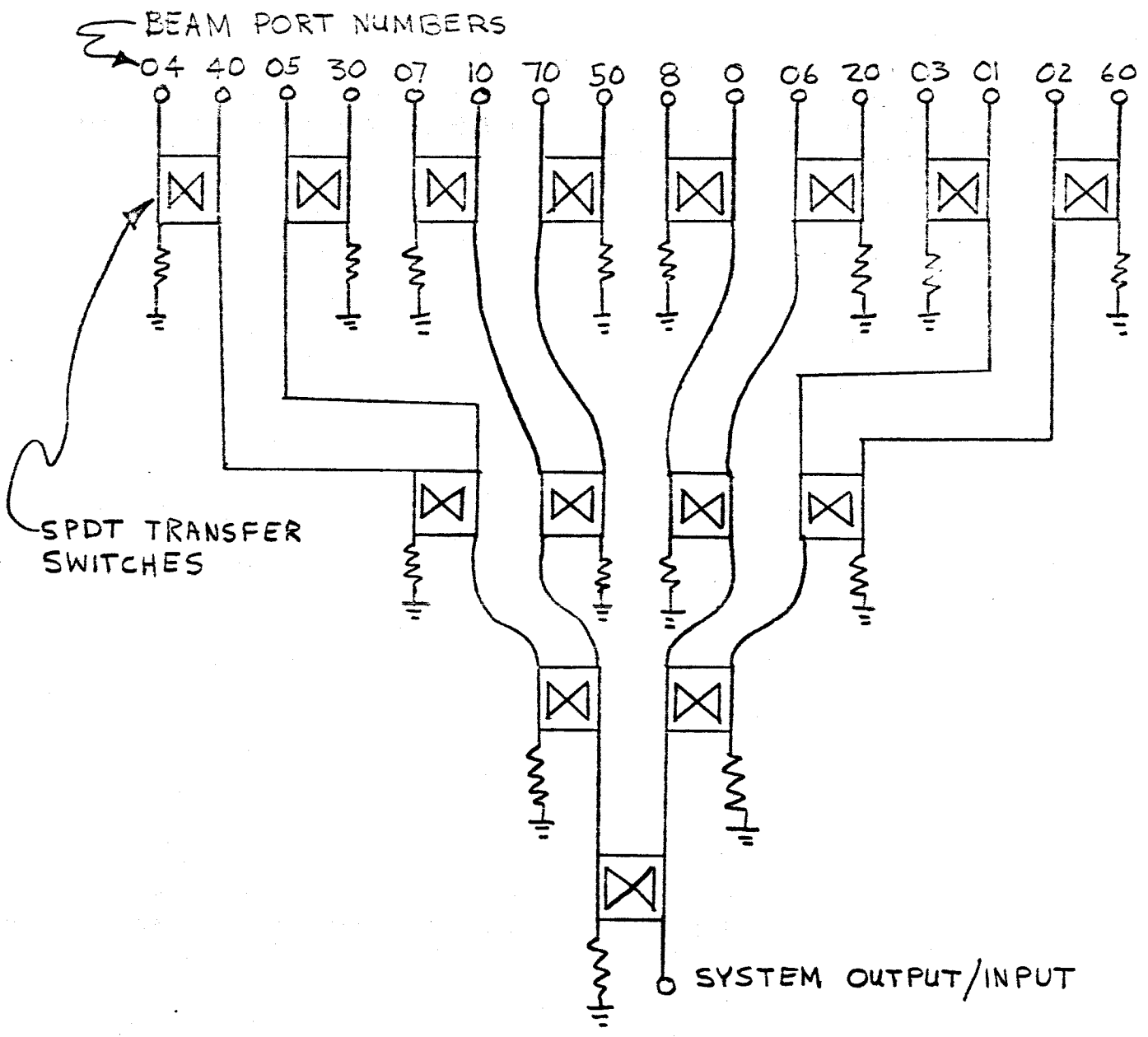
Figure 21.   Schematic of sixteen-element switching tree.

The major difference between the network of Figure 21 and the SP4T network, outside of the number of ports, is in the detailed makeup of the SPDT transfer switch. The SPDT transfer switch used in the sixteen-port matrix is designed to handle high average input powers. This switch is sketched on Figure 22. It consists of two couplers interconnected by two transmission lines, each shunted by a diode. In the reverse bias case, the diodes are open circuited and the r-f energy is allowed to pass through from the first input coupler to the output of the second coupler. In the forward bias case, the diodes are conductive and hence short circuit the main feeder lines between the couplers. The r-f energy in this case is reflected and appears at the normally isolated port of the first input coupler. The unused port of the coupler is terminated by a 50 ohm tab load. The DC ground is connected in shunt to the main feeder lines. This DC short circuit is located approximately one-quarter wavelength (at 1700 mc) from the main feeder line. A corrective 2270 mc tuning stub, which is an approximate one-quarter wavelength open circuit at 2270 mc, is located at an intermediate port between the ground connection and the main feeder line. The bias input is shorted at the r-f frequencies by two tuning stubs: one a quarter-wavelength long, at 2270 mc, and the other a quarter-wavelength long at 1700 mc. The length between these stubs and the diode is controlled to correct for diode junction reactances and to achieve the best overall switch performance.

The switch is formed in three layers of 1/16-inch thick polyolefin

BIAS INPUT

RF OUT (FORWARD BIAS)

3 RF OUT (BACK BIAS)

BIAS RETURN (GROUND)

1
2
1

2270 MC TUNING STUB BACK BIAS

1
2
1

RF INPUT

50 Ω

FORWARD BIAS 2270 MC TUNING STUB

FORWARD BIAS 1700 MC TUNING STUB

BIAS INPUT
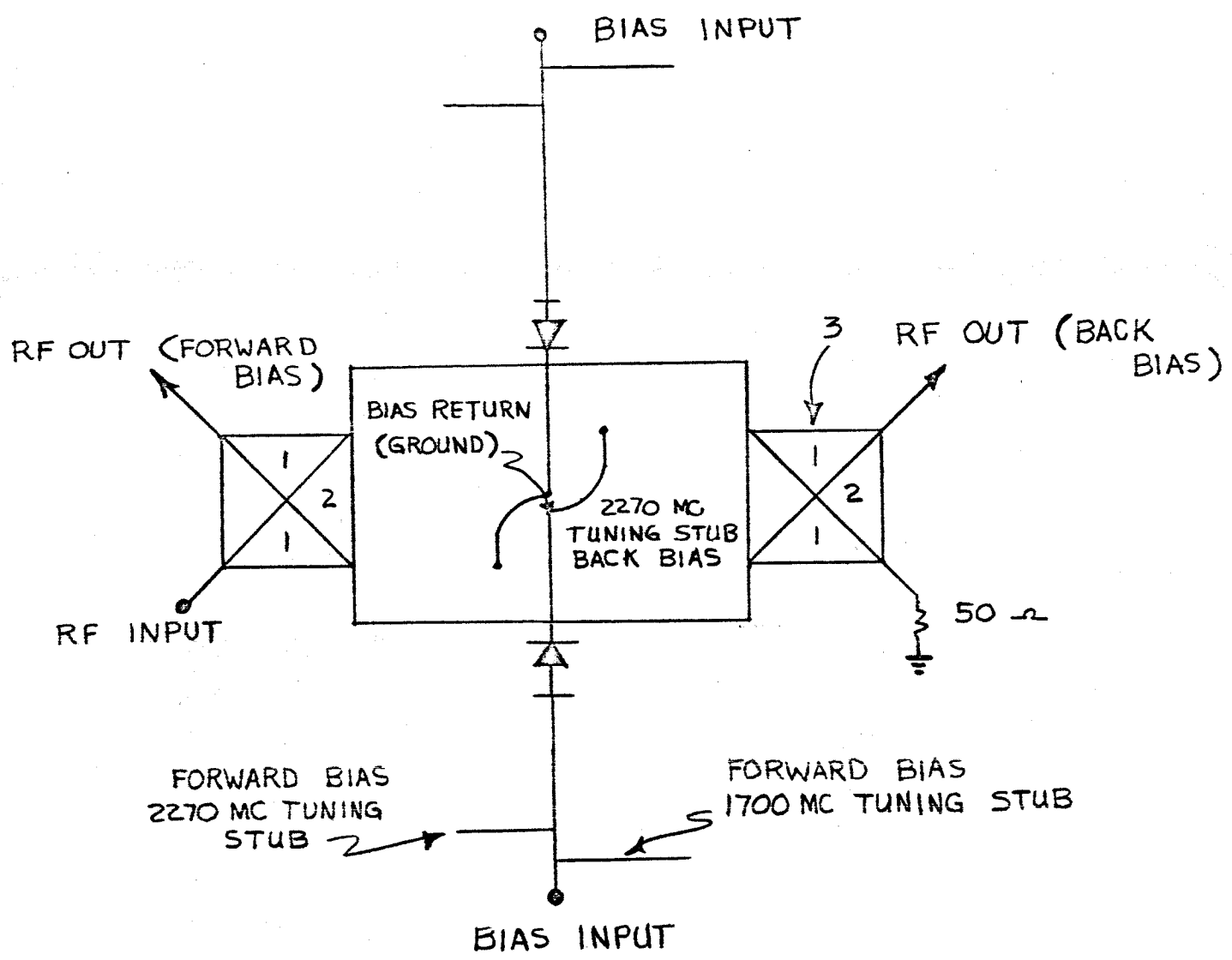
All STUBS ARE OPEN CIRCUITED AT ENDS.

Figure 22.   SPDT high power switch.

with the central layer containing the r-f circuitry. The 3 db couplers are identical to those described in Section 3.2.3.2. The solid-state devices are MA-4571C1 diodes and require individual forward current drains of 50 mils at +6.3 VDC. The back bias voltage for the diode is -30 VDC. The performance of the individual SPDT switch is described below.

Frequency	1.7 kmc	2.27 kmc.
Maximum VSWR	1.06	1.26
Average VSWR	1.04	1.20
Minimum Isolation	15.5 db	26.8 db
Average Isolation	24.8 db	30.1 db
Maximum Insertion Loss	0.7 db	0.4 db
Average Insertion Loss	0.6 db	0.2 db

The SPDT switch was successfully subjected to 20 watts of average r-f power at 1700 mc and 2270 mc. The peak power rating could not be determined because the necessary equipment was not available. However, it is felt that the peak power capacity would be in excess of 1.2 kw. The above data were taken with TNC input and output connectors. One SPDT switch was delivered to NASA. The remainder of the developed switches were used in the sixteen-port switch and hence were without connectors, except at the input and output terminals of the sixteen-port network. The SPDT switches were integrated into two 18-inch diameter x 5/16-inch thick three-layer strip transmission line packages formed of

the polyolefin base material. The output port positions were made to exactly coincide with the input ports of the four-port matrix. The input and output connectors on the switching network were of the TNC variety. Connections between the beam matrix and the sixteen-port switching network were made with commercial TNC type feed-throughs. The average measured performance of this SP16T switch is defined below.

Frequency	1.7 kmc	2.27 kmc
Maximum VSWR	1.20	1.40
Average VSWR	1.18	1.37
Minimum Isolation	15.0 db	26.1 db
Average Isolation	21.8 db	28.9 db
Maximum Insertion Loss	2.8 db	2.5 db
Average Insertion Loss	2.4 db	2.1 db

3.3 Twelve-Element Planar Array

The objective of this section of the report will be to describe the theory of operation, the detailed design and the network component design for the twelve-element planar array. This array, as described in the schematic of Figure 3, consists of twelve antenna elements, a twelve-port multiple-beam network, and a SP12T switching network.

3.3.1 Theory of Operation

The twelve-element planar array is unique in that it does not use the conventional square building block of the more common multiple-beam

antenna systems. The array building block for the twelve-element array is a three-element equi-lateral grid. This arrangement allows improved crossover levels to be achieved, while at the same time allowing a reduction in sidelobe levels relative to those obtainable from a conventional square array having the same distribution.

The geometry of the twelve-element multiple-beam array is sketched in Figure 23. Examination of this figure will indicate that it consists of equi-lateral grids with an element spacing equal to, a. The relative voltage array factor, in any plane containing a row of elements, may be derived as being equal to

$$E_p \ (\psi_p) = \left[\cos \ (\psi/4) \right] \ \frac{\sin \ (3\psi/2)}{\sin \ (\psi/4)} \tag{15}$$

where: $\quad \psi_p \quad = \ k \ a_p \ \sin \theta$

$\qquad\quad a_p \quad = \ a/2$

$\qquad\quad a \quad = \ \text{grid spacing (see Figure 23)}$

$\qquad\quad k \quad = \ 2\pi/\lambda$

$\qquad\quad \theta \quad = \ \text{angle relative to broadside}$

$\qquad\quad \lambda \quad = \ \text{wavelength.}$

The relative voltage array factor for the planes between the rows of elements (see Figure 23) may be written as

$$E_m \ (\psi_m) = \ 5 \cos \ (3\psi_m/2) + 7 \cos \ (\psi_m/2) + j \ 4 \sin(\psi_m/2)$$
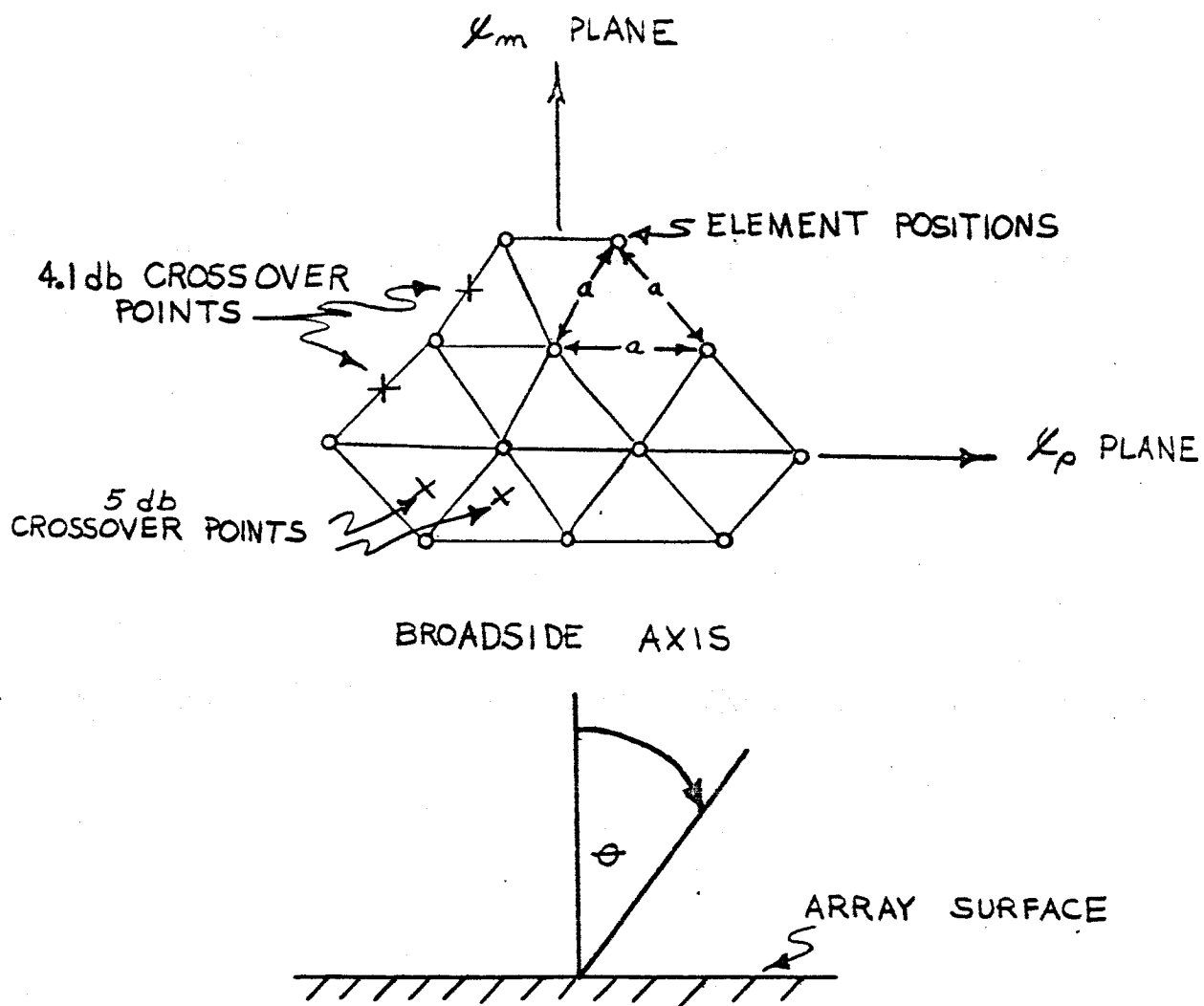$$\cos^2 \ (\psi_m/2) \tag{16}$$

Figure 23. Geometry of the twelve-element array.

where: $\psi_m = k\, a_m \sin\theta$

$a_m = 0.866\, a$

The array factors derived from equations (15) and (16) are plotted in the sketch of Figure 24. The highest sidelobe is -15.6 db. This sidelobe level may be compared to that of a sixteen-element square array which has a sidelobe level of -11.4 db.

If a multiple-beam twelve-port martix is utilized, the proper phasors are added in the array factor to generate a cluster of twelve beams. The actual angular location of the patterns can be determined by projecting the ψ— plane patterns on the surface of a sphere. The beam cluster of twelve beams will thus duplicate the element arrangement of the array. The crossover levels can be computed as ranging from -4.1 db between any two adjacent elements, and to -5.0 db at a common crossover of any three elements. By way of comparison, a sixteen-element square array has crossover levels ranging from -3.7 db between any two elements, and to -7.4 db at any crossover common to four elements.

3.3.2 Detailed Design

A sketch of the top surface arrangement of the twelve-element planar array is shown in Figure 25. This actual array geometry duplicates the geometry first listed in Figure 23. The individual elements are round spiral antennas driven against a metallic enclosed cavity. The center-to-
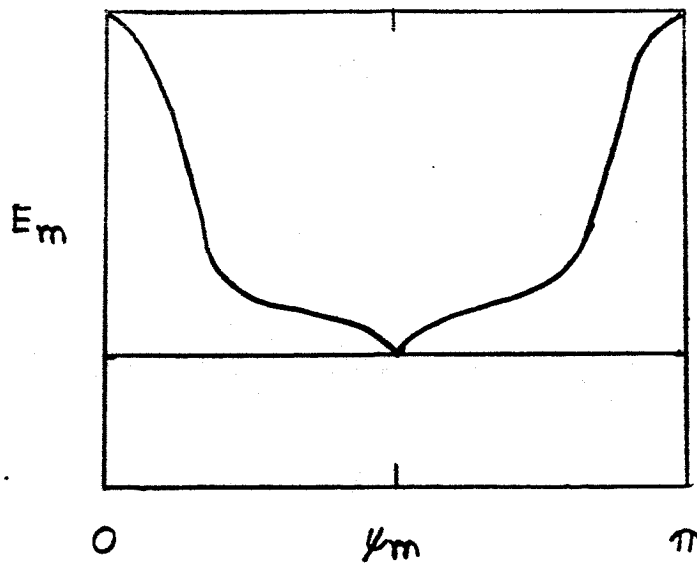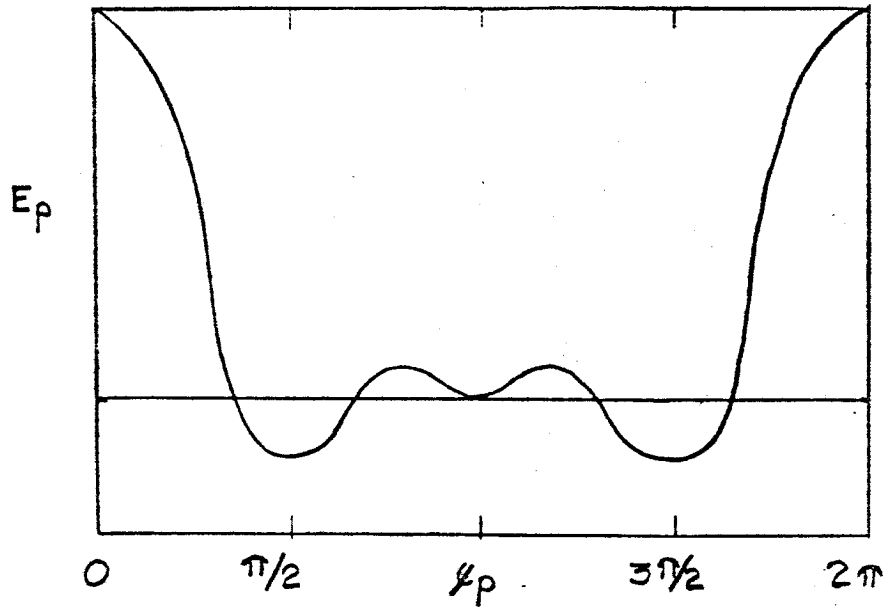
Figure 24. Array factors for the twelve-element array.

12 ELEMENT PLANAR ARRAY

18" DIA.
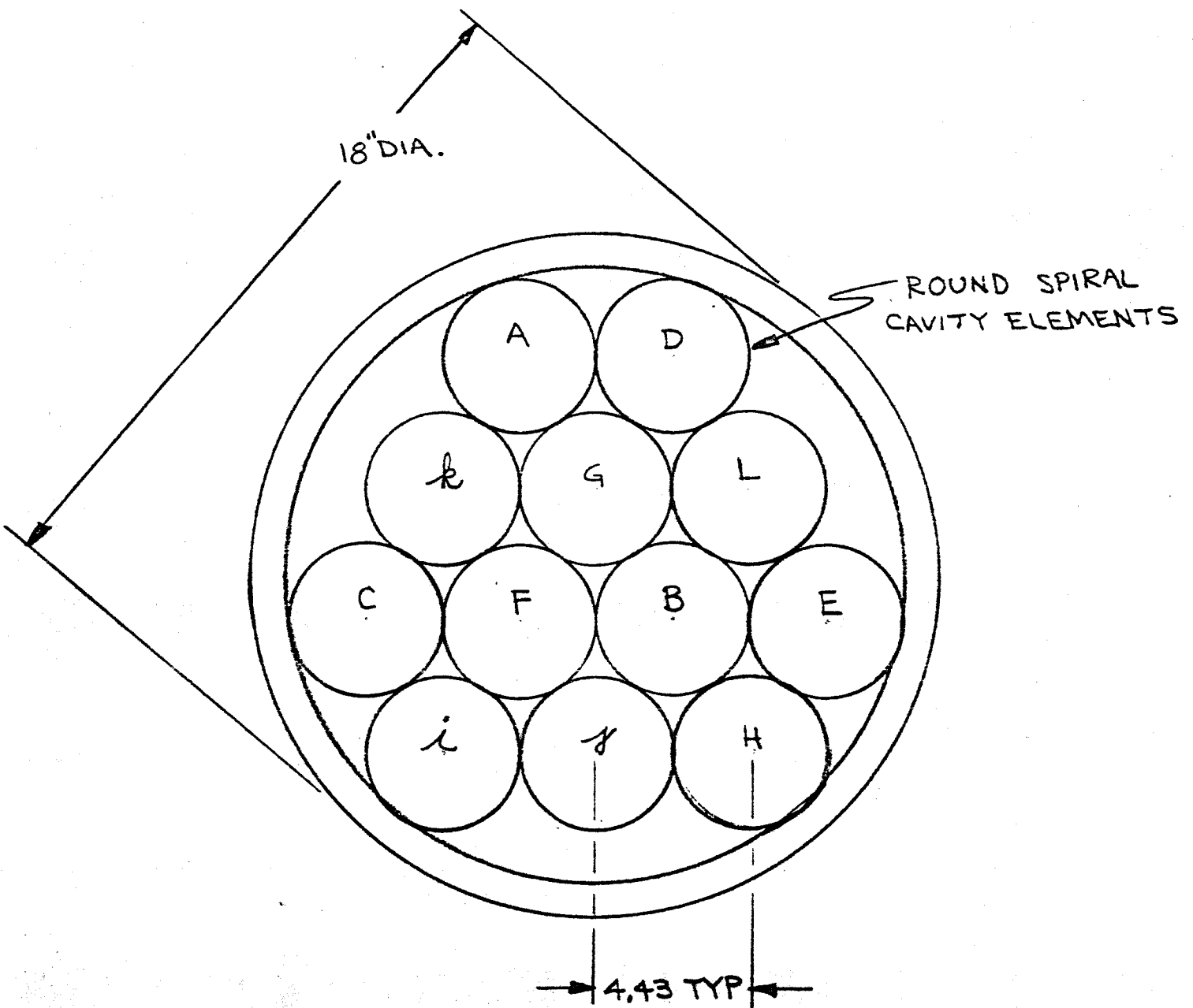
ROUND SPIRAL
CAVITY ELEMENTS

4.43 TYP

Figure 25. Geometry of the actual twelve-element array.

center spacing of these spiral elements (a) is equal to 4.33 inches. The entire array is contained within an 18-inch circle. The element notation utilized in this array corresponds to the matrix connection notation and will be used as reference throughout the remainder of the report.

The element spacing was used in conjunction with the matrix phase excitations and the array theory developed in Section 3.3.1 to compute the beamwidths and beam positions at 2270 mc. The computed patterns are too numerous to include in detail in this report, however, the salient characteristics of the patterns are listed below.

Beam Position Number	Major BW	Minor BW	Location θ/ϕ
1	21°	16.6°	$12^{\circ}/120^{\circ}$
2	21.8°	21.8°	$35.5^{\circ}/20^{\circ}$
3	21.5°	21.0°	$35.5^{\circ}/138.5^{\circ}$
4	22.7°	16.6°	$25^{\circ}/300^{\circ}$
5	20.9°	16.6°	$12^{\circ}/0^{\circ}$
6	21.5°	21.5°	$35.5^{\circ}/259^{\circ}$
7	21.5°	21.5°	$35.5^{\circ}/101^{\circ}$
8	22.7°	16.6°	$25^{\circ}/180^{\circ}$
9	21.0°	16.6°	$12^{\circ}/240^{\circ}$
10	21.8°	21.8°	$35.5^{\circ}/340^{\circ}$
11	21.5°	21.0°	$35.5^{\circ}/221.5^{\circ}$
12	22.7°	16.6°	$25^{\circ}/60^{\circ}$

The sidelobe levels recorded were generally in accordance with the sidelobes denoted by array theory. However, gradient lobes were encountered for the outermost beam positions. Although the computed patterns were not obtained for 1700 mc, it can be presumed that the beamwidths and beam positions would both alter in conventional accordance with the decreased element spacing (expressed in wavelengths). The actual noted beam positions measured

with the experimental twelve-element array will be listed in Section 4.0.

3.3.3 Network Components

The objective of this part of the report is to describe the design and performance characteristics of the major components which form the twelve-element planar array portion of the antenna system. The major components which will be discussed are listed below.

a) Spiral antenna elements

b) Twelve-port beam-forming matrix

c) Twelve-port switching network

The above components will be discussed in the following subsection of the report.

3.3.3.1 Antenna Element

A total of twelve spiral cavity antenna elements are utilized to implement the planar array portion of the developed antenna system. These spiral cavity elements are based on a design described in the literature by Bawer and Wolfe[10]. The cavity surface is circular in cross-section with a diameter of 3.5 inches. The spiral surface is housed in a cylindrical cavity having a depth of 1.360 inches. The performance characteristics of a typical spiral cavity element are listed below.

Frequency range	1.7 to 2.3 kmc
Average 3 db BW	75°
Average 10 db BW	140°
Maximum Axial Ratio	2 db maximum
Maximum VSWR	1.43

The above data were obtained with TNC connectors, modified to adapt to the balun which excites the spiral surface. The TNC connectors were subsequently removed and replaced by a female center pin and a specially developed outer coaxial housing. This latter arrangement allowed the twelve spirals of the planar array to be made an integral part of the exciting twelve-port multiple-beam matrix.

3.3.3.2 Twelve-Port Matrix

Reference to Figure 3 will indicate that a twelve-port beam-forming matrix is required to implement the multiple-beam planar array. For any given matrix input, all of the output element terminals are excited with equal amplitudes. However, the phase sequence from port-to-port varies as the input port is changed from one position to another. The block diagram of the beam-forming matrix is shown in the schematic of Figure 26. The antenna port terminology corresponds to that defined in Section 3.3.2. The input port terminology corresponds to the beam position number in space. This terminology was also defined in Section 3.3.2. The same sets of terminal designations were used in the actual antenna system.

The twelve-port matrix consists of 3 db couplers, 4.7 db couplers, and fixed phase shifters. All of the components for the network are designed in three-layer strip transmission line. The individual layers are 1/16-inch thick and the base dielectric medium is polyolefin. Many of the components utilized in the twelve-port matrix were described earlier as part of the discussion for the sixteen-port matrices. Only those components which have
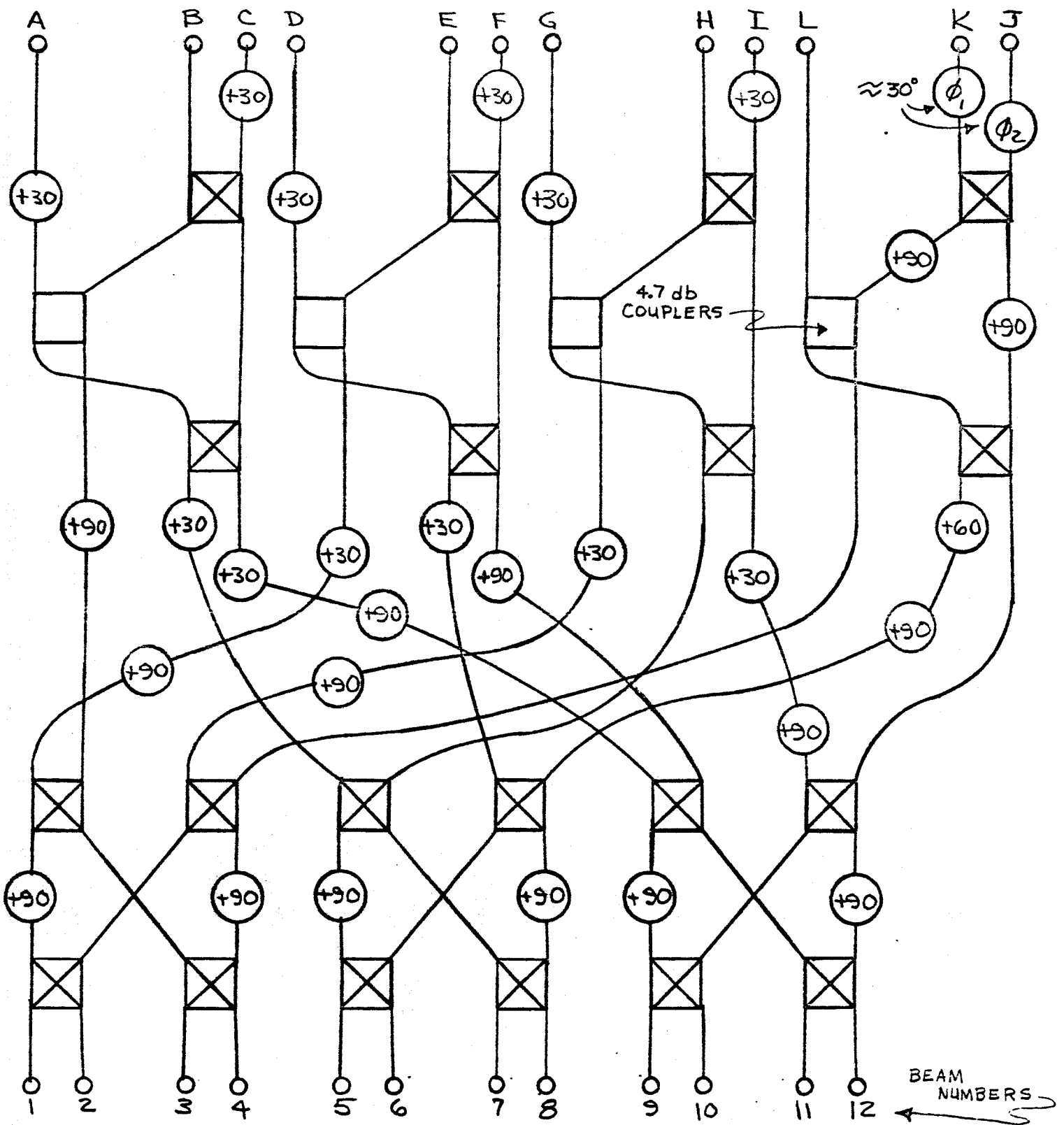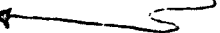
FIGURE 26   12 PORT MATRIX

not been previously described will be discussed below.

3.3.3.2.1 4.7 db Coupler Design

The 4.7 db coupler design was patterned after that earlier described for the 3 db coupler. It is of the tandem variety with the basic difference being the change in coupling between the two quarter-wavelength sections which form the tandem device. The spacing between coupling sections is thus again equal to 1/16-inch. The characteristics of the developed coupler are listed below.

Frequency	1.7 kmc	2.27 kmc	1.7 — 2.3 kmc
Coupled port level	-4.9 db	-4.8 db	$-4.7 \begin{array}{l} +0.0 \text{ db} \\ -0.3 \text{ db} \end{array}$
Isolation	24.0 db	25.5 db	24.0 db
Maximum VSWR	1.18	1.18	1.18

The above data were taken with modified TNC connectors at the input and output terminals. In the actual matrix, the terminals were removed and all inter-connections were made with printed circuit transmission line lengths.

3.3.3.2.2 Fixed-Phase Shifters

Fixed phase shift values of 30, 60, and 90 degrees are required to implement the twelve-port matrix. The fixed-phase shifts are relative to a fixed length of strip transmission line. Two types of differential fixed-phase shifters are utilized: coplanar and biplanar. The distinction between these two types of phase shifters was described earlier in

Section 3.2.3.2.2. The 60 and 90 degree phase shifters are biplanar and the 30 degree phase shifter is coplanar. The 90 degree phase shifter design was discussed in the above referenced section and hence will not be described in the following paragraphs. The 60 and 30 degree phase shifters have not heretofore been described and will be discussed below.

The construction of the 30 and 60 degree phase shifters is generally the same as the construction of the earlier described phase shifters. The distinction is the difference in the coupling values required to achieve the 30 and 60 degree fixed-phase shifts. The performance of these two 50-ohm phase shifters is listed in the following table:

$+30^{\circ}$ Fixed Phase Shifter (Coplanar Type)[1]

Frequency	1.7 kmc	2.27 kmc	1.7 — 2.3 kmc
Measured phase shift	$+30.2^{\circ}$	$+29.8^{\circ}$	
Greatest phase deviation	—	—	$+29.8^{\circ} - 33.0^{\circ}$
Maximum VSWR	1.13	1.21	1.23

$+60^{\circ}$ Fixed Phase Shifter (Biplanar Type)

Frequency	1.7 kmc	2.27 kmc	1.7 — 2.3 kmc
Measured phase shift	$+61.3^{\circ}$	$+58.8^{\circ}$	
Greatest phase deviation	—	—	$58.8^{\circ} - 62.5^{\circ}$
Maximum VSWR	1.13	1.10	1.15

Note 1) - Phase is that of coupled section relative to that of a straight line section.

All of the above data were obtained with TNC type input and output connections.

3.3.3.2.3 Performance of the Twelve-Port Matrix

The twelve-port matrix is formed in three layers of 1/16-inch polyolefin. All of the printing is contained in photo-registry on the center 1/16-inch thick layer. The components described above are integrated on this central layer in such a manner that no component-to-component coaxial connections are required. The entire package is contained within an 18-inch cylinder having a total depth of 5/16-inch. This total depth includes a top and bottom 1/16-inch thick aluminum support sheet. The performance of the twelve-port matrix is summarized below.

Frequency	1.7 kmc	2.27 kmc
Greatest measured amplitude imbalance	± 1.2 db	± 1.15 db
Average amplitude imbalance	± 0.8 db	± 0.7 db
Greatest measured phase deviation	$\pm 9°$	$\pm 12°$
Average phase deviation	$\pm 3°$	$\pm 4°$
Poorest measured isolation	14.5 db	13.8 db
Average isolation	23.4 db	23.9 db
Worst measured VSWR	1.55	1.37
Average VSWR	1.23	1.23
Average insertion loss	0.8 db	1.2 db

3.3.3.3 Twelve-Port Switching Network

The solid-state, single-pole 12-throw switch (SP12T) is required to reduce the twelve beam outputs of the beam-forming matrix to a single

terminal. The block diagram of this switch is defined in the sketch of Figure 27. It consists of eleven double-pole, double-throw solid-state transfer switches arranged to form a switching tree. The terminology and functioning of these transfer switches is identical to that which was described for the SP4T switch of Figure 21. The SP12T switch also has the feature that all unused ports are terminated.

The SPDT transfer switch used in the twelve-port matrix is the same high power switch which was described for the sixteen-port matrix. The twelve-port switch is formed in three layers of 1/16-inch thick poly-olefin with the central layer containing the r-f circuitry. Two 18-inch diameter, 5/16-inch thick three-layer strip transmission line packages were required to integrate the complete network. The output port positions were made to exactly coincide with the input ports of the twelve-port matrix. The input and output connections on the switching network were of the TNC variety. Connections between the beam matrix and the twelve-port switching network were made with commercial TNC type feed throughs. The average measured performance of this SP12T switch is defined below.

Frequency	1.7 kmc	2.27 kmc
Maximum VSWR	1.20	1.40
Average VSWR	1.17	1.35
Minimum Isolation	15.0 db	23.4 db
Average Isolation	21.0 db	25.1 db

BEAM PORT NUMBERS

8 7 6 5 12 11 10 9 4 3 2 1

SPDT TRANSFER
SWITCH

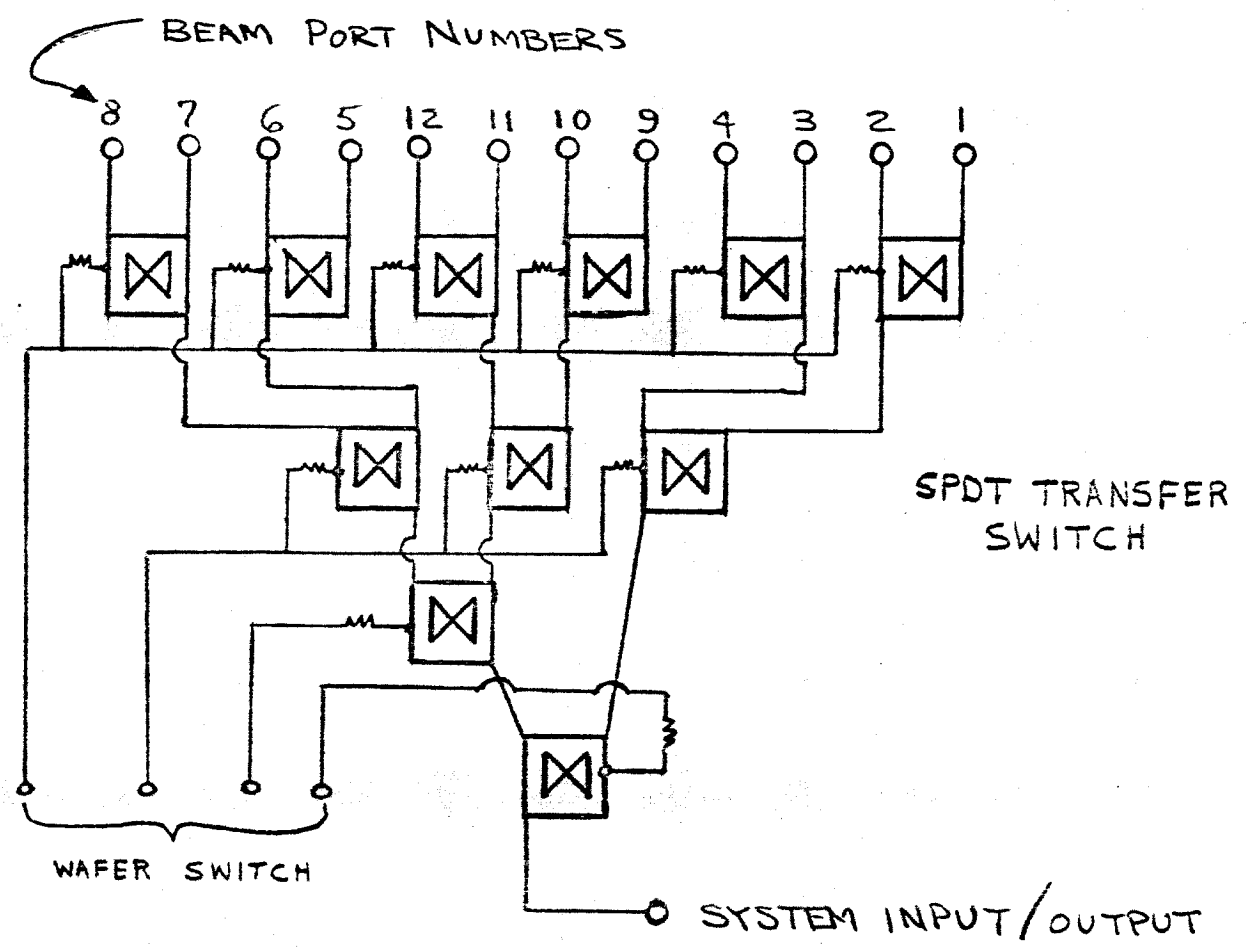SYSTEM INPUT/OUTPUT

WAFER SWITCH

Figure 27.   Schematic of SP12T switch.

| Maximum Insertion Loss | 2.8 db | 2.5 db |
| Average Insertion Loss | 2.4 db | 2.2 db |

3.4 Switch Control Network

The switch control network is a separate remote console which allows the beams of the cylindrical and planar arrays to be positioned at nanosecond rates. This section will describe the manner in which the individual switches are positioned by the remote network.

3.4.1 Elevation Bank-Cylindrical Array

The elevation switch control network for the cylindrical array consists of sixteen vertical banks of SP4T switches. The manner in which these switch banks are connected to the +6.3 VDC forward bias and the -30 VDC reverse bias is illustrated in Figure 28. All of the output SPDT switches are connected to a common lead. All of the input SPDT switches are connected to a separate control lead. In the example shown in Figure 28, both the input and output SPDT switches are biased in a forward direction by the +6.3 VDC terminal voltage. When biased in the forward direction, the output of each switch is the straight through path. Hence, the pictured arrangement will excite multiple-beam port III for each of the sixteen vertical banks. The two-terminal four-position wafer switch is located in the main console immediately behind the elevation bank selector for the cylindrical array.

3.4.2 Azimuth Switch Bank-Cylindrical Array

A schematic of the azimuth switch section of the circular array is
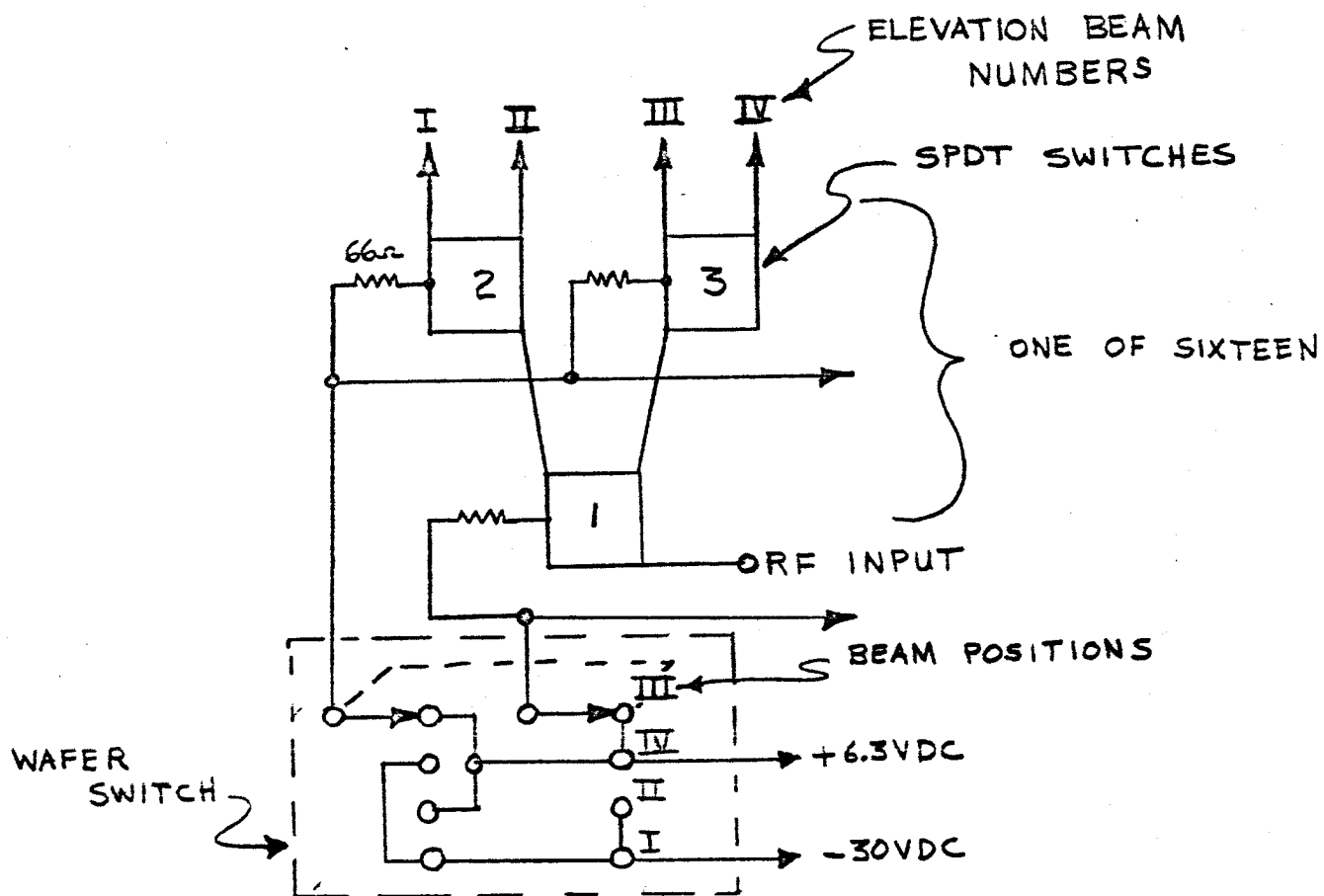
Figure 28. Control network for SP4T.

shown in the sketch of Figure 29. A four-terminal 16-position wafer switch, controlled from the front panel, is used to select a given beam position. One terminal position is required for each of the four switch banks. These individual switch banks are either connected to a +6.3 VDC forward bias or to a -30 VDC bias. This arrangement allows full and complete control of the beam positions. Thirty-three ohm resistors are utilized to maintain the proper bias of each of the individual switches. Switches 8 through 15 are photoetched on the printed circuit board which is closest to the beam-forming matrix. The switches denoted 1 through 7 are photoetched on the printed circuit switch network which is closest to the output of the array.

3.4.3 Switch Control for the Planar Array

The switch control schematic for the planar array is shown in the sketch of Figure 30. This switch control functions in much the same manner as the 16-pole switch required for the azimuth section of the cylindrical array. Four terminals with twelve positions each are required to connect the individual switch banks to either +6.3 VDC or -30 VDC. Switches numbered 6 through 11, are contained in the printed circuit package which connects directly to the twelve-port beam-forming matrix. Switches 1 through 5 are contained on a separate printed circuit board located immediately below the first switching network.

3.4.4 Power Supply

The power supply schematic is described by the sketch of Figure 31. Examination of this sketch will indicate that the forward bias and reverse bias
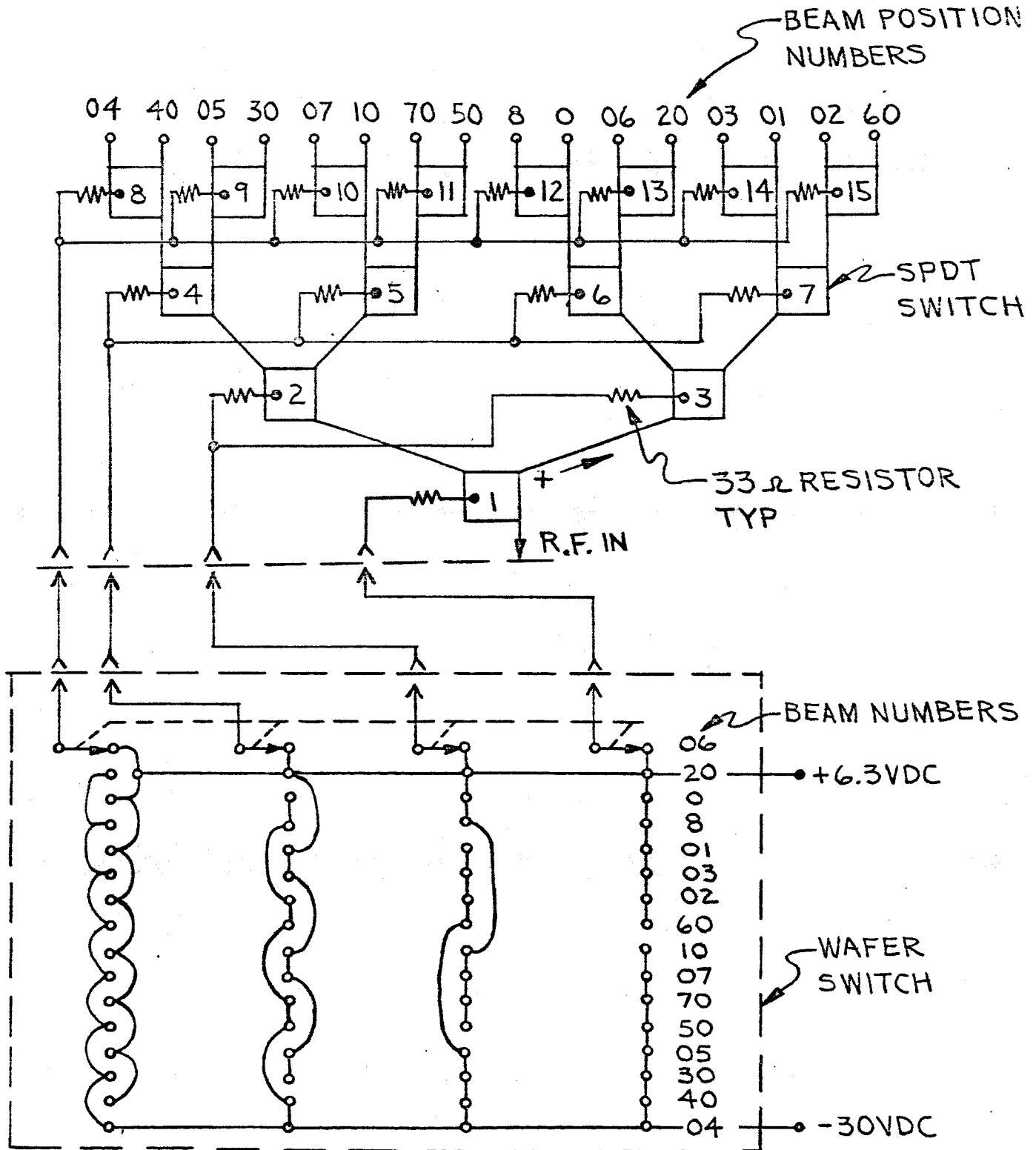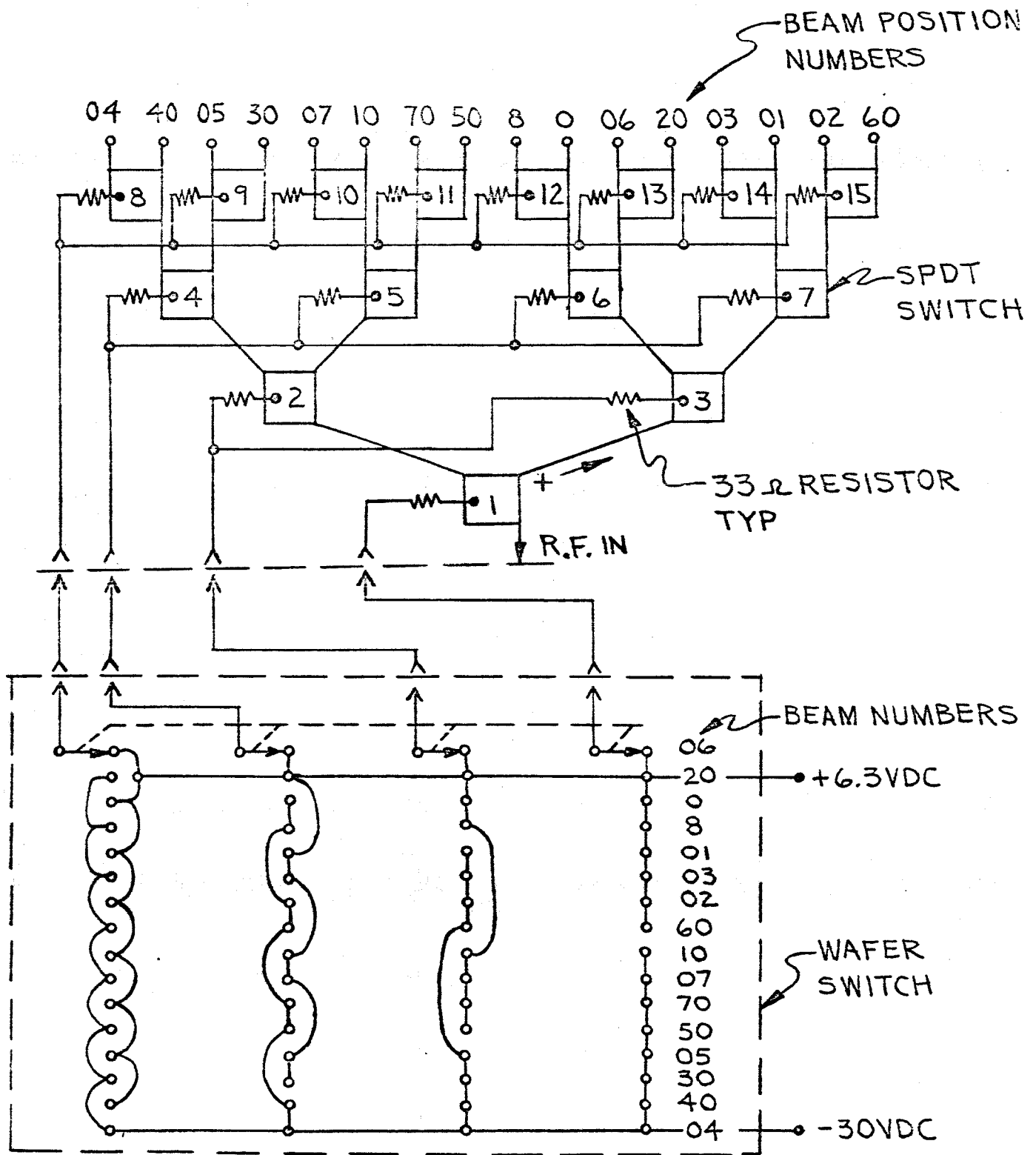
Figure 29. Control network for SP16T switch.

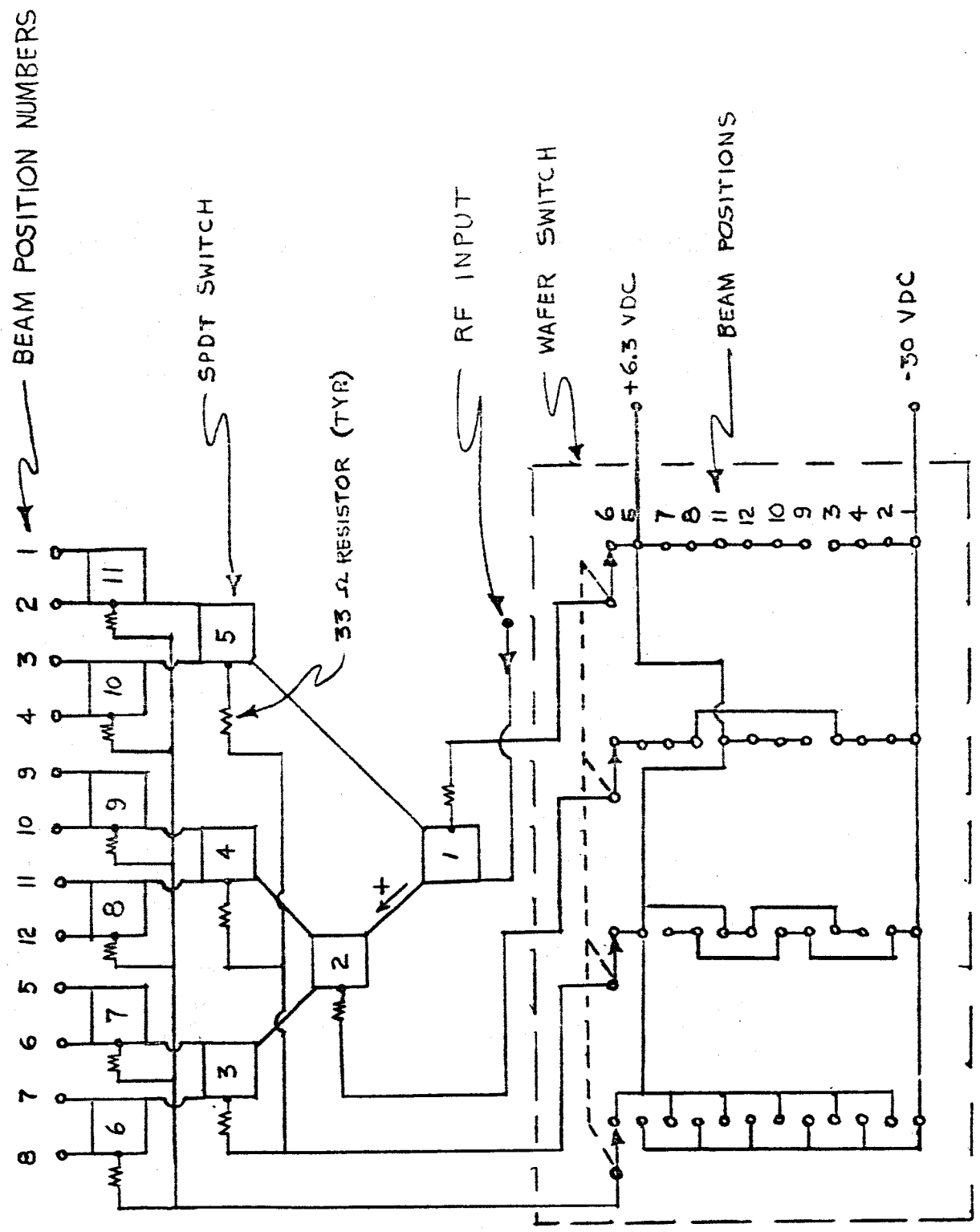Figure 29.   Control network for SP16T switch.

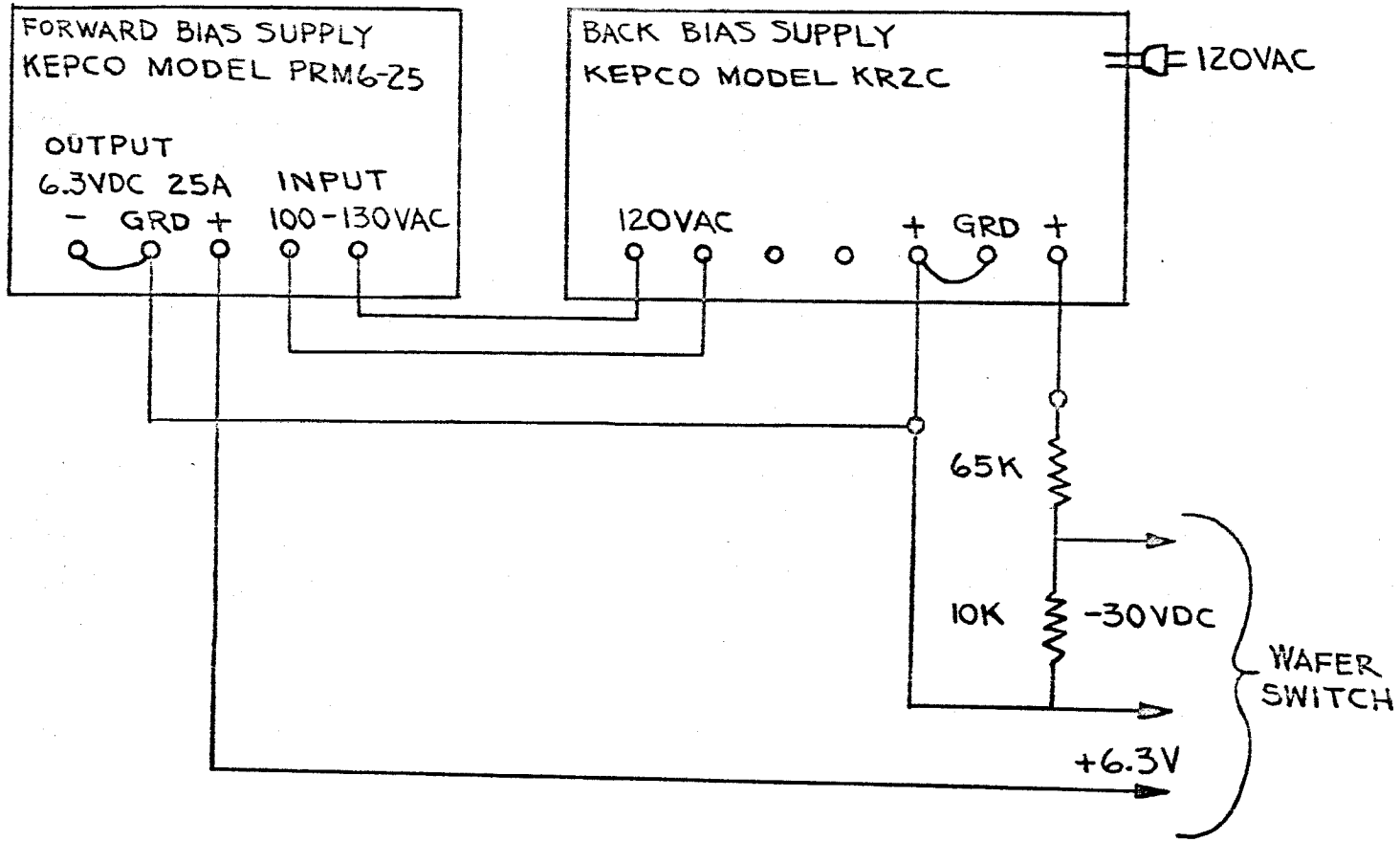Figure 30. Control network for SP12T switch.

Figure 31.   Power supply detail.

power supplies are commercial items purchased from the Kepco Company of Flushing, New York. The back bias power supply, in addition to supplying the 30 volt negative terminal voltage for back biasing the switches, also supplies the 120 volt input to the forward bias supply. These two units are contained in a console along with the required wafer switches and panel indicators. A control cable is used to interconnect the console to the antenna system.

3.5 System Packaging

The actual outward physical appearance of the developed antenna array was illustrated, in part, by the photograph of Figure 1. A more detailed indication of the antenna system packaging is illustrated in Figure 32. This figure shows the location of all of the major components of the antenna system. It further serves to define the manner in which the various system parts are interconnected. The major package dimensions are shown in the figure, along with a description of each of the major components. Not shown in the figure are the DC voltage connections and the necessary biasing resistors to control the switch networks. The DC bias leads and biasing resistors are located on printed circuit cards which are positioned directly below the 12-way switch.

Examination of the package will indicate that the interior volume of the cylindrical array is essentially open. While at the present time the mode network-to-elevation bank r-f cables are, for convenience, routed up through the center of this volume, in an operational installation, they could

be routed along the top of the mode-forming networks and up the sides of the SP4T switches to leave the central volume almost totally open.

The vertical banks, along with the matrices and the SP4T switches, are compactly packaged and hence not much could be done to decrease the volume occupied by these components. However, a considerable saving in space could be realized by compacting the package consisting of the mode-forming matrix, the beam-forming matrix, and the SP16T switch. It is estimated that this series of networks could be contained in a volume having an 18-inch diameter and a total depth of less than 1.5 inches. Furthermore, it would be possible to provide a larger access hole through the center of these networks to allow more flexibility in the use of the volume bounded by the cylindrical array. The same general comments apply to the twelve-port matrix and SP12T switch. The double-male TNC adaptors between the twelve-port multiple-beam matrix and the twelve-port switching network could be deleted, saving the equivalent amount of space.

An alternate possible arrangement for the cylindrical array would be to wrap the beam-forming, mode-forming and switch control networks around the interior of the cylinder immediately behind the SP4T switches, thus making available complete access from the base of the array.

The weight of the antenna system measures 83 pounds, including all support members and the antenna housing.

3.6 The Interpositioned Four-Beam Vertical Array

It was noted in Section 3.2.3.3 that the interpositioning diodes of the vertical sections of the cylindrical array were not included in the developed antenna system. However, it was felt that the technique was of sufficient merit that it justified experimental verification. Accordingly, an array consisting of four spiral elements and a four-port multiple-beam matrix, with interpositioning, was fabricated. The spiral elements are identical to those described for the cylindrical array. The four-port multiple-beam matrix is also identical to that described for the cylindrical array. However, in this instance, the interpositioning diodes are added. The schematic of the four-port matrix, included earlier as Figure 19, is thus the schematic for the multiple-beam array with interpositioning. The distinction, of course, is that the two-step phase shifters are included in the four-port matrix.

The interpositioning phase shifters are implemented by using diodes and couplers much in the same manner that they are used in the SPDT switch. A schematic of the two-step solid-state phase shifter is shown in Figure 33. The network consists of a 3 db coupler with an input and an output terminal. The output terminal is the normally isolated terminal of the 3 db coupler. The two normal outputs of the 3 db coupler are connected, with equal lengths of line ($\emptyset_1$), to two like 1N270 diodes. The outputs of these diode terminals are, in turn, connected to two equal lengths of line ($\emptyset_2$). With the diodes in reverse bias, the length of line is equal to $\emptyset_1$. When the diodes are in forward bias,
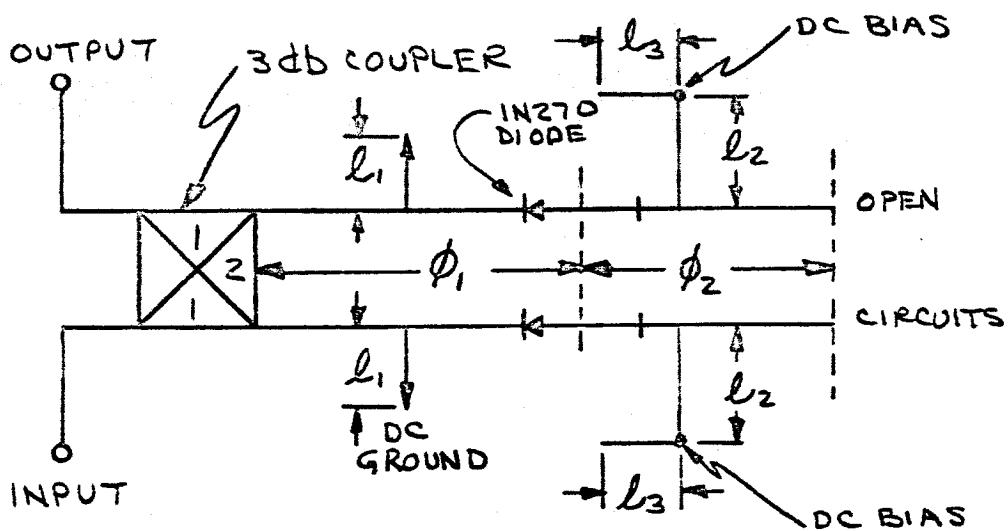
Figure 33.   Two-step solid-state phase shifter.

the total length of line is $(\emptyset_1 + \emptyset_2)$. Since both the forward and reflected paths must be included in estimating the phase shift, the total path length difference, from a reverse bias to a forward bias case, is equal to $2\emptyset_2$. The desired phase shifts from element to element are obtained by simply varying the length $\emptyset_2$ from element to element. The values of $2\emptyset_2$ are set equal to $0°$, $+45°$, $+90°$, and $+135°$ at a center frequency of 2000 mc. These are the required values for proper interpositioning of the beam. They correspond to the values initially defined in Figure 19.

The two-step phase shifter consists of a 3 db coupler and two 1N270 diodes. The values of $\emptyset_1$ for all phase shifters are equal, thus establishing the in-phase case. The coupler is identical to that described for the four-port matrix. The diode biasing and drive circuits are identical to those described in Section 3.2.3.5 and Figure 20. A 50 ma drive is required at a forward bias of +6.3 VDC. The reverse voltage used is -30 VDC. The measured characteristics of the four-port matrix with the solid-state phase shifters are listed below.

Frequency	1700 mc	Bias	2270 mc
Maximum VSWR	1.25	Forward	1.40
	1.45	Reverse	1.39
Average VSWR	1.17	Forward	1.21
	1.17	Reverse	1.24
Minimum Isolation	22.3 db	Forward	21.3 db
	24.7 db	Reverse	20.1 db
Average Isolation	27.3 db	Forward	29.8 db
	26.5 db	Reverse	25.6 db
Average Loss	2.2 db	Forward	2.2 db
	0.6 db	Reverse	0.7 db

Comparison of the loss of this four-port network with that described earlier on page 64, indicates that the forward bias loss of the two-step phase shifter is approximately 1.9 db at 1700 mc and 1.6 db at 2270 mc.

4.0   SYSTEM PERFORMANCE

The entire body of Section 3.0 was devoted to a description of the system theory of operation and the design detail of the components which were required to implement the system.   This section will describe the far-field pattern data obtained with the developed antenna system.   Consideration will be given to a comparison of the measured data with the predicted data.   The coordinate system which will be used throughout this section is that which was initially described in Figure 2 of the report.   The following discussion will be divided into three general sub-sections: a description of the data obtained from the cylindrical array portion of the system;   a description of the data obtained with the twelve-element array;   and a description of the data obtained with the interpositioned array.

4.1   Performance of the Sixteen-element Multiple-beam Circular Array

Figures 34 through 37 contain composite patterns, in the azimuth plane, for the multiple-beam cylindrical array.   Figures 34 and 35 represent the data taken at 1700 mc for elevation angles of -6 degrees and +16 degrees, respectively.   Figures 36 and 37 represent the data taken at 2270 mc for elevations of -6 degrees and +16 degrees, respectively.

The average beamwidths at 1700 mc are equal to 22.5 and 23 degrees, respectively, for both the -6 and +16 degree elevation stations.   The range in beamwidths for both instances varied from as low as 21 degrees to as high as 25 degrees.   The theoretical beamwidth was predicted as being equal to 20 degrees.
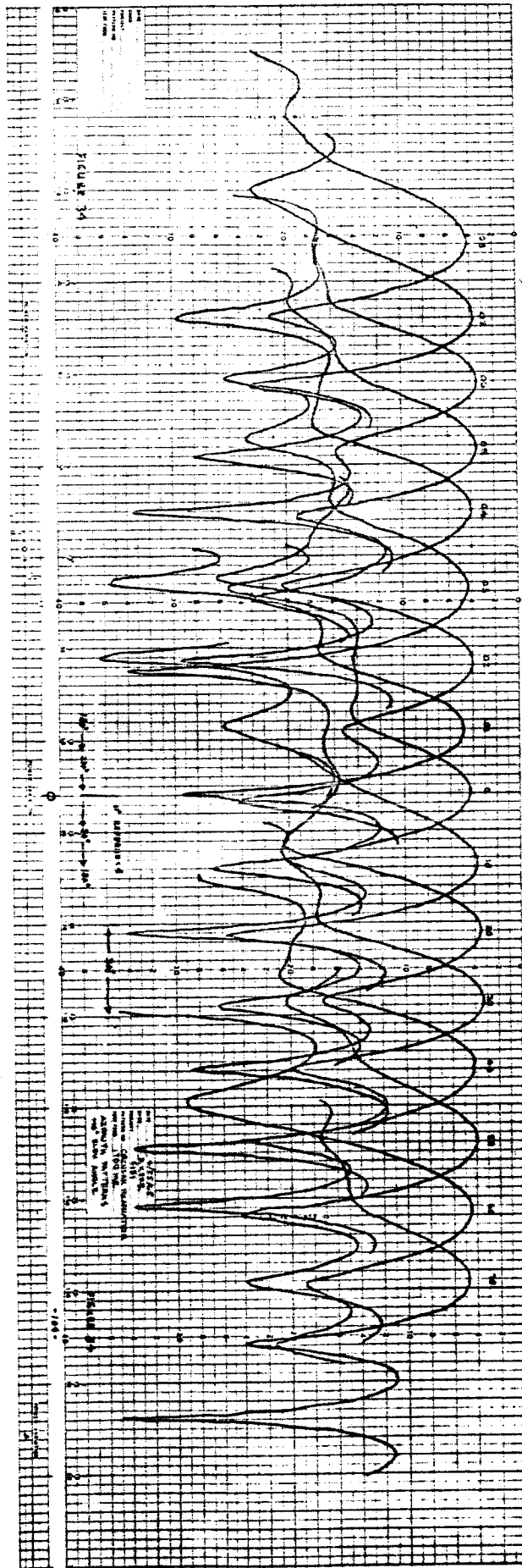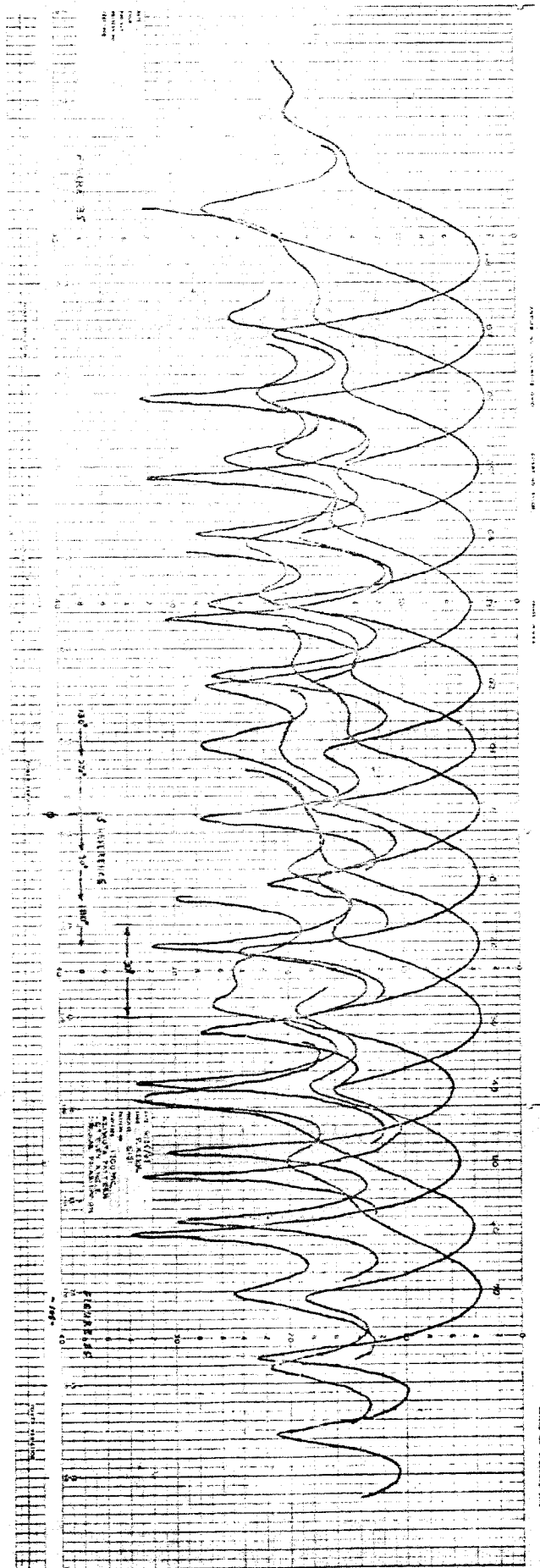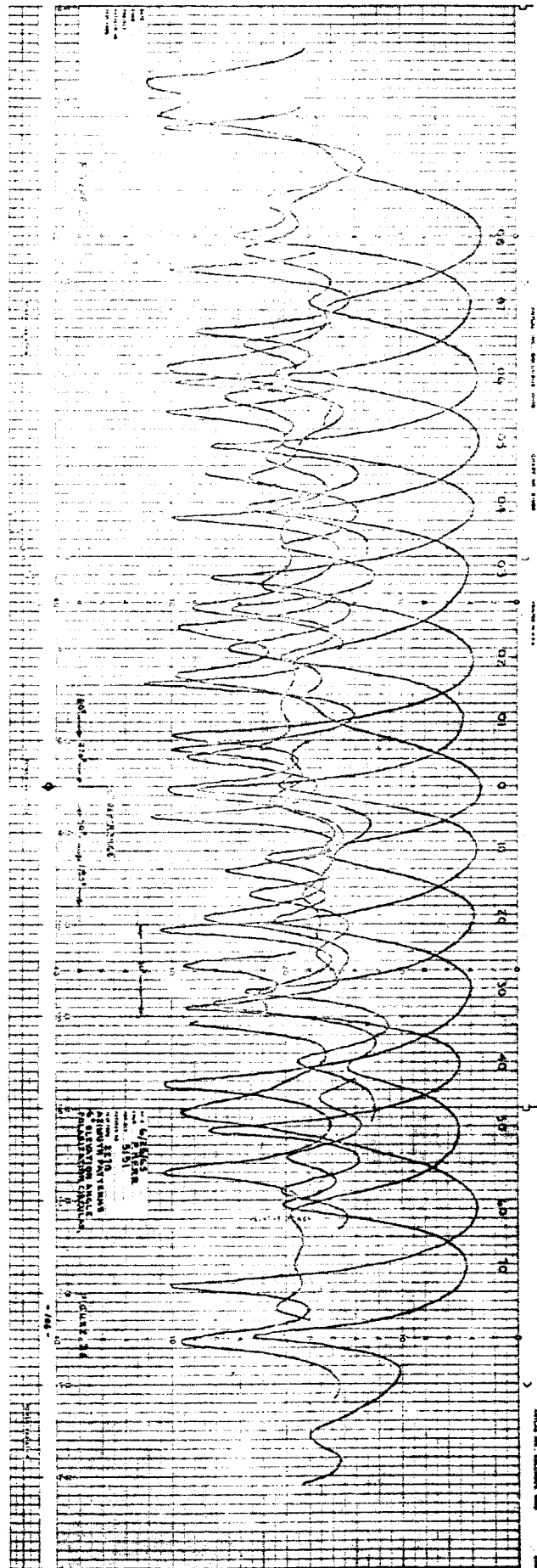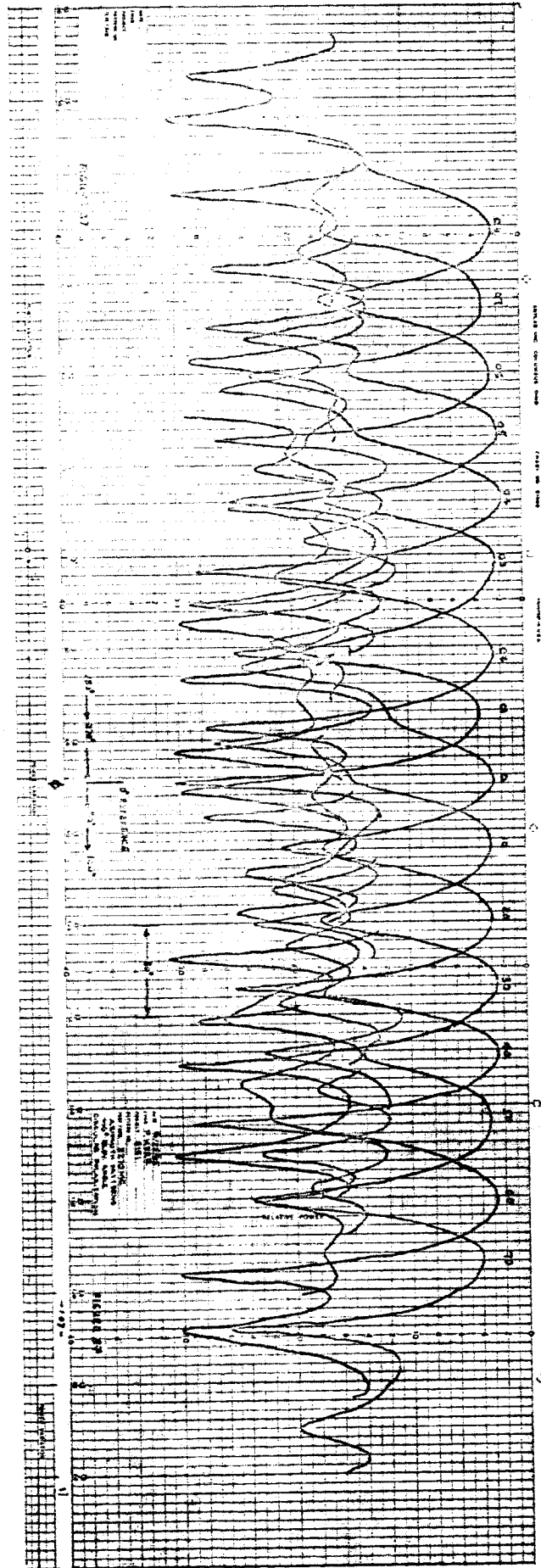
The average crossover levels are -3.4 db and -3.2 db, respectively, for the -6 and +16 degree elevation stations. The range of crossover levels at -6 degrees extends from -2.6 db to -4.2 db. At the +16 degree elevation station, the crossover levels vary from -2.6 db to -3.6 db. The theoretical value is approximately -3.9 db. The average maximum sidelobe level at the -6 degree elevation station is -8.6 db. The range of the maximum sidelobe levels extends from -6.2 to -11.2 db. The predicted sidelobe level was an average of -11.2 db for the computed vertically and horizontally polarized patterns. The average maximum sidelobe level at an elevation station of +16 degrees is equal to -8.5 db with a range extending from -7.2 db to -13.6 db. The measured gain variation is ±1.5 db at an elevation station of -6 degrees, and ±0.8 db at an elevation station of +16 degrees.

The depicted pattern data for 2270 mc indicates that the average beamwidth is equal to 23 degrees at both elevation stations. The beamwidth range varies from 20 to 25 degrees at an elevation station of -6 degrees and from 21 to 25 degrees at an elevation station of +16 degrees. The average crossover levels vary from -3.0 db at -6 degrees to -3.2 db at +16 degrees. The range of crossover level variations extends from -1.8 to -4 db at -6 degrees and from -2.7 to -4.2 db at +16 degrees. The average maximum sidelobe level at the -6 degree elevation station is -9.8 db with a maximum-to-minimum range extending from -5.7 db to -13.1 db. The corresponding maximum sidelobe levels at the elevation station of +16 range from -7.2 db to -13.6 db with an average maximum of -10.4 db. The gain

variation from beam to beam is ± 1 db for both elevation stations. The predicted beamwidth at 2270 mc is 20 degrees and the predicted sidelobe level is -9.1 db. The theoretical crossover value is -3.9 db.

Data were also taken at the noted elevation stations for horizontal and vertical polarizations. However, the circularly polarized data is representative of the average values obtained for these two individual polarizations. Hence, these linearly polarized data are not included in the report. Some data were also obtained at elevation stations of -28 degrees and +40 degrees. These data were very similar to those shown for an elevation station of +16 degrees and hence are not included in the report.

The measured data indicate that the beamwidths for the circular array are indeed constant. However, the average beamwidths in both cases, while they are near constant at 23 degrees, do not agree with the theoretical value of 20 degrees. This disparity in beamwidths is largely attributed to the normalizing of the upper and lower frequency range performance. Initially the theoretical phase compensating cable lengths were used in the system. However, it was found that the best data were obtained by adjusting these cables for equal performance at the high and low end of the frequency ranges. This adjustment generally tended to broaden the beamwidth in an amount equal to the deviation between theory and practice. The crossover levels were a measured average of approximately -3.1 db instead of the predicted value of -3.9 db. However, this difference in crossover levels is reasonable in view of the increased beamwidth
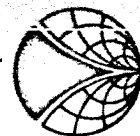
which was measured. The average sidelobe level obtained at 2270 mc closely corresponds with the sidelobe level predicted. The predicted average sidelobe level is -9.1 db and the measured average sidelobe level is 10.1 db. The variation in beamwidths crossover levels and beam gains at a given frequency and elevation station, are largely attributable to errors within the matrix and to normal design model variations in the individual component parts.

While the array was specifically designed for two frequencies, in actual fact its performance is relatively constant over the range from 1700 to 2270 mc. Spot checks at intermediate frequencies and for various beam positions indicated that the array would function in approximately the same manner over the full bandwidth.

The axial ratio of the cylindrical array was spot checked at a number of beam positions at both the low and high frequencies. The average axial ratio measured at 1700 mc was 2 db and the average axial ratio measured at 2270 mc was 1.4 db.

Elevation patterns were also measured with the cylindrical array. However, it was difficult to take complete elevation plane pattern cuts because of the limited range of the azimuth - elevation pedestal being used. A typical measured 2270 mc pattern, for the "0" degree reference beam position, (see Figures 36 and 37) is shown in Figure 38. These pattern data are similar to those obtained for the single elevation bank with the exception that the sidelobe level for the +40 degree station is somewhat better.
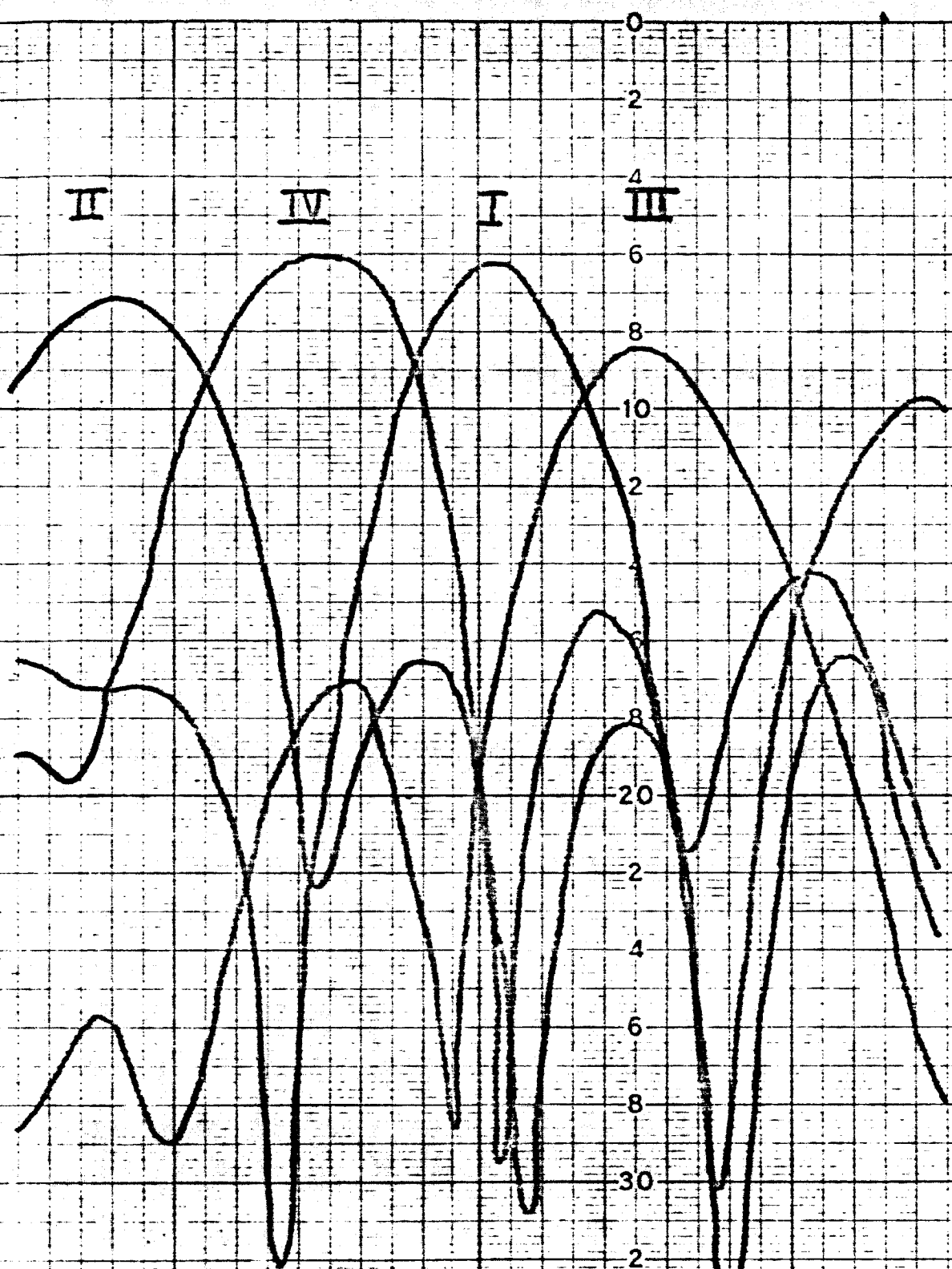
FREQ : 2270 mc
POLAR: Circular
INPUT: "O" Beam Position

FIGURE 38 Elevation Patterns of 4×16 Cylindrical Array.

The average measured gain of all of the beams at an elevation station

of -6 degrees and at a frequency of 2270 mc is equal to +12.8 db absolute. The

individual beam gains vary by approximately ± 1 db about this average value. The

computed gain derived from the simple relationship

$$G \approx 10 \text{ Log } (32,500/(BW_1) (BW_2)), \tag{17}$$

where: BW_1 = elevation BW = 18°,

BW_2 = azimuth BW = 23°,

is equal to approximately 18.9 db. Thus the difference between the estimated

theoretical gain and the measured gain is approximately 6.1 db. This is a quite

reasonable differential as the following table will indicate:

Measured Gain	12.8 db $\pm$ 1 db
Losses (2270 mc)	
4-port matrix:	0.6 db
SP4T switch:	1.5 db
16-port mode network:	1.0 db
16-port beam network:	1.0 db
Cable:	0.8 db
Spiral element (estimated):	0.5 db
Total losses:	5.4 db
Gain + Losses:	18.2 db

The estimated loss of the spiral antenna, although it could not be measured, is

believed to be reasonable. The unaccounted difference between the measured

and estimated figures is 0.7 db. This differential is believed to be attributable to energy lost in sidelobes. Thus, the gain measured with the system is reasonably consistent with the computed values. The measured gain at 1700 mc is equal to 14.2 db while the computed gain is estimated at 18.1 db. The 3.9 db difference is traceable to network losses. The remaining difference of 1 db is attributable to energy lost in the sidelobe regions. The above measured gain data do not include the losses in the SP16T network.

4.2 <u>Measured Performance of the Twelve-Element Planar Array</u>

Pattern data for the twelve-element planar array are contained in Figures 39 through 46. The data are for frequencies of 1700 and 2270 mc. The polarization is E_ϕ and the beam notation is as described earlier in Section 3.3. The coordinate system utilized is that described in Figure 2 of this report. The patterns are presented in a somewhat unusual manner because of the beam distribution in space. All patterns are θ plane cuts. However, the ϕ plane has been selected to pass through the beam maximum for each beam. The ϕ plane selected is defined at the top of each of the patterns contained in the figures. The most salient characteristics of the far-field patterns are summarized below in tabular form.

Beam No.	BW (degrees) 1700 mc/2270 mc	1st Side Lobe (db) 1700 mc/2270 mc	Grating Lobe (db) 1700 mc/2270 mc
1	26/21	-13.8/-12.0	-14.6/-14.2
2	36/23	-12.6/-15.4	-14.2/-13.8
3	35/22	-14.6/-18.4	-10.0/-11.4
4	29/21	-10.8/- 9.6	-10.0/- 4.6

Beam No.	BW (degrees) 1700 mc/2270 mc	1st Side Lobe (db) 1700 mc/2270 mc	Grating Lobe (db) 1700 mc/2270 mc
5	27/20	-13.0/-18.0	——/-11.5
6	35/23	-10.2/- 8.4	——/-16.2
7	35/23	-13.8/-14.6	-10.1/- 9.9
8	30/21	-11.0/-13.2	-10.5/- 6.2
9	27/20	-14.6/-13.4	-15.8/-11.2
10	34/24	-11.0/-12.3	-15.5/-16.8
11	35/23	-13.8/-17.0	-11.5/-17.2
12	31/21	-11.1/-10.4	- 9.2/- 4.6

Examination of the above data will indicate that the beamwidths generally increase as the position relative to the boresight axis increases, while the sidelobe levels generally become higher as the angle from boresight increases. The measured sidelobe levels range from -18 db to -12 db. These levels may be compared to a theoretical value of approximately -15.6 db. The grating lobes are a by-product of the element spacing and are generally worse at the highest frequency as would be expected. The pattern data were also taken for E_θ polarizations. However, the similarity of the data coupled with the large number of patterns required to describe this data in the report, did not warrant their inclusion.

The measured gain at 1700 mc was 14.6 db. The measured gain at 2270 mc was 17 db. These figures may be compared to approximate computed values of 16.5 and 19.1 db. The differences are attributable to losses in the twelve-port network and the spiral antennas. The above gain figures do not include the loss in the 12-way switching network which was added after these data were taken. The losses in the twelve-port switching network were defined in Section 3.3.

4.3 Multiple-Beam System With Interpositioning

Pattern data for the interpositioned four-element array are shown in Figures 47 and 48. These data are for $E_{\emptyset}$ polarizations (horizontal polarization) and contain the patterns for both the interpositioned and non-interpositioned states. The pattern data are in good accord with theory. By way of example, the reader may refer to the predicted patterns of Figure 49 which are for a frequency of 2270 mc. The pattern data for E_{θ} (vertical polarizations) are essentially the same as those shown for $E_{\emptyset}$ polarizations. Examination of the experimental patterns will indicate that the interpositioned beams raise the level at crossover by an amount ranging from 1.5 to greater than 2 db. However, since the addition of the two-step phase shifter decreased the non-interpositioned gain by approximately 0.3 db, the net gain increase ranges from 1.2 to 1.7 db. The question of whether or not this improvement in the gain at the crossover position warrants the inclusion of two-step phase shifters must then depend on whether the added gain warrants the increased complexity. It is worth noting that the gain loss in the reverse bias case, caused by the diodes in the two-step phase shifters, could be improved by almost 1 db if more time is spent in developing the component.

The depicted data indicates that the interpositioning technique is feasible and that the technique could be included as part of the cylindrical array concept (or indeed as part of any multiple-beam array concept).

5.0   RECOMMENDATIONS AND CONCLUSIONS

The preceding report has discussed the implementation of two rather unique concepts and their integration into a package format which could be considered reasonably typical for an orbiting satellite.   The antenna data obtained are in generally good accord with computed data.   The interpositioning technique has been shown to improve the gain at the crossover regions by approximately 1.2 to 1.7 db.   The high-power, solid-state SPDT switch developed and implemented in the SP12T and SP16T switches has demonstrated its capability of handling in excess of 20 watts of average power.

It appears that the pattern performance of the planar array technique, the cylindrical technique, and the interpositioning technique can be reasonably well predicted by theory.   It has further been demonstrated that these antenna techniques are at least usable over the investigated bandwidth.   Furthermore, switching techniques have been developed which can handle in excess of 20 watts of average power; a power level reasonably consistent with most satellite applications.   The cylindrical array concept is particularly intriguing since it allows the interior volume of the satellite to be used for other purposes.

Many satellite antenna systems might require lower sidelobes than those achievable from the uniformly illuminated array.   Such a low sidelobe multiple-beam cylindrical or multiple-beam planar array system has not been developed at this time.   However, it is believed that, since the uniformly excited techniques generally result in data which are consistent with theory,
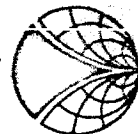
corresponding improvements would be achieved with non-uniform tapered distributions. It is recommended that the cylindrical array technique be given every consideration, particularly where the satellite attitude is random or where spin stabilization is utilized. In the instance of spin stabilized satellites, the need for high gain omnidirectional coverage is not necessary. However, even in this instance the cylindrical array would be most useful since it would allow automatic de-spinning of the far-field beam.

The effort supported by this reported program indicates that high gain, omnidirectional receiving and transmitting antenna systems are practical in a satellite-type configuration. It is felt that sufficiently good results have been obtained to allow the development of an operational system within a 12 to 24 month span; with the time dependent on system complexity.

BIBLIOGRAPHIES

1. G. G. Chadwick, J. C. Glass, "Investigation of a Multiple-Beam
    Scanning Circular Array," Scientific Report No. 1, prepared for
    AFCRL under Contract No. AF 19(628)367, AD-411868; 31 December
    1962.

2. Radiation Systems, Incorporated Technical Proposal TP-217(U),
    "Steerable Array Design," dated 21 September 1964.

3. Radiation Systems, Incorporated Technical Report No. 45,
    "Multi-Beam Mobile Antenna Array," prepared for Radio Corporation
    of America under Contract No. MOB-12-91 dated 24 February 1964.

4. T. T. Taylor, "A Synthesis Method for Circular and Cylindrical
    Antennas Composed of Discrete Elements," Trans. IRE Antennas
    and Propagation, No. 3, p. 251; August 1952.

5. Ta-Shing Chu, "On the Use of Uniform Circular Arrays to Obtain
    Omnidirectional Patterns," Trans. IRE, Vol. AP-7, pp. 436-438;
    October 1959.

6. J. Blass, "Multidirectional Beam Scanning Antenna Array," First
    Interim Report No. W. O. 4071-1, prepared for Rome Air. Dev.
    Center under Contract AF-30(603)1920; July 1958 - April 1959.

7. J. P. Shelton and K. S. Kelleher, "Multiple Beams from Linear Arrays,"
    Trans. IRE, Vol. AP-9, No. 2, pp. 154-161; March 1961.

8. William P. Delaney, "An RF Multiple Beam Forming Technique,"
    Massachusetts Institute of Technology, Lincoln Laboratory,
    Technical Report dated 9 August 1961.

9. J. Butler and R. Lowe, "Beam Forming Matrix Simplifies Design of
    Electronically Scanned Antennas," Electronic Design 9, 170;
    12 April 1961.

10. R. Bawer and J. J. Wolfe, "A Printed Circuit Balun for Use With
    Spiral Antennas," IRE Trans. on Microwave Theory and Techniques,
    Vol. MTT-8, No. 3, May, 1960.

11. B. M. Schiffman, "A New Class of Broad-band Microwave 90-Degree
    Phase Shifters," IRE Trans. on Microwave Theory and Techniques,
    Vol. MTT-6, No. 2, pp. 232-237, April 1958.